A STUDY OF HADRONISATION IN e^+e^- ANNIHILATION AT THE Z^0 USING K^0 MESONS

by

ALIX POULADDEJ, B.Sc., M.Sc., B.Sc., M.Sc.

A thesis submitted to

the Faculty of Graduate Studies and Research

in partial fulfilment of the requirements for the degree of

Doctor of Philosophy

Department of Physics

Carleton University, Ottawa-Carleton Institute for Physics

Ottawa, Ontario

6^{th} July 1992

The undersigned hereby recommend to

the Faculty of Graduate Studies and Research

acceptance of the thesis,

"A STUDY OF HADRONISATION IN e^+e^- ANNIHILATION AT THE Z^0 USING K^0 MESONS"

submitted by

ALIX POULADDEJ

in partial fulfillment of the requirements

for the degree of Doctor of Philosophy

P. G. Wood

Chair, Department of Physics

Richard J. Hemingway

Thesis Supervisor

D. G. Stairs

External Examiner

Carleton University

2 September 1992

Abstract

The process of hadronisation in e^+e^- annihilation falls in the non–perturbative regime of QCD (the theory of strong interactions) which, at the present time, is theoretically non–calculable. Consequently, one has to rely on phenomenological models to describe this process. The accuracy and validity of these models is then tested in terms of various aspects of particle production in multihadronic events, thereby furthering our understanding of the hadronisation process.

The study of K^0 production resulting from hadronisation in e^+e^- annihilation at the Z^0 peak forms the subject matter of this thesis. The analysis presented here is based on a data sample containing 138,638 Z^0 multihadronic events (corresponding to an integrated luminosity of 6.5 pb^{-1}) which was collected by the OPAL detector in 1990 at the LEP collider.

The inclusive production rate for K^0 is determined to be:
$1.95 \pm 0.03(stat.) \pm 0.14(sys.)$ per multihadronic event and is found to be consistent with particular Monte Carlo models. This rate corresponds to a strangeness suppression factor of $\gamma_s = 0.25 \pm 0.03$.

The detailed kinematical distributions used to investigate K^0 production were divided into two classes– those that were based purely on single particle properties and others that depended on the global shape parameters of the event. For the former case, the momentum and scaled energy distributions were studied. For the latter category, the distributions of the transverse momentum in and out of the event plane, the rapidity and the event sphericity were investigated.

The overall conclusion reached is that the production of K^0 within multi-hadronic events is well described and is consistent with the considered hadronisation models.

Acknowledgements

The field of high energy physics is a very challenging field which allows students to grow in many ways. I would like to thank Bob Carnegie as our group leader allowing me the opportunity to participate in the OPAL collaboration and benefit from exposure to CERN's environment.

I would also like to thank Richard Hemingway, my thesis supervisor, for his constant guidance and his cheerful and positive approach to physics. His help is gratefully acknowledged.

In a large group, on has the opportunity to collaborate with a number of people and benefit from their different backgrounds and experiences. On this note, I would like to thank Mike Ogg and Penny Estabrooks who I worked with and learned from at different times.

Alan Barney is thanked for doing such a wonderful job on the upkeep of the OPAL software; a man who always sorted out any computing, Latex or disk space problems one encountered. Our system manager Bill Jack is also thanked for his kind assistance at various times.

Finally, I Would like to thank my family and my fiancée Susan Jessica for their constant support and love throughout the entire length of this degree.

Contents

List of Tables

List of Figures

Chapter 1

Introduction

1.1 A Brief History of Particle Physics

The atomistic nature of the material world dates back to the days of the early Greek Philosophers. Just before the turn of this century the existence of atoms had been experimentally verified, and these atoms were believed to be the fundamental building blocks of matter. At that time, the only forces known to act on these material particles were gravity and electromagnetism.

The discovery of the negatively charged electron by J. J. Thompson in 1897 and the positively charged nucleus by E. Rutherford in 1912, both smaller in size than the atom, hinted at the subatomic nature of matter.

Experiments subsequent to Rutherford's discovery indicated that the nucleus was made up of densely packed positively charged objects (protons) and neutral objects (neutrons). Also, during the 1930s and the 1940s, cosmic–ray data provided clear evidence for the existence of many new particles, and conclusively ruled out the widely accepted view of the 1920s which regarded the electron and the proton as the elementary constituents of matter. This heralded the birth of modern elementary particle physics.

In order to account for the stability of the nucleus against the repulsive electromagnetic forces between the protons, a force field stronger than electromagnetism was postulated: it was simply named the "strong force". The first

important theory of the strong force was put forward by H. Yukawa in 1935 [1]. In doing so, he proposed a "quantum" of the field responsible for transmitting this strong force. This agent came to be known as the "meson". The existence of the π meson was eventually confirmed by Powell's group in 1947 [2] by nuclear emulsion techniques. Strongly interacting particles ("hadrons") were then categorised into two subclasses: mesons (carriers of the strong force, such as the π meson), and baryons (such as the proton).

The transmutation of matter, as observed in radioactivity, was explained in terms of the existence of yet another force, the "weak force". E. Fermi in 1934 [3] proposed the first weak interaction theory to explain $\beta-$decay in analogy with the electromagnetic current$-$current interaction.

By 1947, the muon, the π meson, and Dirac's positron (antiparticle of the electron) had been discovered and Pauli's neutrino had been postulated (though not detected). At this time, the K^0 meson was observed by Rochester and Butler in 1947 [4] with its characteristic two$-$prong decay in their cloud chamber.

The K^0 meson was heavier than the π meson and was referred to as a "strange" meson, for it was produced rapidly (time scale 10^{-23} s) but decayed slowly (time scale 10^{-10} s). A. Pais in 1952 [5] proposed the concept of *strong production* and *weak decays* for such strange particles. Pais's idea was implemented by M. Gell-Mann [6] and K. Nishijima in 1953 [7] in terms of a new property of matter called "strangeness", which is conserved in any strong interaction, but is not conserved in weak interactions.

1.2 The "Periodic Table" of Elementary Particles and the Quark Model

By 1960, a large number of strongly interacting particles had been discovered. Apart from the classification of these mesons and baryons according to their mass, charge and strangeness, no real underlying pattern was apparent. This was all changed in 1964 when Gell-Mann and Ne'eman [8] proposed the Eightfold Way, in which they arranged baryons and mesons in certain geometrical patterns according to their charge and strangeness. One could alternatively plot these geometrical patterns in terms of "hypercharge" (Y) and third component of isospin (I_3). Hypercharge is an additive quantum number which is defined in terms of strangeness and baryon number (B), via:

$$Y = B + S \tag{1.1}$$

The charge, Q, is then given in terms of the third component of isotopic spin and hypercharge via:

$$Q = I_3 + \frac{Y}{2} \tag{1.2}$$

Figure 1.1 shows one such pattern for the eight lightest mesons, forming the pseudoscalar meson octet. An explanation for the Eightfold Way was offered by Gell-Mann and Zweig in 1964 [9] who independently postulated an even more elementary constituent of matter from which hadrons were built; Gell-Mann called these *quarks*. Initially three quark types (or "flavours") were introduced, known as up (u), down (d), and strange (s).

In 1970 Glashow, Illiopoulos and Maiani [10] proposed a fourth quark, known as charm (c), to account for the observation of highly suppressed strangeness–changing

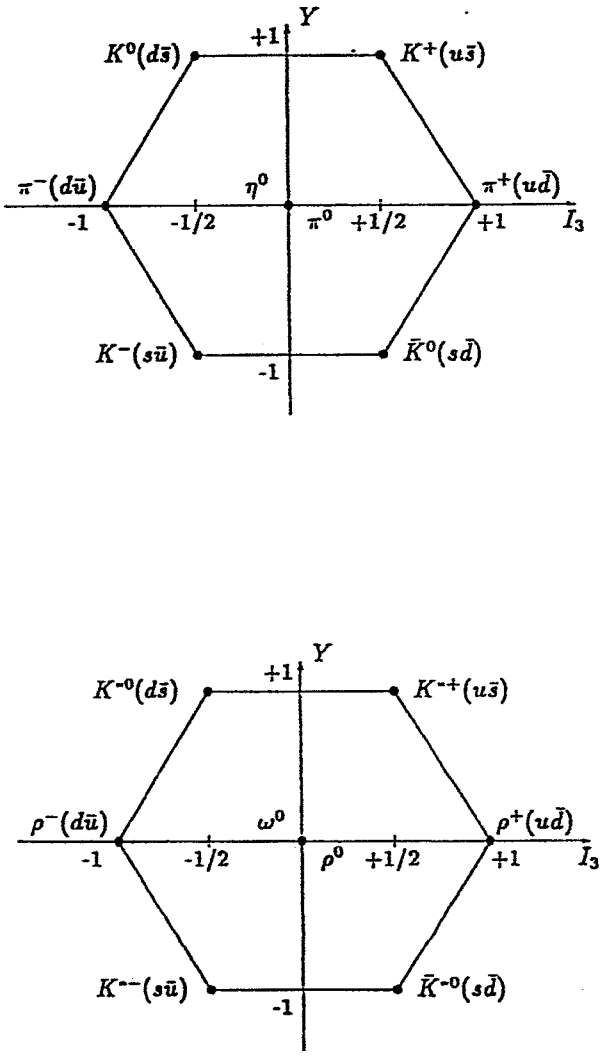

Figure 1.1: Geometrical configuration for (a) the pseudoscalar mesons and (b) the vector mesons as arranged in the Eightfold Way.

neutral currents (the GIM mechanism). The existence of this charm quark was experimentally verified by the independent discovery of the J/ψ particle at SLAC and BNL in 1974 [11].

Prior to the discovery of the charm quark, Kobayashi and Maskawa in 1972 had in fact proposed 3 generations of quarks in order to account for the observed CP violation in nature [12]. The two quarks making up the third generations are know as bottom or beauty (b) and top or truth (t).[1]

For a review of these aspects of particle physics, the reader is referred to the bibliography item [13].

1.3 Strong and Electroweak Theories

The present theory of the strong interaction is known as Quantum Chromodynamics (QCD) [14] in which each quark carries a colour charge that can have three values: Red, Green, or Blue. The interaction between the quarks is mediated by the quantum of the field known as the gluon (g). Quarks and gluons are known collectively as partons.

Mesons are made up of quark–antiquark pairs ($q\bar{q}$), while baryons consist of three quarks (qqq). The observed hadrons (mesons and baryons) are colourless.

The non–abelian nature of QCD [2] results in a self–interaction of the gluons. This has the consequence that at short distances the colour interaction between the quarks "switches off". This is known as "asymptotic freedom". The opposite to asymptotic freedom is "confinement" where, as quarks move apart, the colour force between them increases and the gluon field between them is squeezed into

[1]The top quark still remains to be experimentally discovered. The bottom quark was discovered at FNAL in 1977.

[2]Non–abelian means that successive gauge transformations do not commute.

Table 1.1: The four fundamental forces of nature.

Force	Mediator
strong	gluon, g (0 mass)
Electromagnetic	Photon, γ (0 mass)
Weak	$W^{\pm}$ (82 GeV), and Z^0 (91 GeV)
gravitational	graviton G(0 mass)

a tube or colour string. The further the quarks move apart, the stronger the attractive force between them becomes. After a certain distance of separation the string breaks up into two where, at the end of each string, one finds a quark and an antiquark; the net effect is to create a new meson. In this manner, quarks are always confined and cannot be isolated.

The Fermi theory of the weak interaction has been superseded by the electroweak theory of Glashow–Weinberg–Salam (GWS) [15] which unifies the electromagnetic and weak forces. This theory is sometimes referred to as Quantum Flavour Dynamics (QFD). In this present view, the weak force is understood to be mediated by the intermediate vector bosons. There are in fact three such particles, two of which are charged ($W^{\pm}$), and the third is neutral (Z^0). The electromagnetic interaction is transmitted by the photon (γ).

Table 1.1 shows the four known fundamental forces of nature with their corresponding mediators.

1.4 The Standard Model

At the present time, all matter is considered to be composed of spin 1/2 objects known as *fermions*, of which there are two kinds: quarks and leptons. Three

families of quarks and leptons have been identified (see Table 1.2). The interaction between these material objects is via mediators which are particles of integral spin and are known as *bosons.*

The QCD sector of the strong interaction and the Glashow-Weinberg-Salam theory of the electroweak interaction provide a theoretical framework that is known as the Standard Model (SM) of particle physics; the mathematical basis for which is the group $SU(3)_c \otimes SU(2)_L \otimes U(1)_Y$. The $SU(3)_c$ part of the group differentiates between colour triplets of quarks, while $SU(2)_L$ distinguishes between the singlets of right-handed particles and the doublets of left-handed particles:

$$\begin{pmatrix} \nu_e \\ e^- \end{pmatrix}_L, \begin{pmatrix} u \\ d \end{pmatrix}_L \; ; \; e_R^-, u_R, d_R$$

$$\begin{pmatrix} \nu_\mu \\ \mu^- \end{pmatrix}_L, \begin{pmatrix} c \\ s \end{pmatrix}_L \; ; \; \mu_R^-, c_R, s_R$$

$$\begin{pmatrix} \nu_\tau \\ \tau^- \end{pmatrix}_L, \begin{pmatrix} t \\ b \end{pmatrix}_L \; ; \; \tau_R^-, t_R, b_R$$

and $U(1)_Y$ assigns hypercharge to the $SU(2)_L$ doublets and singlets.

1.5 High Energy e^+e^- Annihilation and the Hadronisation Process

In the early days of experimental high energy physics, one relied on high energy cosmic–ray interactions for the production of elementary particles. Subsequent

Table 1.2: The three generations of quarks and leptons. The top quark has not been discovered yet.

Generation	1	2	3	charge
Quarks (mass)	up (u) (4 MeV)	charm (c) (1.5 GeV)	[top (t)]	$+\frac{2}{3}$
	down (d) (7 MeV)	strange (s) (200 MeV)	beauty (b) (5 GeV)	$-\frac{1}{3}$
Leptons (mass)	e–neutrino (ν_e) (< 18 eV)	μ–neutrino (ν_μ) (< 0.25 MeV)	τ–neutrino (ν_τ) (< 35 MeV)	0
	electron (e) (0.51 MeV)	muon (μ) (106 MeV)	tau (τ) (1.8 GeV)	-1

technological advancement in charged particle accelerators has allowed a more controlled environment for the investigation of particle production than was possible with cosmic–rays.

In recent years, particle colliders have gained popularity. With these accelerators, beams of particles are accelerated in opposite directions and are then allowed to collide head–on. Provided one employs particle–antiparticle beams, all of the original quantum numbers are annulled, allowing the total energy of interaction to transform into new particles which can be entirely distinct from the original colliding particles. Figure 1.2 shows the basic diagrams where e^+e^- annihilate into fermion–antifermion final states. At very low centre–of–mass energies ($<<$91 GeV), the reaction proceeds via only the γ which then couples to charged fermions and antifermions: i.e. quarks and charged leptons. For high enough

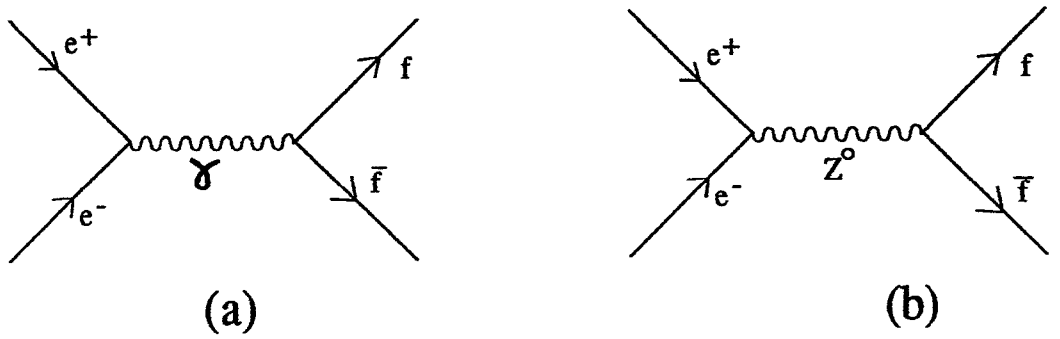

Figure 1.2: e^+e^- annihilation resulting in fermion–antifermion pairs mediated by a photon (γ) or a neutral intermediate vector boson (Z^0).

centre–of–mass energies, both the γ and the Z^0 mediate the reaction, with Z^0 coupling to all fermions and antifermions including neutrinos and antineutrinos [3].

The cross–section for this reaction has three components: an electromagnetic part, a weak part and the interference between the electromagnetic and the weak parts. The differential cross–section in the centre–of–mass is given by [16]

$$\begin{aligned}
\frac{d\sigma^{(e^+e^-\to f\bar{f})}}{d\cos\theta} &= \frac{d\sigma^{em}}{d\cos\theta} + \frac{d\sigma^{inter}}{d\cos\theta} + \frac{d\sigma^{weak}}{d\cos\theta} \\
&= \frac{N_c\pi\alpha^2 Q_f^2}{2s}(1+\cos^2\theta) \\
&- \frac{N_c\alpha Q_f G_F M_Z^2(s-M_Z^2)}{8\sqrt{2}[(s-M_Z^2)^2+M_Z^2\Gamma_Z^2]} \\
&\times [(R_e+L_e)(R_f+L_f)(1+\cos^2\theta)+2(R_e-L_e)(R_f-L_f)\cos\theta]
\end{aligned}$$

[3] At the Z^0 peak, the weak mechanism is favoured by as much as 1000 over the photon exchange.

$$+ \quad \frac{N_c G_F^2 M_Z^4}{64\pi[(s-M_Z^2)^2 + M_Z^2\Gamma_Z^2]}$$
$$\times \quad [(R_e^2+L_e^2)(R_f^2+L_f^2)(1+\cos^2\theta) + 2(R_e^2-L_e^2)(R_f^2-L_f^2)\cos\theta] \tag{1.3}$$

where $s = E_{cm}^2$ is the square of the center–of–mass energy, θ is the scattering angle of the fermion in the center–of–mass, M_Z is the mass of the Z^0, Γ_Z is the decay width of the Z^0, N_c (= 3 for quarks, = 1 for leptons) is the colour factor, Q_f is the charge of the fermion, G_F is the Fermi constant and $\alpha = \frac{e^2}{4\pi\hbar c}$ is the electromagnetic fine structure constant. L_f and R_f represent the left and right–handed coupling of the Z^0 to fermions and are given by:

$$R_f = -2Q_f \sin^2\theta_W$$
$$L_f = \tau_3 - 2Q_f \sin^2\theta_W$$

where θ_W is the Weinberg angle and $t_3 = \frac{1}{2}\tau_3$ is the third component of the weak isospin. The first term is the pure electromagnetic component, the second term is the interference term and the last term is the pure weak part. Figure 1.3 shows the integrated form of this cross–section for hadron and $\mu^+\mu^-$ production for various centre–of–mass energies. Table 1.3 gives the relative decay modes of the Z^0 to the various fermion–antifermion pairs.

The creation of hadrons in high energy e^+e^-annihilation proceeds via the process:

$$e^+e^- \rightarrow \gamma^*, Z^0 \rightarrow q\bar{q}(g....) \rightarrow \textit{hadrons} \tag{1.4}$$

where the created fermion–antifermion from the decay of the γ,Z^0 happen to be quark–antiquark pair accompanied by the emission of hard gluons, which are then acted upon by the strong force as they move apart. Each of these primary created

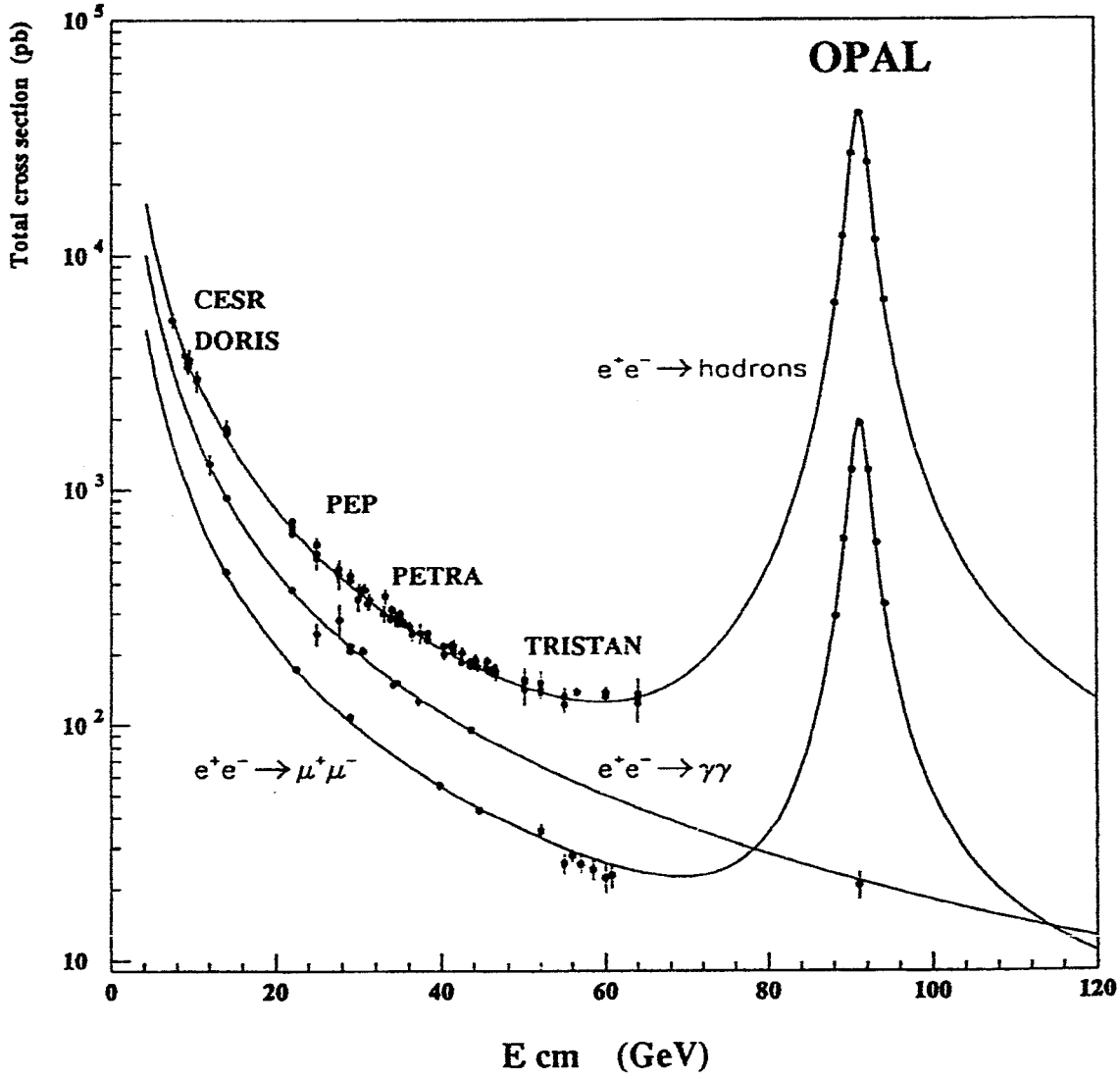

Figure 1.3: Fermion–antifermion cross–sections as a function of center–of–mass energy.

Table 1.3: The relative decay fraction of the Z^0.

Decay modes	Branching ratios(%) per decay mode
$\nu_e\overline{\nu_e}$, $\nu_\mu\overline{\nu_\mu}$, $\nu_\tau\overline{\nu_\tau}$	6.6%
e^+e^-, $\mu^+\mu^-$, $\tau^+\tau^-$	3.4%
$u\bar{u}$, $c\bar{c}$	12.1%
$d\bar{d}$, $s\bar{s}$, $b\bar{b}$	15.2%

partons then result in a "spray" of hadrons (i.e. a group of particles within some "narrow" cone) known as a "jet". In this process, additional soft (low energy) gluons are radiated and other quark–antiquark pairs are produced out of the vacuum. The mechanism responsible for this parton–to–hadron transformation is known as "hadronisation". This is the regime of non–perturbative QCD and is theoretically non–calculable. It is then necessary to rely on phenomenological models to describe the parton to hadron transition. This thesis will concentrate on studying certain aspects of these fragmentation models: namely the production characteristics of K^0. In the next chapter the process of fragmentation is discussed in some detail and the various approaches that are used to model it are examined.

Chapter 2

QCD Models of Hadronisation

Hadron production in high energy e^+e^- annihilation can be modelled in terms of two distinct steps: (i) the formation of an initial partonic state and (ii) the fragmentation (or hadronisation) of this partonic state into final observed hadrons. It is assumed that these two steps are independent (or at least have negligible interference), which subsequently allows one to handle them consecutively and separately.

The underlying reason for choosing to describe hadron production in the above manner lies in the momentum–transfer dependence of the "effective" coupling constant of the strong interactions, α_s. To first order in perturbation theory, this coupling constant is given by:

$$\alpha_s(Q^2) = \frac{12\pi}{(33 - 2N_f)\ln(\frac{Q^2}{\Lambda^2})} \tag{2.1}$$

where N_f is the number of quark flavours, Q is the magnitude of the 4–momentum transfer and Λ is a QCD scale [1].

For large Q values, α_s is small and a perturbative approach in terms of weakly interacting quarks and gluons is possible. This constitutes the initial step in the formation of primary partons.

Subsequently, these primary partons move away from the interaction region (which is normally accompanied by soft gluon emission) and fragment into the final

[1] Λ is a free parameter of the theory and is experimentally determined to be in the range of 0.15–0.25 GeV

hadrons. At these large distances from the region of creation of the initial partons, momentum transfers are small and the coupling constant is large. Here, perturbative QCD calculations are not possible. In dealing with this non–perturbative regime of QCD one must rely on phenomenological models to describe the parton fragmentation. In this chapter, various QCD models of hadronisation are introduced and their specific implementation in this work is discussed. Figure 2.1 shows the overall schematic of a typical e^+e^- annihilation with its subsequent hadronisation process. The primary quarks are formed at a scale Q. This is followed by QCD branching where more partons are formed and this showering continues until a scale Q_0 is reached. The process of hadronisation then converts the partons to hadrons at the QCD scale of Λ.

By experimentally studying the composition and the spectra of particles in hadronic final states, one refines these phenomenological models and gains insight into the non–perturbative nature of QCD. This ultimately may lead to the formulation of suitable non–perturbative methods. It is noted that studying non–perturbative aspects of QCD via e^+e^- annihilation ($e^+e^- \rightarrow q\bar{q} \rightarrow$ hadrons) has the advantage that it provides one with a well–defined initial parton state without any complication due to poorly known initial hadronic states.

The algorithmic implementation of the process $e^+e^- \rightarrow$hadrons that employs a particular model for hadronisation constitutes what is commonly known as as a "physics generator". In order to compare experimentally measured quantities with the prediction of these hadronisation models however, one needs in addition a full and reliable Monte Carlo (MC) simulation of the detector used in the experiment. The combination of the physics generator and the MC simulation of the detector provides a MC model which can then be used for direct comparison with

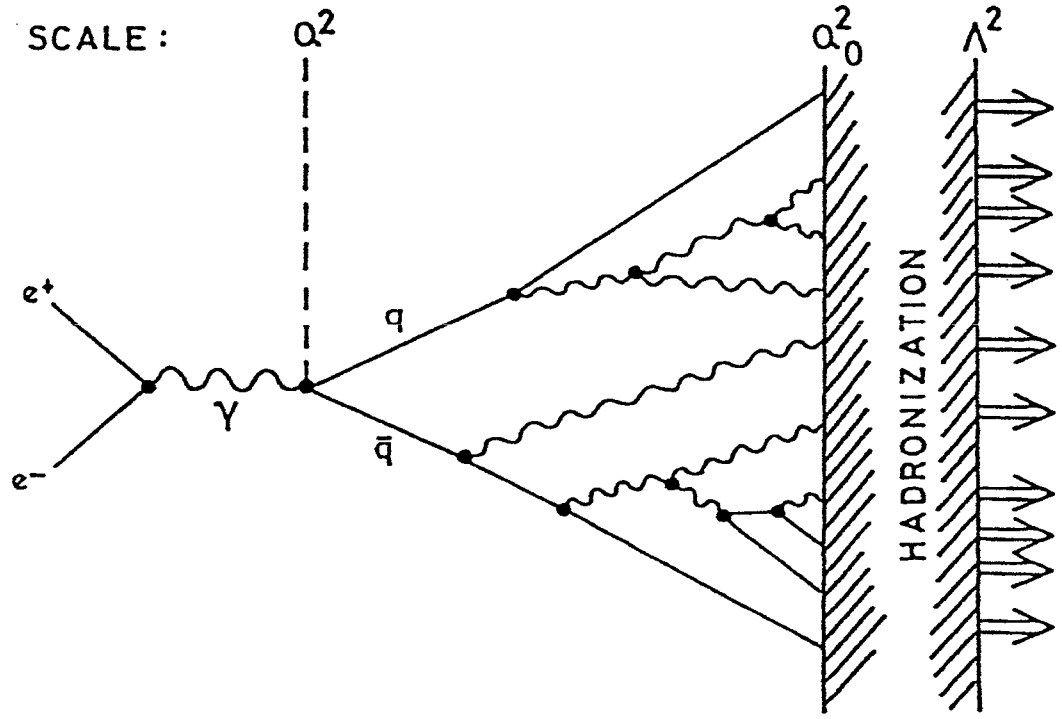

Figure 2.1: Schematic of a typical e^+e^- annihilation with the subsequent hadronisation process.

experiment.

2.1 Primary Parton Distributions

The generation of primary partons is governed by the perturbative regime of QCD. There are two classes of perturbative methods that are in current use to produce the primary partons: (i) the exact matrix element method and (ii) QCD shower models in the Leading Logarithmic Approximation (LLA).

With the matrix element method, the production cross–sections for "on–shell" [2] partons up to second order in QCD ($O(\alpha_s^2)$) have been exactly calculated [17]. In this manner, one uses a finite sum approximation to the infinite perturbative expansion involving $(\alpha_s)^n$ to estimate the number and the 4–momenta of the primary partons. With this approach, a maximum of 4 primary partons can be generated: 3 primary partons can be produced by a single gluon emission $e^+e^- \rightarrow q\bar{q}g$ while $e^+e^- \rightarrow q\bar{q}gg$ and $e^+e^- \rightarrow q\bar{q}q'\bar{q'}$ result in 4 primary partons. Figure 2.2 shows some of the Feynman diagrams relevant to this parton generation.

In the second approach, the parton distribution is formed by a shower process. The primary quarks are produced off–shell and decay into virtual partons (mostly gluons) via successive branchings ($q \rightarrow qg$, $g \rightarrow gg$, $g \rightarrow q\bar{q}$). As the branching progresses, the virtual masses decreases until a cut–off mass, Q_0, close to hadron mass (of the order of 1.0 GeV) is reached. The probabilistic picture for these branchings is defined by the Altarelli–Parisi equations [18]. Figure 2.3 is a schematic picture of shower evolution.

In the early days of such models, only those leading logs arising from collinear

[2] A particle is said to be "on–shell" if its calculated mass based on Einstein's mass–energy relationship ($m^2 = E^2 - p^2$) agrees with its rest mass. Otherwise it is referred to as "off–shell".

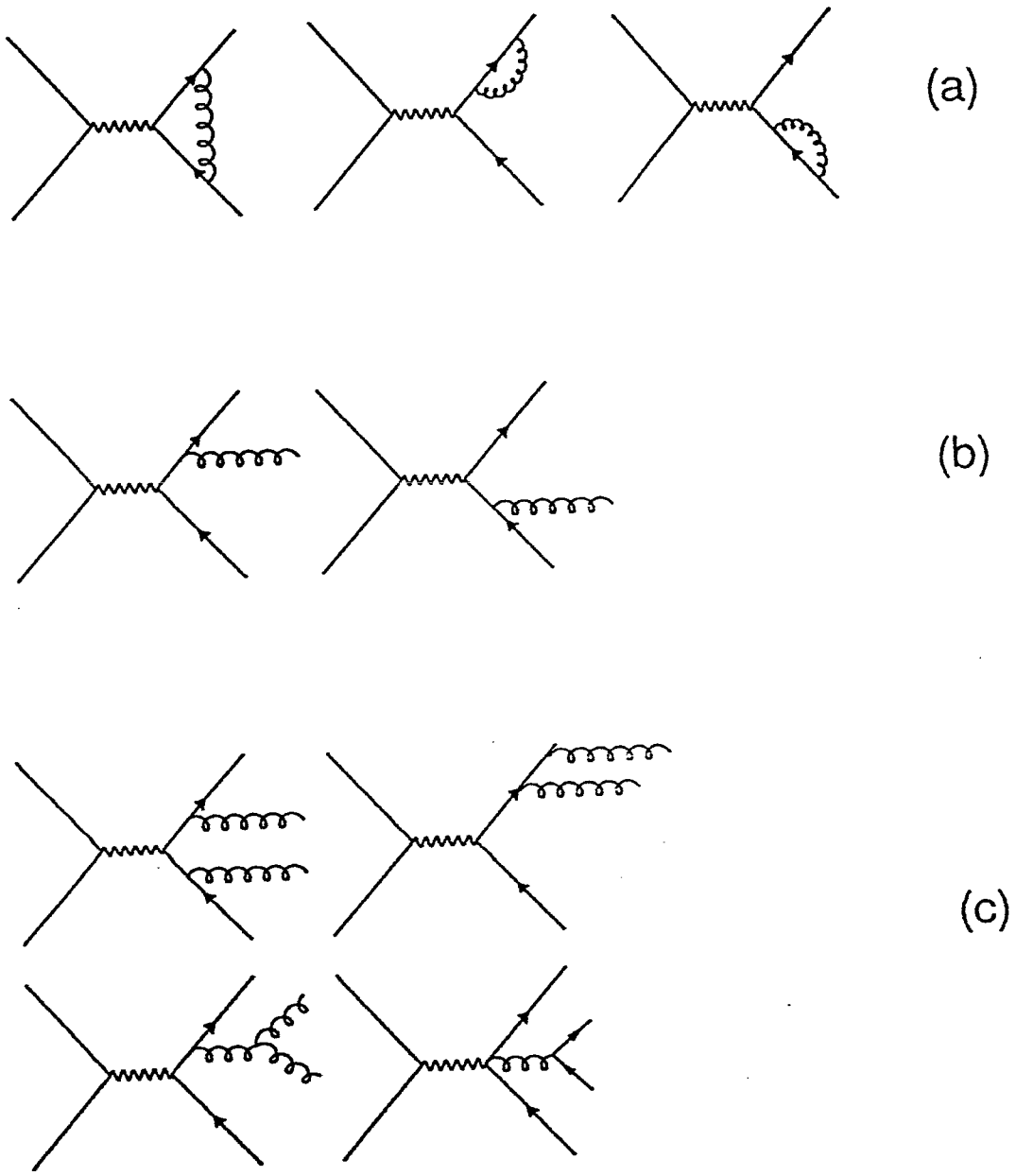

Figure 2.2: Feynman diagrams for parton generation. (a) first order correction for $q\bar{q}$, (b) first order $q\bar{q}g$ and (c) second order $q\bar{q}gg$ or $q\bar{q}q'\bar{q'}$.

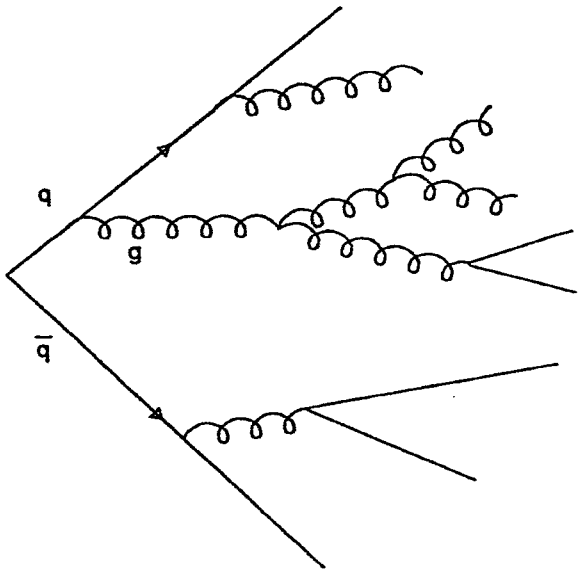

Figure 2.3: Schematic of the parton shower cascade.

divergences of perturbative QCD were included [19]. However, it has been shown more recently that the infrared (soft gluon) leading logs can also be summed, resulting in the destructive interference of soft gluons [20]. This has a simple probabilistic interpretation: soft gluons are emitted with uniformly decreasing opening angles in the shower cascade. This is known as angular ordering and reflects the coherent behaviour of emitted soft gluons.

2.2 Fragmentation Models

In the hadronisation process which follows the primary parton generation, one is dealing with momentum transfers of the order of the QCD scale ($Q \sim \Lambda$) where

the confinement property of the strong force takes over and converts the partons into hadrons. This section is devoted to the description of three phenomenological models that perform the task of bridging the gap and establishing the connection between the perturbative partons and the hadrons. The three models discussed are: the independent fragmentation model, the string model and the cluster model [21].

2.2.1 Independent Fragmentation Model

One of the earliest models of fragmentation was introduced for $e^+e^- \rightarrow q\bar{q}$ by Field and Feynman [22], and is known as the independent fragmentation (IF) model. In this model, the two original quarks decay independently of each other. The picture is sketched in Figure 2.4. The model is based on a recursive scheme where, at each step of the process, a $q'\overline{q'}$ pair is created out of the vacuum (with some of the original quark momentum) and a new meson is formed: $q \rightarrow M(q\overline{q'}) + q'$. The remaining quark q' does exactly the same and pulls another quark–antiquark pair out of the vacuum. The iteration continues until there is insufficient energy to proceed with the cascade. With this scheme, energy and momentum are not necessarily conserved and have to be imposed at the end of the fragmentation process. The process is normally parametrised in terms of a fractional energy and momentum that is imparted to the meson. Let z be this fraction :

$$z = (E + p_{||})_{meson}/(E + p_{||})_{Quark} \tag{2.2}$$

where $p_{||}$ is the momentum component parallel to the direction of the original quark and E is the energy. Then if $D(z)$ is the probability density function (fragmentation function) for producing a meson with energy and momentum fraction z, one may

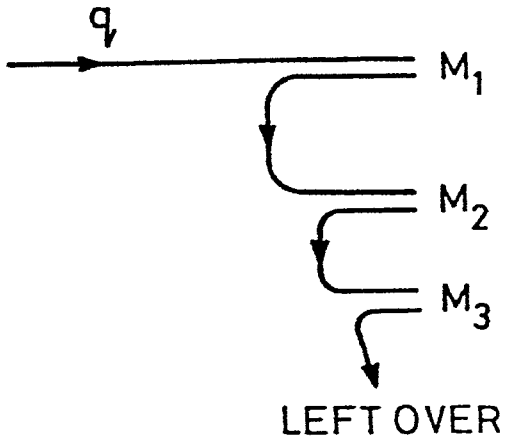

Figure 2.4: Schematic of the independent fragmentation model.

write [22], [23]:

$$D(z) = f(z) + \int_z^1 f(1-z')D(\frac{z}{z'})\frac{dz'}{z'} \tag{2.3}$$

where $f(z)$ is an arbitrary normalised function [3] known as the scaling (or the splitting) function which governs the fraction of energy and momentum transfer at each branch point [4]. When the production of different flavours is taken into account, one has a more general version of the above integral equation (see B.

[3] $f(z)$ satisfies the normalisation condition $\int_0^1 f(z)dz = 1$

[4] The original Field–Feynman function was $f(z) = (1-a) + 3a(1-z)^2$, with parameter a to be determined from experiment.

Andersson et al. [24]):

$$D_q^h(z) = f_q^h(z) + \int_z^1 \sum_{q'} f_q^{q\bar{q}'}(1-z') D_{q'}^h(\frac{z}{z'})\frac{dz'}{z'} \tag{2.4}$$

where h is a hadron and q and q′ are quark flavours. The f's are now normalised according to:

$$\sum_{q'} \int_0^1 f_q^{q\bar{q}'}(z)dz = 1 \tag{2.5}$$

The independent fragmentation model has failed to predict the observed "string effect"[5] in three jet events [25]. At the present time, string fragmentation models and cluster models are the favoured fragmentation models and will be the subject of the rest of this chapter.

2.2.2 The String Fragmentation Model

The basic starting idea for such models is the concept of a "string". In QCD, one expects a linear confinement behaviour at large distances which is expressed in terms of a string with constant tension that connects the quark and the antiquark with an associated confining force $F \propto \kappa\, r$, where κ ($\sim$ 1 GeV/fm) is the string constant and r is the separation distance.

A fragmentation model based on this classical concept was first proposed by Arturu and Mennessier in 1974 as a $(1+1)$ dimensional model [26]. As the quark and the antiquark move apart the energy in the colour field increases until it is energetically favourable to produce a new quark–antiquark pair out of the vacuum. At this time, the string breaks. This process continues until there is too little energy in the string to create a new quark–antiquark pair out of the

[5] In three jet events, the study of energy flow and angular distribution in the event plane has shown a depletion in the production of hadrons opposite to the gluon jet (i.e. in the region between q and $\bar{q}$) compared to the prediction of the independent fragmentation model.

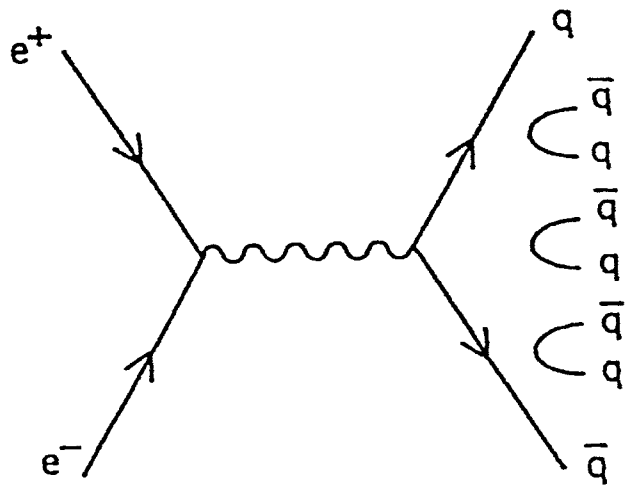

Figure 2.5: Schematic of the string fragmentation process.

vacuum. The left over strings are then the stable mesons. This is schematically shown in Figure 2.5. *In contrast to the independent fragmentation where individual partons fragment, with the string fragmentation (SF) model, hadronisation results from the break up of the string that joins the partons.* The process of generation of quark–antiquark pairs out of the vacuum is invoked in terms of a quantum mechanical tunnelling process [27] with a probability which is proportional to:

$$\exp\left(-\frac{\pi m^2}{\kappa}\right)\exp\left(-\frac{\pi p_T^2}{\kappa}\right) = \exp\left(-\frac{\pi m_T^2}{\kappa}\right) \tag{2.6}$$

where m is the rest mass of the produced quark (or antiquark), p_T is the transverse momentum of the produced quark (or antiquark) perpendicular to the direction

of the original quark and m_T ($m_T^2 = m^2 + p_T^2$) is known as the transverse mass. The mass–dependence of the above probability implies a suppression for heavier quark production in the following ratios: u:d:s:c≈1:1:0.3:10^{-11}. This means that charm and heavier quarks are not produced in the soft fragmentation process. The strangeness suppression factor (with the default value of 0.3), γ_s, is left as a free parameter. Within this model, the pseudoscalar to vector meson production rates are also treated as arbitrary parameters to be determined experimentally. The above formula imposes a flavour–independent Gaussian spectrum for the transverse momentum of the generated quark–antiquark pair and in this way provides transverse momentum to the jets.

The $q\bar{q}$ pairs are formed such that energy and mass are conserved at each step. For simplicity, consider the $(1+1)$ dimensional model with space coordinate x and time coordinate t. Then, if a $(q_1, \bar{q}_1)$ pair is generated at (x_1, t_1) and a $(q_2, \bar{q}_2)$ pair is generated at (x_2, t_2), the energy and momentum of the produced meson is given by (see B. Andersson et al. [24]):

$$\begin{aligned} E(q_1, \bar{q}_2) &= \kappa(x_2 - x_1) \\ p(q_1, \bar{q}_2) &= \kappa(t_2 - t_1) \end{aligned} \tag{2.7}$$

The requirement that the meson is to have a mass m implies that the hadronisation point must lie on a hyperbola in space–time:

$$(x_2 - x_1)^2 - (t_2 - t_1)^2 = \frac{m^2}{\kappa^2} \tag{2.8}$$

Figure 2.6 shows schematically the space–time evolution of a one–dimensional string and the hatched areas represent the regions of non–vanishing field.

Baryon production can be incorporated in terms of diquark pair production out of the vacuum: $(qq - \overline{qq})$. However, due to the higher diquark mass as com-

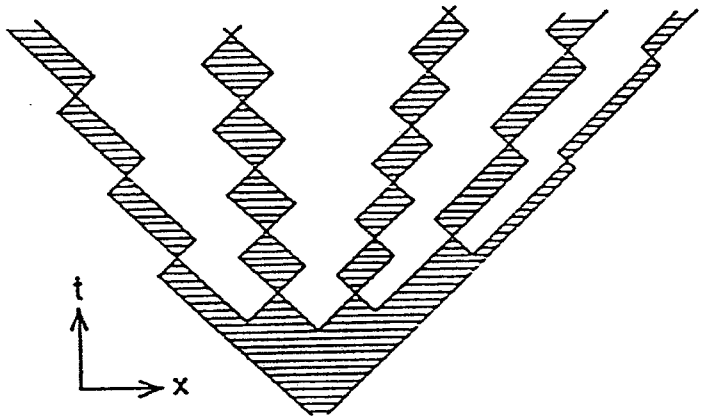

Figure 2.6: Schematic of space–time evolution of a one dimensional string.

pared to a single quark, baryon production is suppressed. An alternative method of baryon production is in terms of the so called "popcorn" mechanism, where a meson is created between the baryon and the antibaryon. Figure 2.7 shows the schematic of baryon production in the string model.

The string model used in this thesis was developed by the LUND group [24] with its specific implementation of JETSET 7.2 using parton shower generation. The major conceptual advance introduced by the LUND group was their treatment of a gluon jet as a kink on the string. This amounts to having a geometry where one section of the string is connecting qg and the other $\bar{q}g$. This method of accommodating hard gluon radiation accounts for the observed string effect pre-

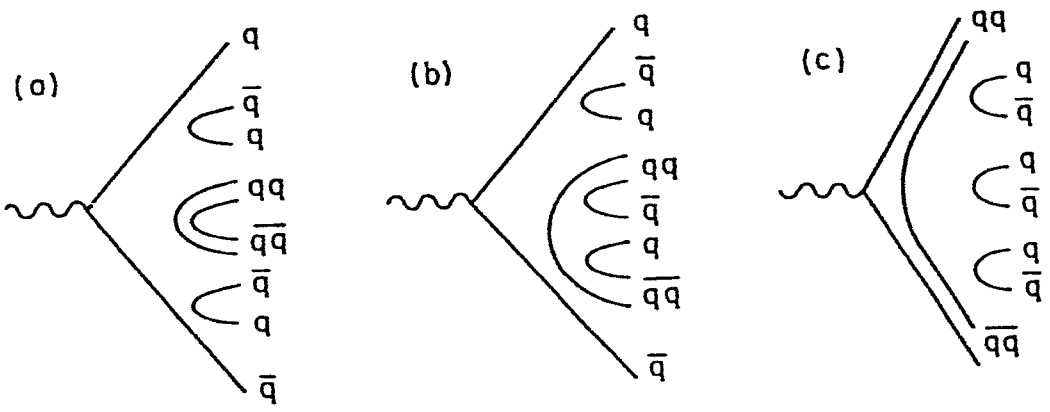

Figure 2.7: Schematic of baryon production via (a)diquark formation, (b) popcorn mechanism and (c) leading diquark formation.

viously discussed. Figure 2.8 compares the decay of a $q\bar{q}g$ event as seen in the independent and the string fragmentation models [6]. As pointed out before, with the independent fragmentation model individual partons (quark, antiquark and gluon) fragment individually. In the string fragmentation model, hadronisation results from the break up of the string that joins the gluon to the quark and the antiquark; this results in a depletion of the produced hadrons in the region between the quark and the antiquark which is known as the "string effect."

[6]Despite their conceptual differences, the independent fragmentation model and the string fragmentation model provide similar description for $e^+e^- \rightarrow q\bar{q}$ events. As has been observed however, the two methods predict differences in properties of 3 jet events $q\bar{q}g$ which relates to the difference in which hard gluon emission is treated in the two models.

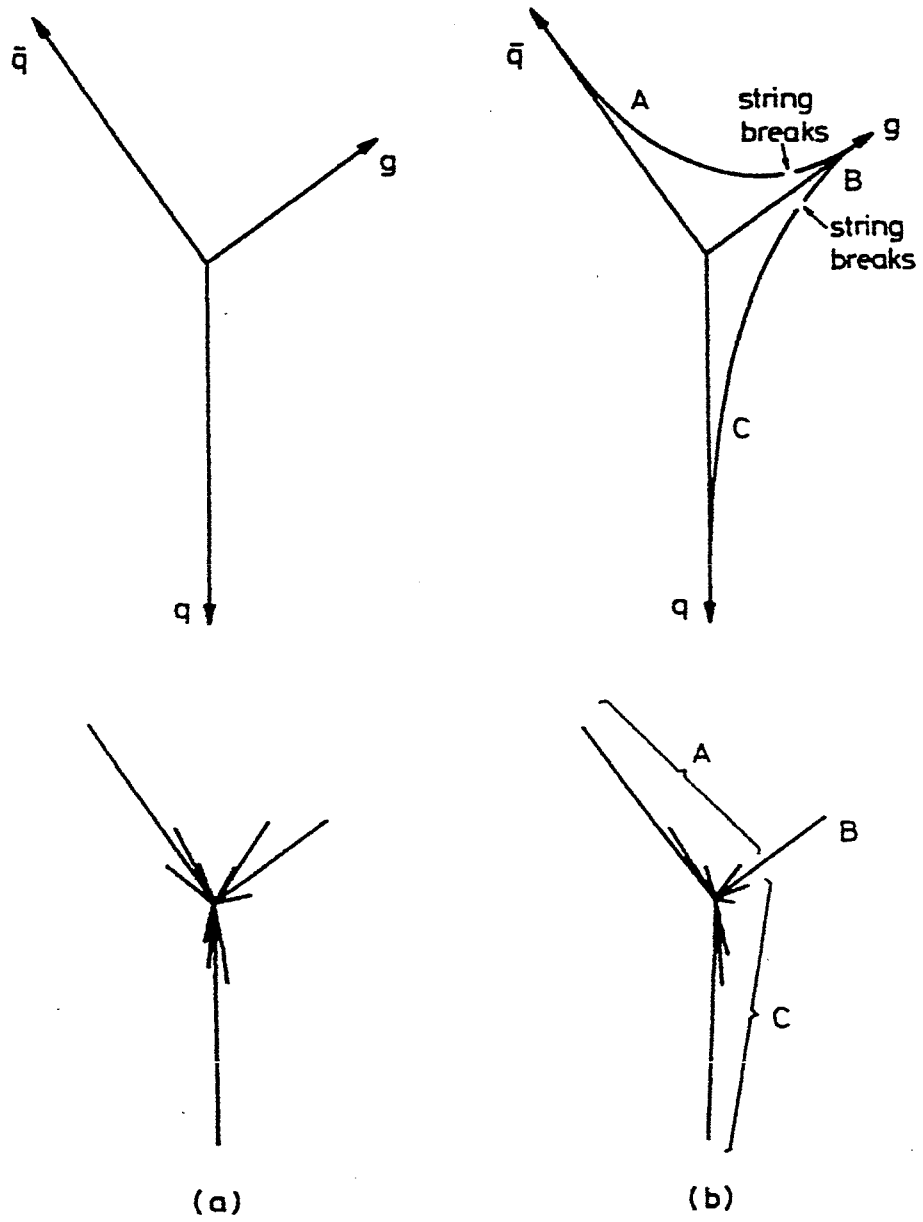

Figure 2.8: Schematic of the fragmentation for a 3 jet ($q\bar{q}g$) event in (a) independent fragmentation model and (b) string fragmentation model.

Table 2.1: Default and optimised values of some JETSET parameters which determine momentum distribution and strange particle multiplicity. Λ_{LLA} is the QCD scale while Q_0 is the cut–off mass for the parton shower generation. a and b are the symmetric LUND fragmentation function parameters.

Parameter	Monte Carlo name	Default value	Optimised value
Λ_{LLA}	PARJ(81)	0.4 GeV	0.29 GeV
Q_0	PARJ(82)	1.0 GeV	1.0 GeV
a	PARJ(41)	0.50 GeV	0.18 GeV
b	PARJ(42)	0.90 GeV^2	0.34 GeV^2
σ_q for p_T	PARJ(21)	0.35 GeV	0.37 GeV
γ_s	PARJ(2)	0.3	0.3

The symmetric LUND model is formulated as an iterative cascade process in terms of a left–right symmetric splitting function which regulates the transfer of momentum to a newly formed quark given by:

$$f(z) = N\frac{(1-z)^a}{z}\exp\left(-\frac{bm_T^2}{z}\right) \tag{2.9}$$

where z is the fraction of $(E + p_{\|})$ for the meson, m_T is its transverse mass and N is a normalisation constant. The parameters a and b are tunable.

Table 2.1 shows those default values and optimised values (as used in this thesis work) for JETSET 7.2 which control the momentum distribution and strange particle multiplicity. The optimised values have been obtained by requiring compatability between the global features of the data and the MC [28]. This matter is further discussed in chapter 4 which deals with data selection.

2.2.3 The Cluster Models

In cluster models, the long, ordered, fragmentation chains as present in the independent and the string fragmentation models are replaced by colour neutral

"clusters" which are regarded as the basic units for hadron production. Each produced cluster decays directly into primary hadrons and so no recursive scheme is necessary for the implementation of such models.

The cluster model used in this work is due to Marchesini and Webber [20] with the specific implementation as a computer program known as HERWIG [21]. In this model parton showers are initiated with the LLA approach. The model also incorporates the effects of soft gluon interference which results in the angular ordering of these soft gluons.

The hadronisation in such models proceeds in three steps. Initially each of the final gluons resulting from the QCD shower process is branched non–perturbatively into $q\bar{q}$ pairs [7]. In the second stage, neighbouring quark–antiquark pairs are combined into colour–neutral low mass (i.e. hardron–like) objects known as clusters, which are characterised by their 4–momenta and the flavour content of the constituent quark and antiquark [8]. Finally, these clusters decay isotropically into hadrons, weighted according to phase space. Figure 2.9 shows the schematic of hadron production in the cluster model.

Clusters may decay into hadrons by two possible mechanisms: either a one–body decay or a two–body decay with the choice based on the flavour content and the mass value of the cluster. Consider a cluster C with the flavour composition, $(q_1, \bar{q}_2)$ and mass, M_C. It could decay into two hadrons:

$$C(q_1, \bar{q}_2) \rightarrow h_1(q_1, \bar{q}_f) + h_2(q_f, \bar{q}_2) \tag{2.10}$$

where q_f is taken to be any of the five possible quark flavours (the top quark is excluded) with equal probabilities. For the above process to proceed, the chosen

[7] Such a splitting of gluons is performed in order to separate the two colour indices of the gluon, allowing the formation of colour–neutral clusters.

[8] A cluster may have a diquark as its constituent parton.

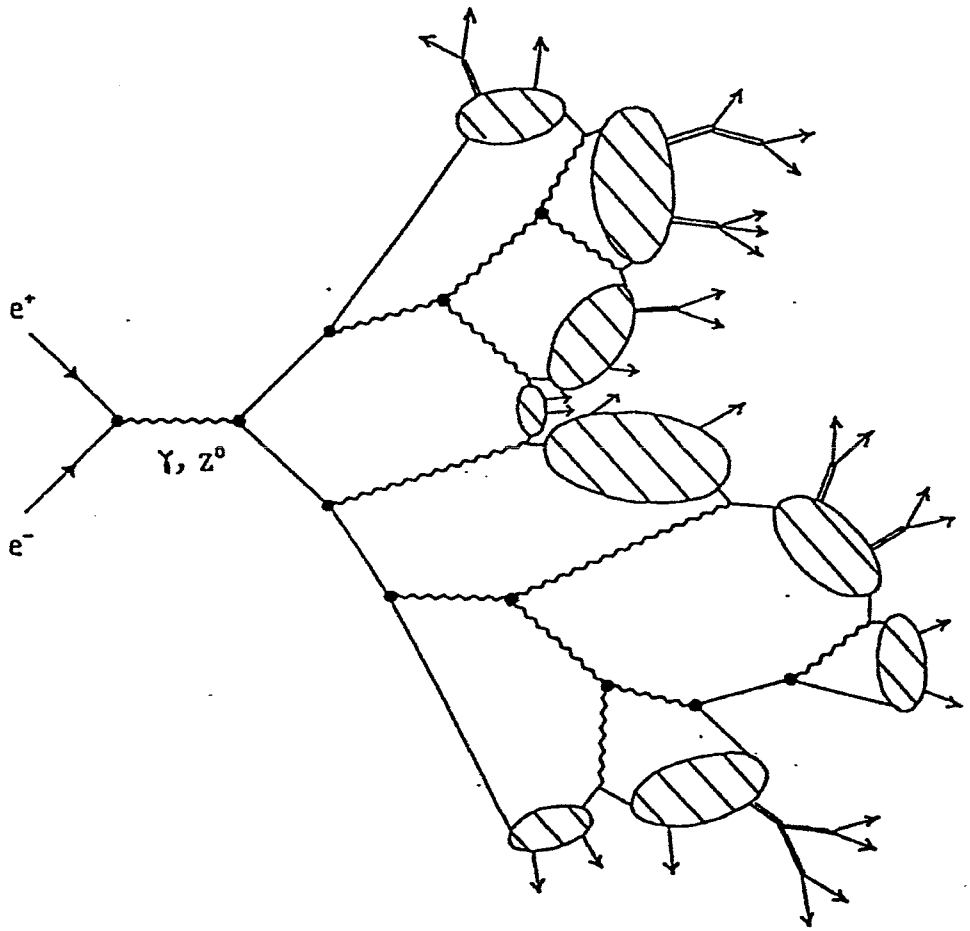

Figure 2.9: The schematic of the hadronisation process as viewed in the cluster model.

flavour q_f must satisfy the following threshold mass cut:

$$M_C > [m_1(q_1, \overline{q_f})]_{lightest} + [m_2(q_f, \overline{q_2})]_{lightest} \tag{2.11}$$

where $[m_1(q_1, \overline{q_f})]_{lightest}$ and $[m_2(q_f, \overline{q_2})]_{lightest}$ are the masses of the *lightest* hadrons with the given flavour composition. Furthermore, the probability of a given selection is given by the kinematical phase–space weight and the spin–degeneracy of the two hadron daughters: $(2S_1 + 1)\ (2S_2 + 1)$, where S_1 and S_2 are the spins of the hadrons h_1 and h_2.

If $C(q_1, \overline{q_2})$ does *not* satisfy this mass inequality, then it will transform via the one–body process into a single hadron. In this process the value of the 3–momentum of the parent is equal to that of the daughter hadron and the difference between their energies is transferred randomly to a neighbouring site.

The mass scale involved in cluster formation is determined by the shower cut–off mass, Q_0, which determines when the showering process is terminated. This cut–off is rather arbitrary and is treated as a free parameter in the model. Typical cluster masses are normally two or three times Q_0, i.e. in the range 0 to a few GeV. It is however possible for a cluster to be formed with a very large mass. Such massive clusters are first decomposed into lighter clusters before the above cluster decay mechanism to hadrons is applied. A cluster is deemed anomalously heavy if its mass satisfies the following inequality:

$$M_C > M_{max}^2 + (m_{q_1} + m_{\overline{q_2}})^2 \tag{2.12}$$

where m_{q_1} and $m_{\overline{q_2}}$ are quark rest masses and M_{max} is a phenomenological parameter of HERWIG. It is effectively the maximum kinetic energy available to hadrons in the isotropic cluster decay.

Table 2.2: Default values of some HERWIG parameters which determine momentum distribution.

Parameter	Monte Carlo name	Default value
Λ_{LLA}	QCDLAM	0.2 GeV
Gluon Q_0	VGCUT	0.06 GeV
Quark Q_0	VQCUT	0.48 GeV
M_{max}	CLMAX	3.5 GeV

Table 2.2 shows the default values for the HERWIG 5.0 parameters controlling the momentum distribution of hadrons. It is noted that the baryon production rate is critically dependent on the maximum allowable cluster mass, CLMAX. For example, changing CLMAX from 3.5 GeV to 3.0 GeV reduces the Λ baryon production rate by a factor of 2 approximately whereas both the charged track and the K^0 multiplicity are rather insensitive to this change.

2.3 Predictions for K^0 and Other Particles

In order to study various aspects of hadronisation relating to K^0 production, one must make a comparison between those aspects determined by the data and those expected from the different Monte Carlo models. For these comparisons, it is desirable to have the different Monte Carlo models provide one with similar inclusive [9] momentum spectra.

In the case of JETSET, such spectra are ultimately determined by the phenomenological aspects of the hadronisation such as the transverse momentum, the strangeness suppression factor and the ratio of the strange pseudoscalar to vector meson production. In the case of HERWIG, with its very compact description

[9] An inclusive reaction for the production of K^0 is: $e^+e^- \rightarrow \gamma, Z^0 \rightarrow K^0 + X$, where X could be anything.

of event generation, the spectra are determined by the cluster phase space decay aspects of the model.

K^0 mesons typically arise from 3 sources in e^+e^- annihilation. They can be created as *first rank hadrons* containing the primary s or $\bar{s}$ quarks resulting from $e^+e^- \rightarrow s\bar{s}$. They could also originate from the weak decay of the hadrons that are formed from the heavier flavour primary quarks: $e^+e^- \rightarrow c\bar{c}$ or $e^+e^- \rightarrow b\bar{b}$; the example decays are: $D^0 \rightarrow \overline{K^0}\pi^+\pi^-$, $D^+ \rightarrow \overline{K^0}\pi^+$ and $B^0 \rightarrow K^0 J/\psi$, $B^+ \rightarrow K^0\pi^+$. Finally, they can be produced in the QCD shower process. As a result, this makes K^0 a very useful probe in fragmentation studies. The contribution of these various sources to the (JETSET) inclusive production cross–section for the K^0 as a function of the scaled energy variable [10] is shown in Figure 2.10. It is seen that at low x_E values ($x_E < 0.1$), the charm and beauty sources are orders of magnitude smaller than the strange source. The charm and beauty sources also exhibit a harder fragmentation distribution. Figure 2.11 shows the (JETSET) inclusive production cross–section for for the five possible primary quark flavours at the Z^0. It is observed that at low x_E values ($x_E < 0.1$) all flavours have similar contributions while at large x_E values, the strange quark is the largest contributor. Figure 2.12 shows the normalised inclusive momentum spectrum for the production of K^0. One observes a very good agreement between the two generated distributions for HERWIG and JETSET. The average momentum of the produced K^0 is: $\langle P_{K^0} \rangle = 4.4$ GeV/c. This momentum corresponds to a mean decay length [11] of $\Lambda_{K^0} = 23.7$ cm.

Table 2.3 shows the predicted multiplicities for some particles by both the

[10] The scaled energy variable $x_E = 2E/\sqrt{s}$, where E is the energy of the particle and $\sqrt{s}$ is the centre–of–mass energy. $\beta = p/E$, where p is the momentum of the particle.

[11] The mean decay length in flight for K^0 is defined as $\Lambda_{K^0} = \frac{p}{m}(c\tau_0) = \frac{4.4}{0.4976}(2.675) = 23.7$ cm, where p is the momentum of the K^0 in the laboratory and m is its rest mass.

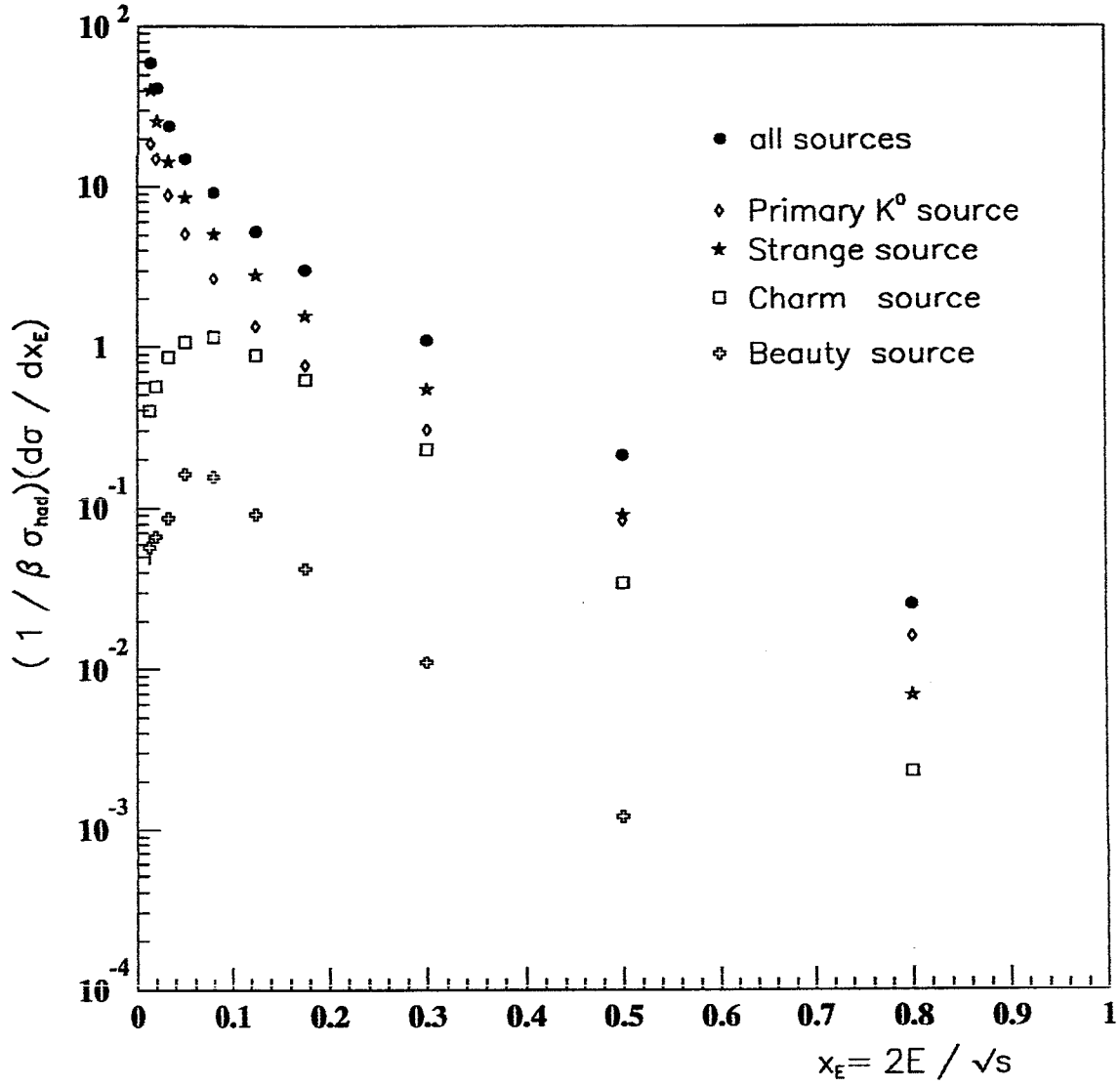

Figure 2.10: Production cross–section for K^0 meson from various sources.

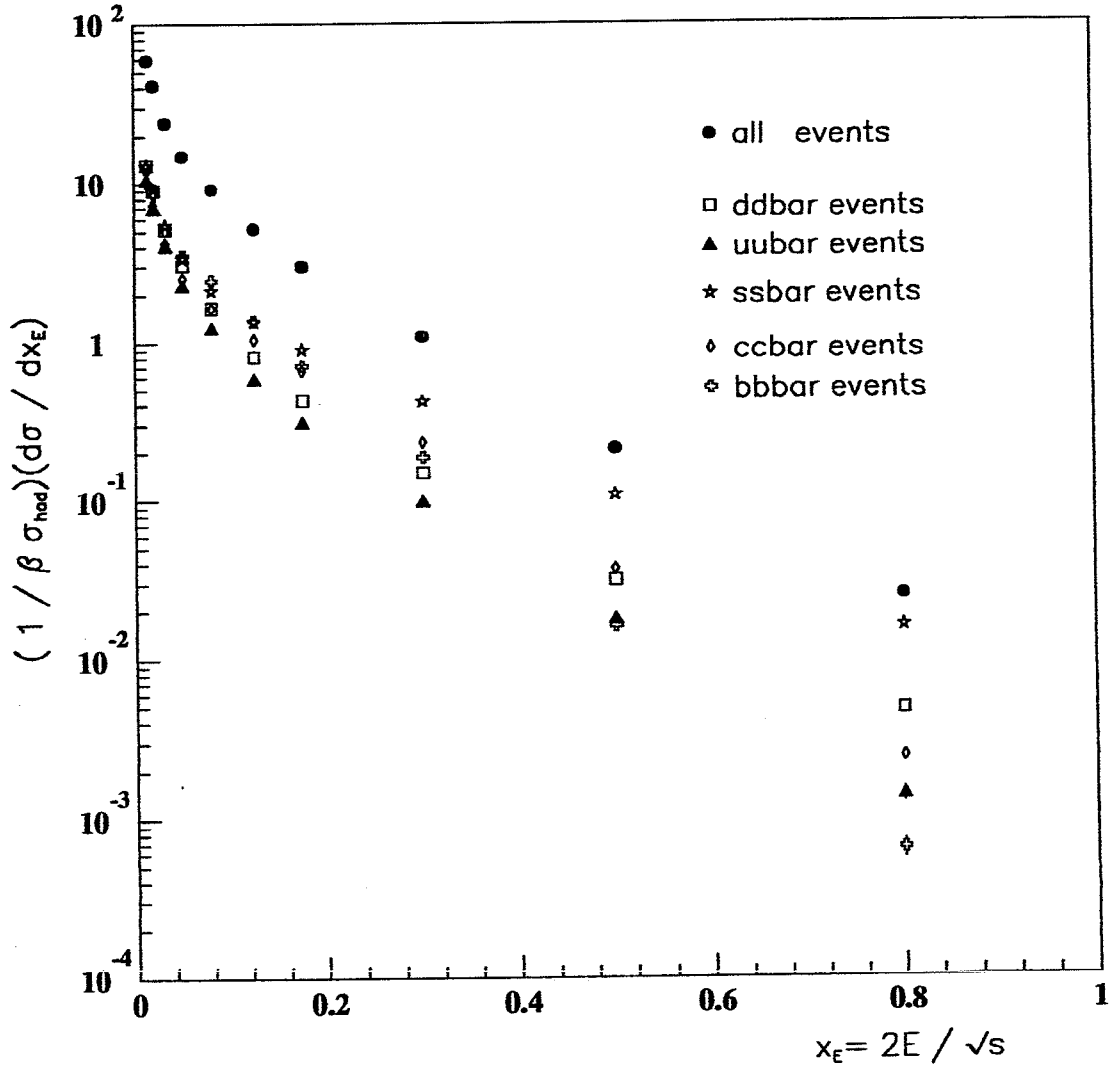

Figure 2.11: Production cross–section for K^0 meson for the five possible primary (quark, antiquark) pairs.

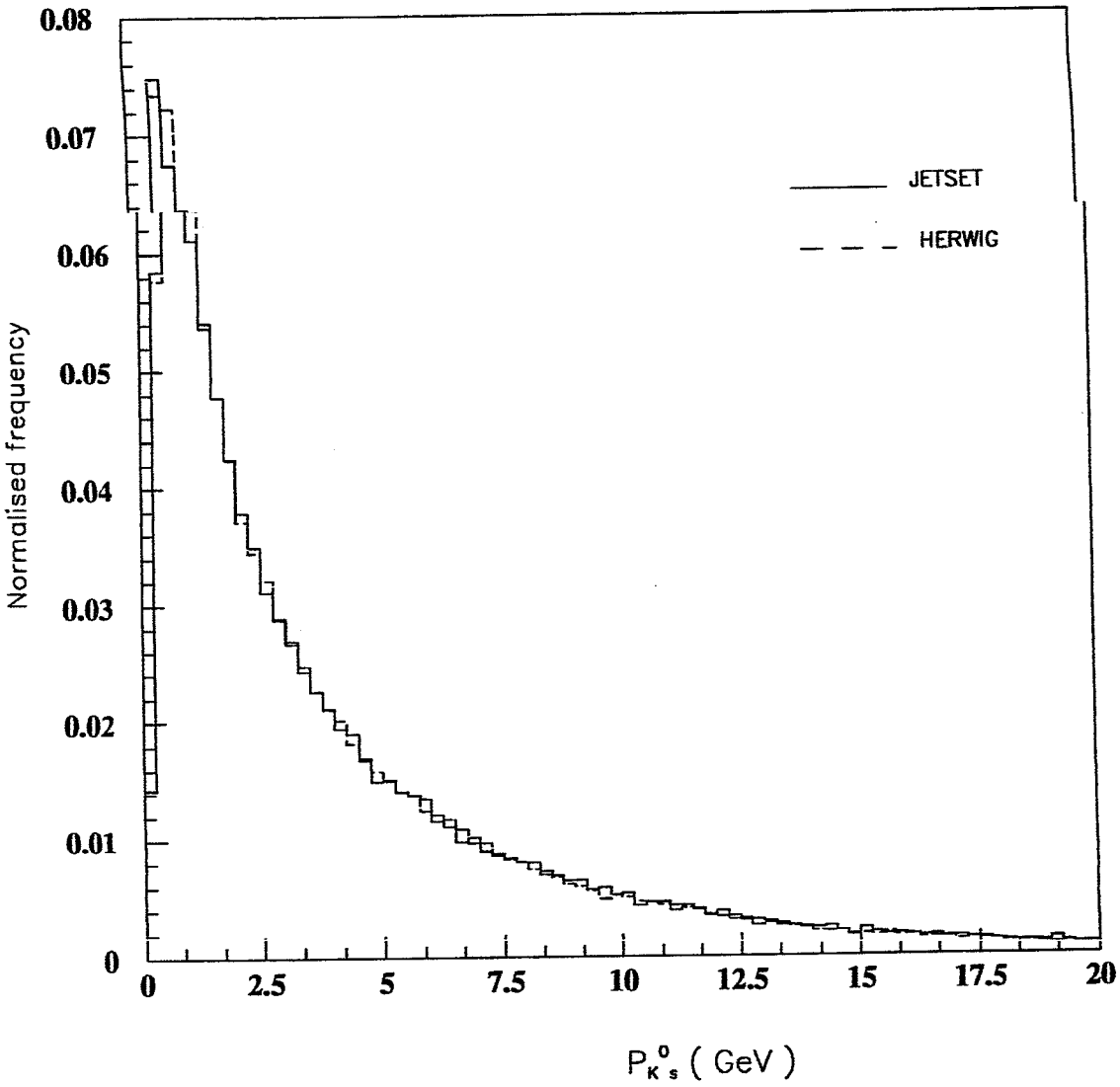

Figure 2.12: Inclusive momentum distribution for K^0 as predicted by JETSET and HERWIG.

tuned JETSET and HERWIG. It it noted that even though the inclusive production rate for K^0 for the two models agree relatively well, their predicted rates for the vector mesons are quite different. JETSET is equipped with a tunable parameter, designated as V/(P+V), which determines the probability of the vector meson production relative to the pseudoscalar meson production. More is said about the tuning of this parameter using the measured rate for vector meson production in section 6.5.

Lastly, it is noted that tensor meson production has been incorporated in HERWIG such that production of particles such as $K_2^*(1430)$ can be studied. In its present form JETSET, lacks such capability.

2.4 Summary

The hadronisation process was discussed and the three phenomenological models used to describe it have been considered. The two models that will be utilised in the analysis section of this thesis are the string fragmentation model and the cluster model, with their specific implementation in the form of computer programs JETSET 7.2 and HERWIG 5.0, respectively.

Table 2.3: JETSET and HERWIG predicted multiplicities for some particles. The statistics is based on 100,000 generated events.

Particle	JETSET	HERWIG
K^0, $\overline{K^0}$	2.154	2.071
K^{*0}	1.060	0.771
$K^{*+/-}$	1.099	0.822
Λ^0,$\overline{\Lambda^0}$	0.386	0.427
$\pi^{+/-}$	17.353	17.313

Chapter 3

The Experimental Background

3.1 Some Historical Perspectives

Experimental high energy particle physics has its origins in cosmic–ray physics. High energy cosmic rays impinging upon the Earth's upper atmosphere act as projectiles, splitting nucleons and producing elementary particles.

In order to imitate high energy processes initiated by cosmic rays, one could alternatively accelerate charged particles (usually protons or electrons) to high energies and utilize them as the projectile particles. This can be achieved by having the particles traverse an accelerating voltage many times, each time receiving a small "kick" and a correspondingly small increase in their kinetic energy. This technique of gradual acceleration (instead of one big "push") constitutes the underlying principle for all of the modern particle accelerators.

In very broad terms, a typical high energy particle physics experimental set–up consists of two main components: an accelerator, to create the high–energy process of interest to be studied, and a detector to "record" it for subsequent detailed analysis. The subject matter of this thesis is concerned with one such high energy particle physics experiment carried out at the **LEP** (Large Electron Positron) collider using the **OPAL** (Omni Purpose Apparatus for LEP) detector.

Before embarking on a detailed description of the LEP collider and the OPAL detector, this section is concluded by a very short summary of the historical de-

velopment of e^+e^- (positron–electron) storage rings [29]. In what follows, CM stands for Centre of Mass.

- The "first generation" e^+e^- storage rings became operational in the period 1963–1967 in Italy, USA, USSR, and France, operating in the CM energy range of 1–7 GeV.

- The larger "second generation" machines were built in the early 1970s. These were, **SPEAR** (the Stanford Positron Electron Accelerating Ring) at **SLAC** (the Stanford Linear Accelerator Centre) and **DORIS** (Double RIng Storage) at **DESY** (the Deutches Electronen SYnchrotron), in Hamburg, Germany. Both achieved a total energy of about 9 Gev and possessed better energy resolution. More sensitive detectors were designed to take advantage of this new improved mass resolution.

- The "third generation" of these storage rings appeared towards the end of the 1970s, including: **PETRA** (Positron–Electron Tandem Ring Accelerator) at DESY (CM energy of 38 GeV, later upgraded to 46 GeV), **CESR** (Cornell Electron Synchrotron Ring) at Cornell University, USA (CM energy of 16 GeV), and **PEP** (Positron Electron Project) at SLAC (CM energy of 36 GeV).

- The "present generation" of e^+e^- colliders has pushed energies to even higher levels. The earliest to become operational (1987) was **TRISTAN** at **KEK** (Ko–Enerugie butsurigaku Kenkyusho) in Japan with a CM energy of 60 GeV. This was followed by **SLC** (Stanford Linear Collider) at SLAC and LEP at **CERN** (Centre Europeén pour la Recherche Nucléaire). LEP was conceived

as a conventional circular accelerator, while SLC is a hybrid accelerator employing both the linear and the collider accelerator concepts. With SLC, beams of e^+ and e^- are accelerated in SLAC's 2–mile linear accelerator. The two beams are then separated into distinct arcs and are made to collide head–on at one collision point. Both of these accelerators possess a CM energy of 100 GeV and act as Z^0–factories.

3.2 The LEP Collider

3.2.1 The Main Ring

The LEP collider (phase–1, CM energy of 100 GeV) was designed as a Z^0–factory with the aim to study the production and decay processes of the neutral intermediate vector boson (Z^0) of the weak interaction. Its expected upgrade (phase–2, CM energy 200 GeV) by the mid 1990s, would allow direct observation/investigation of W^+W^- pair–production. At the present time, LEP is the largest particle collider of its kind, and is expected to remain so until the late 1990s. It became operational in the summer of 1989 [30].

LEP is an underground ring–shaped tunnel with a circumference of 27 km and a tunnel diameter of 3.8 m. It passes through both French and Swiss territories (three quarters of it lying in France) and is situated near Geneva, Switzerland. The schematic is shown in Figure 3.1. The other 3 experiments at LEP are ALEPH, L3 and DELPHI. The ring is not a perfect circle but is made up of eight 2800 m curved sections, linked by straight sections, forming an octagon. Electron and positron beams that have been pre–accelerated, are injected into the LEP ring and are made to circulate in opposite directions, with electrons anti–clockwise. In the curved section of the ring, the electrons and positron beams are guided on their

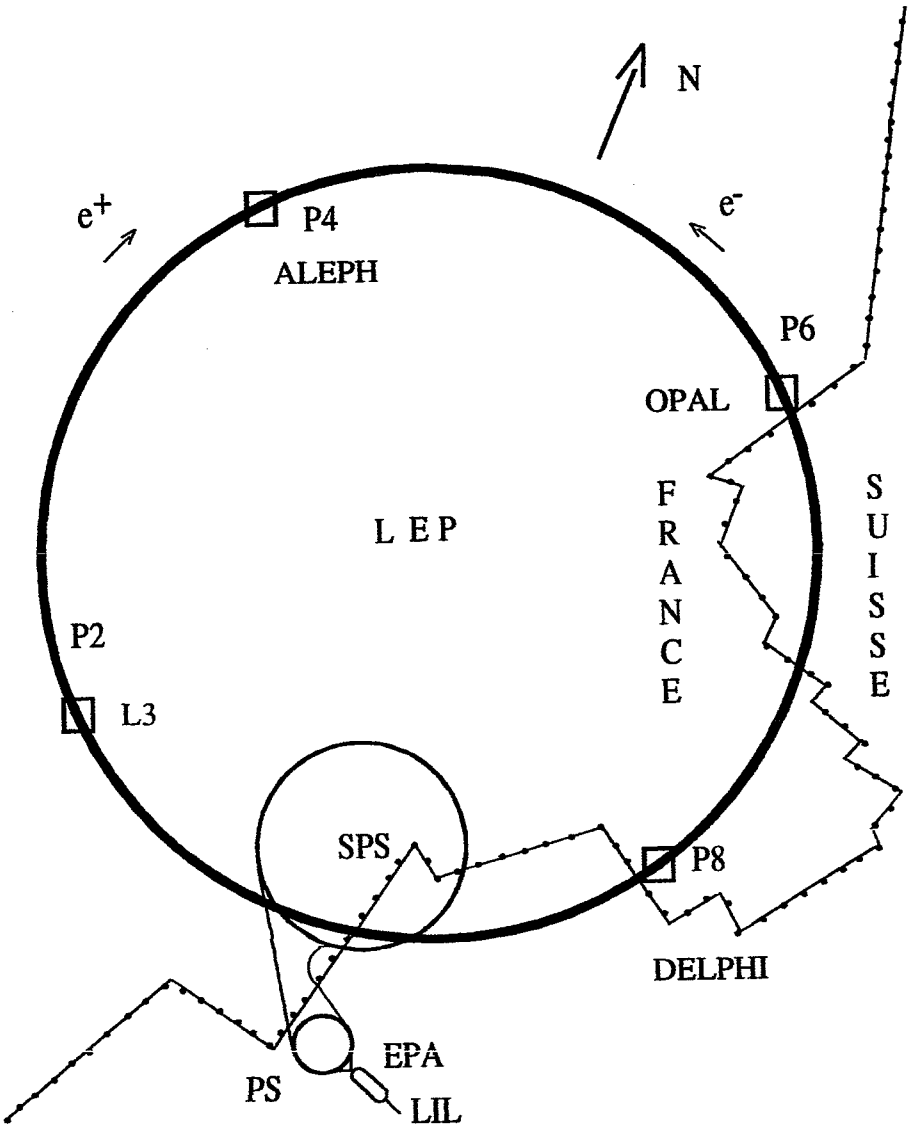

Figure 3.1: Schematic of the LEP ring.

circular path with the aid of 3392 bending magnets (dipoles). The focusing of the beams is realized with the utilization of 1320 focusing–magnets (816 quadrupoles and 504 sextupoles). The magnets take up about 20 km of space in the LEP tunnel. In following a curved trajectory, the beams loose energy in the form of synchrotron radiation. Per single revolution of the tunnel, this energy loss (E_{loss}) is related to the energy (E), mass (m), and radius (R) of the path of the particle according to the following proportionality relationship:

$$E_{loss} \propto \frac{E^4}{m^4 R} \tag{3.1}$$

This implies that the larger the radius of the ring, the smaller the synchrotron radiation loss. Of course, one has to make a trade off between the construction and the operational costs. Besides, geographical limits ultimately dictate the largest size a collider can have. For an energy of 45.6 Gev and radius or orbit of 4300 m (typical LEP values) the synchrotron energy loss for an electron or a positron is 89 MeV/turn.

There are four bunches per beam, giving rise to 8 possible collisions points around the ring. In phase–1 of LEP, fully equipped experimental halls have been constructed at Points 2, 4, 6, and 8 only, where superconducting "low–β" quadrupoles are used for beam focusing. Non–experimental areas of P1, P3, P5, P7 use electrostatic separators to keep the positron and electron beams apart.

The acceleration of the beams and the replenishment of their energy loss due to synchrotron radiation is achieved by arrays of Radio Frequency (**RF**) cavities. These devices are placed on either side of the experimental areas P2 and P6 and are situated in the straight sections of the tunnel. The upgrade of LEP to phase–2 is to be accomplished by replacing the present copper cavities by superconducting niobium cavities together with the installation of additional superconducting RF

cavities at P4 and P8. At present, the total installed RF power is 16 MW with the associated RF frequency, $\nu_{RF} = 352.2$ MHz, and the corresponding wavelength $\lambda_{RF} = 0.851$ m

The reaction rate at any interaction point in the collider is given by:

$$R = \mathcal{L}\sigma \qquad (\mathrm{s}^{-1}) \tag{3.2}$$

where $\mathcal{L}$ ($\mathrm{cm}^{-2}\ \mathrm{s}^{-1}$) is the "luminosity" at the interaction point and σ (cm^2) is the cross–section for the reaction. The luminosity depends on the number of particles per bunch (N_e), number of bunches per beam (n_B), the frequency of revolution for the bunches (f_{orbit}), and the effective area of interaction for the two beams (A_{eff}) [31] via:

$$\mathcal{L} \simeq \frac{f_{orbit}\ n_B\ N_{e+}\ N_{e-}}{A_{eff}} \tag{3.3}$$

where

$$A_{eff} = 4\pi\ \sigma_x\ \sigma_y \tag{3.4}$$

and σ_x, and σ_y are the effective r.m.s. dimensions of the beam profile (assumed Gaussian) in the horizontal and the vertical directions respectively.

The luminosity can be alternatively expressed in terms of the beam–currents. Since $I_{e+,e-} = N_{e+,e-}\ e\ f_{orbit}\ n_B$ (where $e = 1.6 \times 10^{-19}$ is the magnitude of the charge on the electron), the expression for the luminosity becomes:

$$\mathcal{L} \simeq \frac{I_{e+}\ I_{e-}}{e^2\ n_B\ f_{orbit}\ A_{eff}} \tag{3.5}$$

Some typical LEP parameters are given in the table 3.1.

The nominal (design) LEP luminosity for a beam energy of $\mathrm{E}_{beam} = 55$ GeV, and a circulating beam–current of $I_{beam} = 3$ mA is $\mathcal{L} \simeq 1.6 \times 10^{31}\ \mathrm{cm}^{-2}\ \mathrm{s}^{-1}$. Given

Table 3.1: Some Typical LEP performance parameters

LEP–Parameter	Nominal Value
f_{orbit}	1.1×10^4 (Hz)
T_{orbit}	88.9 (μs)
n_B	4
$N_{e^\pm}$	$\simeq 4.25 \times 10^{11}$
σ_x	$\simeq 300$ (μm)
σ_y	$\simeq 20$ (μm)
σ_z	$\simeq 2$ (cm)

$\sigma_{e^+e^-\rightarrow Z^0} \simeq 30\ nb$, the event rate at the Z^0- peak would be:

$$R \simeq (1.6 \times 10^{31})(30 \times 10^{-33}) = 0.48 \tag{3.6}$$

i.e. approximately one event every two seconds.

From a statistics point of view, one is interested in the cumulative number of events collected over the course of the experiment. This is expressed in terms of the "time–integrated luminosity" defined as:

$$\mathcal{L}_{Total} = \int \mathcal{L}(t)\, dt \qquad (\text{cm}^{-2}) \tag{3.7}$$

$$R_{Total} = \mathcal{L}_{Total}\, \sigma \qquad (\text{events}) \tag{3.8}$$

The future prospect for LEP lies in the use of its tunnel for a hadron collider. Indeed, the proposal for a Large Hadron Collider (LHC) with a CM energy of 16 TeV, exploiting the existing LEP tunnel, is under serious consideration by CERN. This pp collider is aimed at exploring the same physics as that of the Superconducting Super Collider (SSC, CM energy of 40 TeV) under construction in Texas, USA. These two colliders indicate the direction which the experimental high energy particle physics community is intending to pursue in the 21^{st} century.

3.2.2 The Injection system

A great reduction in the cost of LEP was achieved by employing the already existing accelerating system to serve as its "injector". It is made up of 3 main components: a linac system, an accumulator system, and a synchrotron (See Figure 3.1).

The LEP Injector Linac (LIL) system consists of an electron–gun and two linear accelerators. It serves the purpose of producing/accelerating positron and electrons pulses. During the positron generation cycle, the electrons produced by the electron–gun are accelerated to 200 MeV in the first linac and are directed onto a converter target. The produced positrons are subsequently accelerated to 660 MeV in the second linac. In the case of the electron cycle, the operation of LIL is very much the same as in the positron cycle except that the converter target is absent and the electron–gun is employed at a much reduced pulse intensity.

The function of the Electron–Positron Accumulator (**EPA**) is to gather a sufficient number of positrons at 660 MeV, prior to injection into the synchrotron system.

Both positron and electrons are fed into the Proton Synchrotron (PS) for additional acceleration to 3.5 GeV. Finally, the particles are passed onto the Super Proton Synchrotron (SPS) for their final phase of acceleration to 22 GeV, at which time they can be injected into LEP.

The act of injecting "fresh" positron and electron beams for the purposes of data acquisition (a "physics run") is referred to as a "fill". A typical LEP fill is as follows. Prior to re–fill, when LEP is undertaking colliding beam physics, the injection system is switched on for the positron filling–mode. When the beam is "dumped", the LEP magnets are reset to 22 GeV. The magnet system is then set up with weaker focusing than normal in the interaction points. This reduces

the sensitivity of the machines during injection and acceleration. When LEP is ready, positrons are fed in for 10 minutes. Next, the injection system feeds in the electrons. This takes about 1 minute for positron/electron switching and 2 minutes for filling. Both beams are then accelerated to the required energy of LEP. Following focusing (for high luminosity) and removal of beam separation, the colliding physics can be resumed.

3.3 The OPAL Detector

OPAL is a multipurpose detector with very good acceptance over nearly 4π of solid angle for the detection of Z^0 decays [32]. It is the most conventional of the four detectors at LEP and was built employing already tested technology to ensure reliable operation at LEP start–up. Its basic design goal has been to construct a detector capable of providing accurate measurements of electromagnetic energy and of charged particles over its full solid angle. It is composed of six main sub-components:

- A 3–component cylindrical central tracking system surrounding the beam pipe which provides information about the momenta and direction of charged particles. It is used for charged particle identification via dE/dx and is employed in primary and secondary vertex reconstruction.

- A large volume solenoidal coil which surrounds the central tracking system and supplies a uniform axial magnetic field.

- An electromagnetic calorimeter made up of 11704 lead glass blocks. It provides identification and energy measurement for electrons and photons.

- Sandwiching limited streamer tubes between the segmented magnet iron return yoke, provides a hadronic sampling calorimeter.

- A muon detection system is provided by a set of drift chambers enveloping the full solid angle of the detector.

- Two forward detectors (one at each end) are used to measure luminosity using Bhabha scattering [1] and identify particles traversing the detector in very forward directions, i.e. very close to the beam line.

Figure 3.2 shows the perspective view of the OPAL detector, where the $z-$axis (which is inclined at 1.4^o to the horizontal direction) represents the direction of the colliding beams, the $x-$axis is horizontal and points to the centre of the LEP ring and finally the $y-$axis is in an upward direction perpendicular to the (x, z) plane. The polar and the azimuthal angles, θ and ϕ, are measured with respect to the positive z and x directions, respectively. The $x-y$ and $x-z$ sections of the OPAL detector are shown in Figure 3.3.

3.3.1 The Beam Pipe

The beam pipe is an evacuated volume to reduce beam$-$gas interactions and to improve beam lifetime [2].

The pipe consists of three sections each about 1150 mm long, with an inner radius of 78 mm, made up of a 0.1 mm aluminum tube unto which a series of overlapping layers of carbon fiber have been epoxied.

The central section of the beam pipe ($|z| < 155$ mm) has 1.3 mm thick carbon fibre lamination which, in addition to the 0.1 mm aluminum liner, corre-

[1] Bhabha scattering is the elastic scattering process $e^+e^- \rightarrow e^+e^-$.
[2] During Physics runs, the LEP ring operates under partial vacuum (10^{-9} Torr).

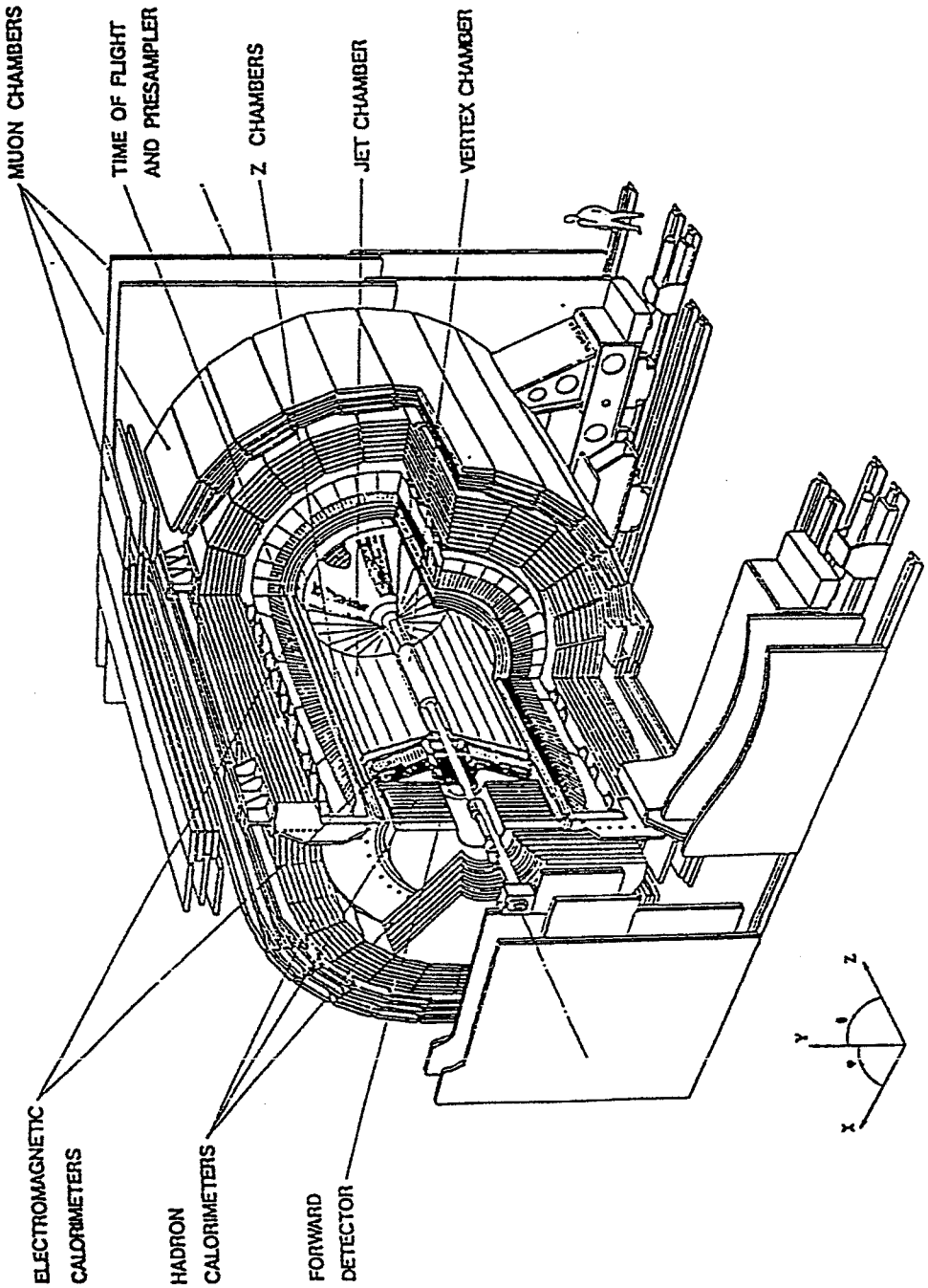

Figure 3.2: A perspective view of the OPAL detector with the associated (x, y, z) coordinate axes.

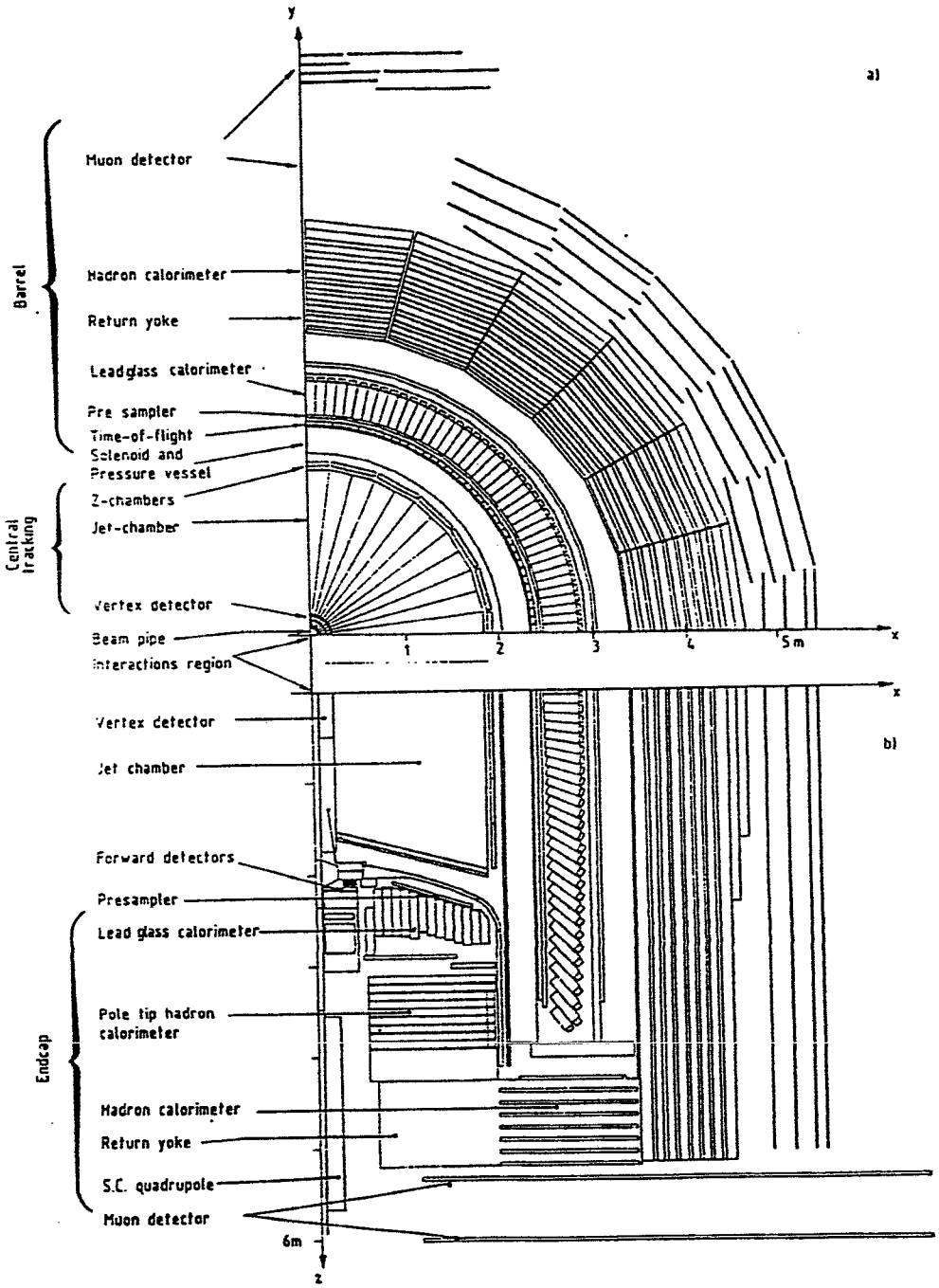

Figure 3.3: The $x-y$ and $x-z$ views of the OPAL detector, showing the subdetectors.

sponds to 0.66% of a radiation length. Its outer edges are tapered to 4mm thick, making it suitable for welding to the other two adjacent outer sections of the beam pipe.

The inner aluminum layer is required to reduce RF losses and local heating. It also furnishes a vacuum tight surface with minimum outgassing.

3.3.2 The Central Tracking Detector

OPAL's central tracking detector operates in a (nominal) axial magnetic field of 0.435 T operating under an internal gas pressure of 4 bars [3]. It is made up of three components:

- A high resolution vertex chamber placed close to the interaction point, which surrounds the beam pipe and affords very good $r - \phi$ and z measurements. It assists in improving charged track reconstruction and helps in accurately determining the interaction point and secondary vertices of short lived particles.

- The main task of tracking is performed by a large drift chamber known as the "Jet chamber." It is positioned radially next to the vertex chamber. It tracks particles over almost the entire solid angle and allows particle detection via sampling energy loss, $\mathrm{d}E/\mathrm{d}x$.

- Z−chambers surround the Jet chamber in the so called "barrel region" of the detector and allow precise z−determination hence resulting in better invariant mass resolution from improved momentum determination.

[3]The OPAL central gas mixture ("OPAL gas") consists of argon/methane/isobutane in the ratio 88.2%/9.8%/2%

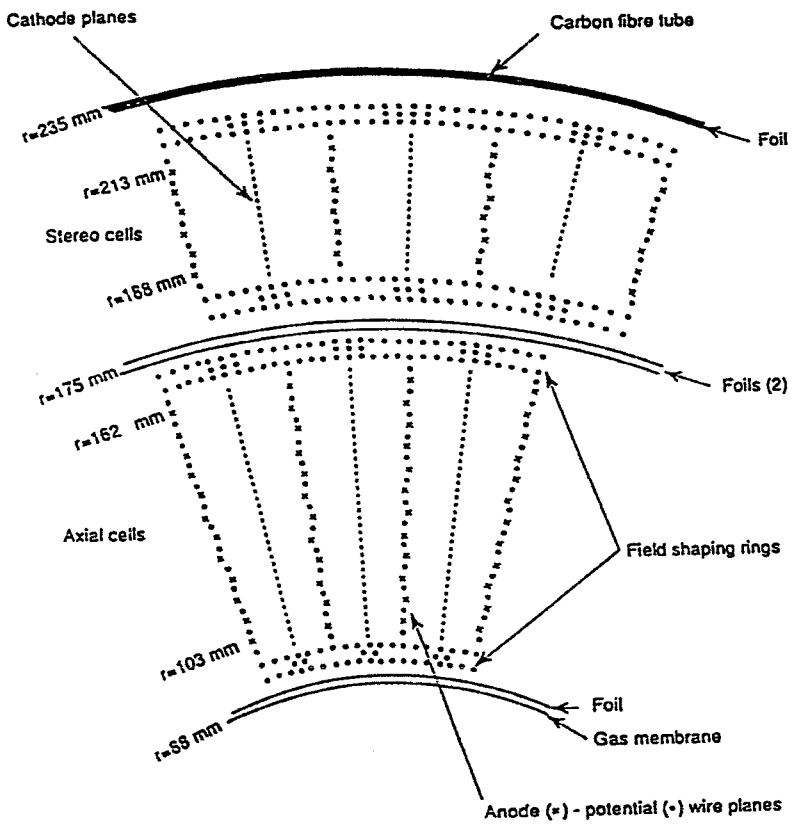

Figure 3.4: Schematic of the OPAL vertex cell geometry.

The analysis presented in this thesis is crucially dependent on the performance of this central tracking part of the OPAL detector.

3.3.2.1 The Vertex Detector

The vertex detector [33] is a cylindrical drift chamber, positioned centrally in the OPAL detector around the beam pipe. It is 1m long and 470 mm in diameter. It consists of 36 inner axial cells and 36 outer small angle stereo cells (stereo angle $\sim 4°$). Each cell is defined in terms of two adjacent cathode planes. The cathode planes are made up of 125 μm diameter copper–beryllium wires with 1 mm radial spacing. Figure 3.4 shows a schematic of the vertex cell geometry. Each axial cell

has 12 anode wires (20 μm diameter gold–plated tungsten–rhenium wires with 5.3 mm radial spacing) located in the chamber between radii of 103 and 162 mm, while each stereo cell has 6 wires (radial spacing 5 mm) located between radii of 188 and 213. The anode wires are placed alternately with potential wires (200 μm diameter gold–plated copper–beryllium), and an anode staggering of $\pm 40\mu$m is used to resolve left-right ambiguity.

The electrostatic condition in the chamber is defined in terms of the drift field and the anode surface field (which determines the gas gain). One achieves the desired fields by an appropriate voltage application to the potential and the cathode wires. The Anode wires are at ground potential and all have uniform gain. Application of a linearly increasing potential with radius to the cathode plane results in a drift field perpendicular to the anode plane which is uniform over most of the drift region. This potential gradient is obtained by a voltage divider resistive chain. Typical operating conditions are a drift voltage of 2.5 kV/cm and an anode surface field of 360 kV/cm. There are 18 separate high voltage (HV) cells for the axial and stereo cells powered by 10 kV Bertran 380N power supplies.

Sense wires are read at both ends and the signals, after amplification, are fed to constant fraction discriminators. By combining the two signals for a given sense wire in a mean timer, one achieves an $r - \phi$ measurement from drift time independent of z with a resolution of 55 μm. Figure 3.5 shows the measured spatial resolution as a function of drift distance in the $r - \phi$ plane for the axial cells. The time difference between the two wire signals allows a z–coordinate measurement with a resolution of $\sim$3 cm. Finally, the chamber possesses a minimum two–particle separation of about 2 mm.

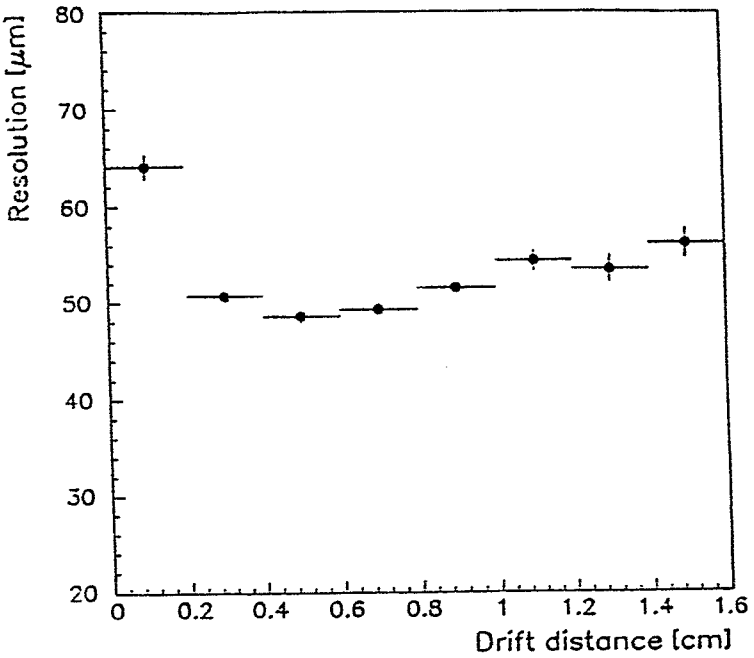

Figure 3.5: $r-\phi$ spatial resolution for the vertex axial cells as a function of drift distance (E_d =2.5 kV/cm, E_s =360 kV/cm).

3.3.2.2 The Jet Chamber

The jet chamber design [34] was motivated by the requirements of both good spatial and double track resolutions to study jet-like events.

It is a cylindrical chamber with a length of about 4 m, having an inner diameter of 0.5 m and an outer diameter of 3.7 m. It surrounds the vertex detector and the beam pipe. The chamber is divided into 24 identical sectors each with 159 anode sense wires alternating with potential wires; these sense wires are drawn parallel to the beam direction and form 24 radial wire planes, positioned between 255 mm and 1835 mm as one moves outwards. Individual wires in each plane are

spaced equally at 10 mm separation in the radial direction with $\pm 100\mu$ m stagger to the left and right of the wire plane in order to resolve left-right ambiguity for track reconstruction. The cathode planes are azimuthally inclined by 7.5° with respect to the adjacent anode planes and each cathode plane is subjected to the same potential gradient varying from -2.5 kV at the inner point to 25 kV at the outer point. The amplified signals from sense wires are recorded by 100 MHz flash analog–to–digital converters (**FADCs**).

The $r-\phi$ spatial positioning is determined by drift time measurement while the $z-$coordinate is determined by charge division. The chamber is operated with a typical drift field of 890 V/cm (gas gain 10^4), with a resulting $r-\phi$ spatial resolution of 135 μm (at a mean drift distance of 7 cm) and an average $z-$resolution of 6 cm. Figure 3.6 shows the variation of the $r-\phi$ resolution with drift distance for the Jet chamber. With 159 measured samples per track, the Jet chamber provides a dE/dx resolution of $\sigma_{(dE/dx)}/(dE/dx)$ =3.5%.

3.3.2.3 The Z Chambers

The Jet chamber is covered by a barrel layer of detectors known as the Z chambers [35], capable of precise z measurement. They cover the polar angle range from 44° to 136°. The detector consists of 24 drift chambers, 4 m long, 50 cm wide and 59 mm thick. Individual chambers are built from 8 bidirectional cells of 50 cm × 50 cm. Each cell has 6 anode wires, placed azimuthally and spaced radially at 4 mm with a stagger of $\pm 250\mu m$ to resolve left right ambiguity.

The Z chambers use the Jet chamber gas and operate with a drift field of 800 V/cm , giving an average z resolution of 200 μm.

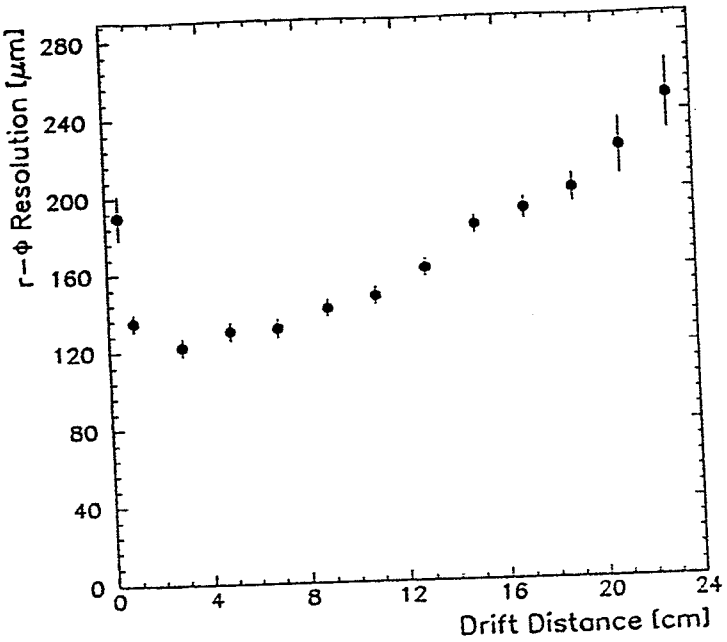

Figure 3.6: $r-\phi$ spatial resolution as a function of drift distance for the Jet chamber.

3.3.2.4 Combined Performance

The combined Central Detector system performance for the analysed data is as follows. The $r-\phi$ momentum resolution in the barrel region of the detector was measured as $(\sigma_{p_T}/p_T) = \sqrt{(0.0018\, p_T)^2 + 0.025^2}$ where p_T is the transverse momentum in the $r-\phi$ plane in GeV/c. Figure 3.6 shows the $1/p$ distribution for dimuon events. The impact parameters measured from these dimuon events are: 45 μm in the $r-\phi$ plane while in the $r-z$ plane it is 2 mm with and 3 cm without the stereo wires of the vertex detector

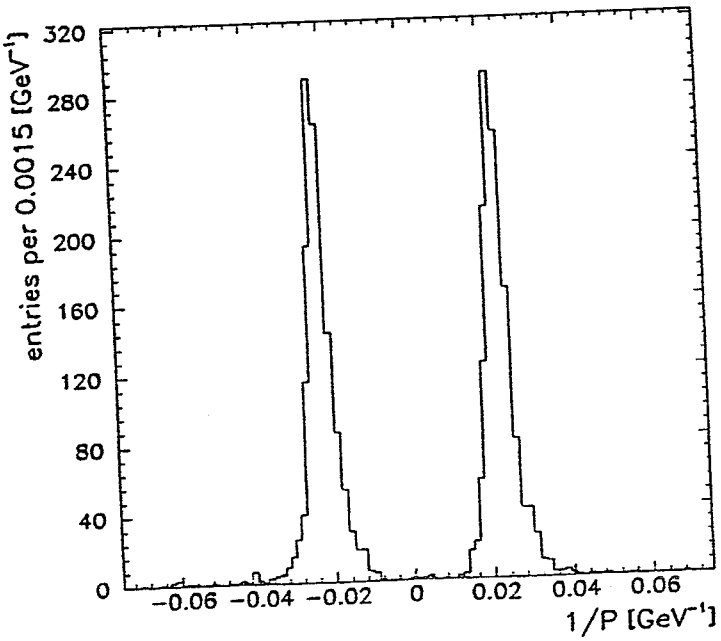

Figure 3.7: Distribution of $1/p$ for dimuon events: $e^+e^- \rightarrow \mu^+\mu^-$.

3.3.3 Magnet

The OPAL magnet has two components: a self-supporting watercooled solenoid coil and a return iron yoke. It has the power consumption of 5 MW and produces an axial magnetic field of 0.435 T which is uniform to within $\pm 0.5\%$ in the Central Detector region.

The return yoke is made of soft steel and is divided into 5 sections: two C's, two poles and one central portion. All are installed on their own respective system of rollers allowing easy assembly during the detector set up.

The annular region between the outside of the coil and the return yoke is

occupied by the barrel electromagnetic calorimeter. The associated photomultiplier tubes which collect the light from the lead glass blocks cannot operate in magnetic fields exceeding a few tens of Gauss. This necessitated the construction of the coil in one *full–section*; an axially segmented coil would have provided a much easier option from a construction point of view, but the magnetic field non-uniformities at the junctions between the different segments would have been unacceptable for the photomultiplier operational mode.

3.3.4 Time of Flight (TOF) System

The TOF system forms a barrel of mean radius 2.360 m, positioned coaxially just outside the magnet aluminum coil and covers the angular range of $|\cos\theta| < 0.82$.

It consists of 160 scintillator counters, each counter being 6.840 m long, 45 mm thick and 90 mm wide.

From $e^+e^- \rightarrow \mu^+\mu^-$ events, a time resolution of 280 ps at the centre and 350 ps at the ends with a z resolution of 5.5 cm have been determined for the operation of this system [4].

3.3.5 Electromagnetic Calorimeter

The electromagnetic calorimeter has been designed to measure the energies and positions of photons, electrons and positrons. It consists of three subsections: a barrel component and two end cap components; each component in turn is constructed from lead glass blocks. The choice of lead glass was based on its good energy resolution, linearity, spatial resolution ($\sim$ 1 cm) and gain stability.

[4]The TOF system has limited charged particle identification capability in the 0.6–2.5 GeV/c momentum range and is also used in triggering.

The barrel component is a cylindrical array of 9440 lead glass blocks of 24.6 radiation lengths placed outside the magnet coil at a radius of 2455 mm. It covers $|\cos\theta| < 0.82$ and the full azimuthal angular range.

Each end cap component is a dome–shaped array of 1132 lead glass blocks with a total depth of at least 20.5 radiation lengths, covering $0.81 < |cos\theta| < 0.98$ and the full azimuthal angular range. It is positioned between the pressure vessel of the central tracking detector and the hadron pole tip.

The calorimeter is supplemented by presamplers (thin multiwire chambers), placed in front of it, to detect electromagnetic showers that have been initiated within the magnet coil and the pressure vessel. In this way, one is able to improve the overall energy resolution by correcting for this energy loss (see figure 3.8).

The electromagnetic calorimeter has a typical energy resolution of $\sigma_E/E = (0.2 + 6.3/\sqrt{E})\%$ in the barrel region and $\sigma_E/E = (2.5 + 16/\sqrt{E})\%$ in the end cap region (where E is measured in GeV).

3.3.6 Hadron Calorimeter

The hadron calorimeter is used to detect and measure the energies of hadrons as they leave the electromagnetic calorimeter. It covers a solid angle of 97% of 4π and is made up of three sections: a barrel section (streamer tube technology), two end cap sections (streamer tube technology) and two pole tip sections (mutliwire chamber technology). The iron return yoke of the magnet is constructed as a sampling calorimeter using limited streamer tube design. The iron core of the hadron calorimeter corresponds to 4 interaction lengths while the material in the electromagnetic calorimeter represents an effective thickness of 2 interaction lengths. Hence the overall electromagnetic and hadron calorimeter is equivalent to

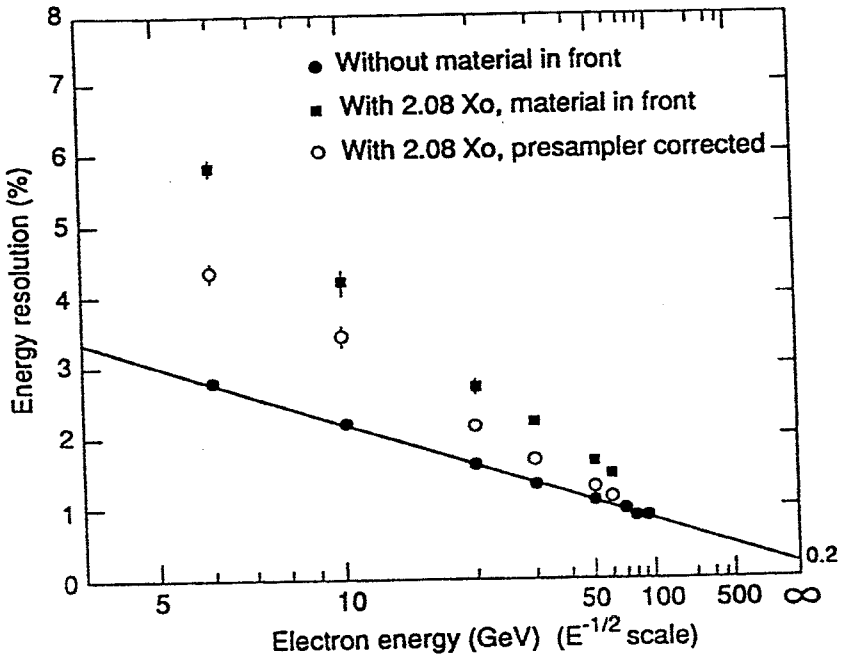

Figure 3.8: Energy resolution for the barrel section of the electromagnetic calorimeter as a function of incident electron energy. In the Figure, the improved resolution from using the presampler is shown.

some 6 interaction lengths.

The barrel section is radially located between 3.39 m and 4.39 m. It consists of 9 layers of active elements alternating with 8 iron slabs 100 mm thick, where the gap between the iron slabs is 2.5 cm.

The donut shaped end caps have 8 layers of chambers alternating with 7 iron slabs. Here once again, the sampling thickness is 100 mm with an increased gap separation of 3.5 cm.

The solid angle for hadron calorimetry is further extended to $0.91 < |\cos\theta| < 0.99$ with the use of the hadron pole tips . In this region an attempt is made

to improve energy resolution by increasing the number of samplings to 10 and reducing the distance between samplings to 86 mm. Over this angular range, the Central Detector has relatively poor momentum resolution.

If $E_{HCAL}(E_{ECAL})$ is the measured energy deposited in the hadron (electromagnetic) calorimeter, assuming the particle to be a hadron (electron), and if R is the e/π ratio of the electromagnetic calorimeter, then the combined energy response of the hadron and the electromagnetic calorimeter to an incident hadronic particle is given by $E_{HCAL}+R\times E_{ECAL}$. R has been determined to be ~3 at 6 GeV and ~2 above 20 GeV. The energy resolution for this combined detector used in determining hadronic energy ranges from $\frac{100\%}{\sqrt{E}}(E \leq 15GeV)$ to $\frac{140\%}{\sqrt{E}}(E = 50GeV)$. Figure 3.9 shows this combined energy response for a 10 GeV beam.

3.3.7 Muon Detector

The last layer in the assembled OPAL detector is the muon detector. It is designed for detecting muons that make it past the hadron calorimeter. The essence of muon identification is the association of an extrapolated central track (allowing for energy loss and coulomb multiple scattering) to a reconstructed muon track segment both in position and angle in two views. Muons above 3 GeV will reach the muon detector and are detected within the 93% solid angle with effectively 100% efficiency. The detector is composed of two main components: a barrel section and two endcap sections.

The barrel section has 4 layers covering an angular range of $|\cos\theta| < 0.68$. It consists of 110 individual drift chambers. The chambers are all 1.2 m wide by 90 mm deep, but have varying lengths of 10.4, 8.4 and 6.0 m. The chambers with shorter lengths were used to fit in between the magnet support legs. The gas is a

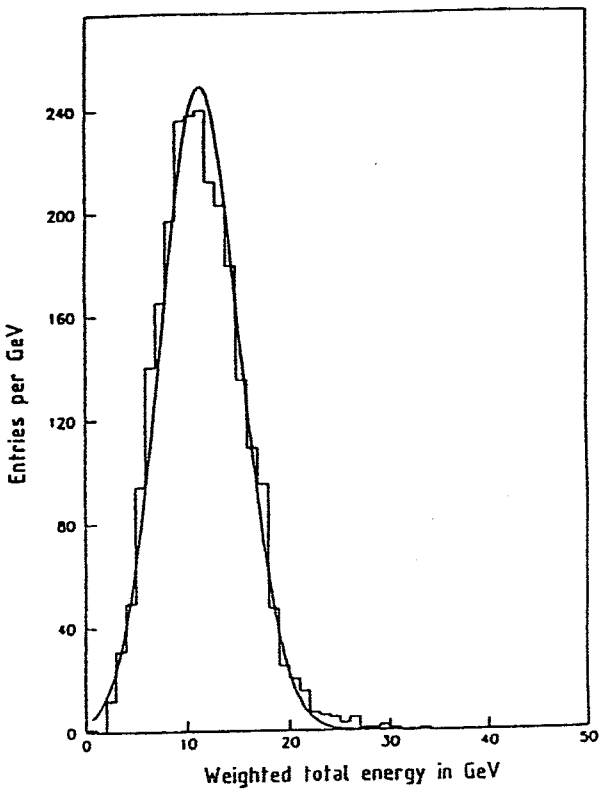

Figure 3.9: Combined energy resolution for ECAL and HCAL for a 10 GeV beam.

10% ethane and 90% argon mixture. The cathode pads are kept at a potential of +4.0 kV while the the anode wires (50 μm in diameter) are set at +1.85 kV relative to these pads resulting in an average drift field of 13.4 V/mm. The maximum drift time in these chambers is 8 μs.

Each end cap section is divided into 8 quadrant chambers (6m×6m) and 4 patch chambers (3m×2.5m), covering an angular range $0.67 < |\cos\theta| < 0.985$, using limited streamer tube technology. The tubes operate with a gas mixture of 25% argon and 75% isobutane with the anode wires (100 μm diameter) at a common voltage of +4.3 kV and cathodes at ground.

3.3.8 Forward Detectors

The forward detectors are used to measure the LEP luminosity by observing small angle Bhabha scattering. The two main components are a lead–scintillator calorimeter and a set of position measuring proportional tubes. The detectors have good acceptance for particles from the interaction region in the angular range of 47 to 120 mrad from the beam and the full 2π azimuthal range.

The forward calorimeter is made up of a presampler ($4X_0$) and a main calorimeter ($20X_0$) and is, in total, composed of 35 layers of lead–scintillator sandwich which are read out via wavelength shifters. The presampler has wave length shifter on the outside while the main calorimeter is read on both the inner and the outer sides. It is subsectioned into 16 azimuthal sections which are contained in two semi–cylindrical parts with a vertical cut allowing its easy mounting around the LEP beam pipe. It has an energy resolution $\sigma_E/E \sim 17\%/\sqrt{E}$ (E measured in GeV), and provides a radial position resolution of ± 2 mm for electron showers using the ratio of the inner to outer signals of the main calorimeter.

Three layers of brass–walled proportional tube chambers occupy the space between the presampler and the main calorimeter. The absolute position of the tubes is surveyed to ± 1 mm. These position measuring tubes are then used to define a precise acceptance region used in absolute normalisation for luminosity determination.

3.4 The Trigger and the Data Acquisition Systems

Beam crossings (BX) at every interaction point at LEP occur every 22.2 μs. For OPAL, situated at one of these interaction points, this translates to a maximum trigger rate of 45 kHz . However, given the nominal luminosity of LEP, actual

e^+e^- annihilation events occur at a rate of no more than 1 Hz. Background events (cosmics, beam gas and beam wall interactions) have substantially higher rates, of the order of 140 Hz [36]. Hence it is necessary to have an efficient trigger system that is able to reduce the number of accepted and recorded events to a few per second (1-5 Hz) by effectively eliminating most of the background events while retaining all of the interesting events.

The physics interest in all final states arising from e^+e^- annihilation events means that one necessarily needs to incorporate a certain degree of flexibility and redundancy in the trigger system in order to make it "intelligent" enough to identify various categories of events.

Finally, in addition to the above requirements, one needs the trigger system to be multilevel. The first level, a fast trigger, reduces most of the background events and minimises dead time. A more sophisticated second level trigger would then be responsible for filtering and possibly recording the selected reduced data set.

The OPAL trigger system [37] has been designed to give good efficiency for various physics reactions of interests such as multihadronic events, charged lepton pairs, while effectively removing background events. The general philosophy behind the design is that most physics reactions generate triggers that are formed from several independent requirements imposed on different subdetector signals. Now, in order to geometrically correlate signals form these various subdetectors, OPAL uses a triggering scheme that is based on $\theta\phi$ segmentation. To this end, the OPAL detector has been divided into 6 polar sectors (θ) and and 24 azimuthal sectors (ϕ), i.e. 144 $\theta\phi$ bins.

Subdetectors deliver two sort of signals, a $\theta\phi$ signal as well as a "stand

alone" signal, where the latter signal is derived form track counting or total energy sums; these analog sums are discriminated in the subdetectors. Both signals are generated based on certain threshold requirements to safeguard against noise. The collection of $\theta\phi$ segmentation for the various subdetectors forms what is known as the $\theta\phi$–matrix. It has 5 layers: track, TOF, electromagnetic calorimeter, hadron calorimeter, and muon trigger.

The trigger/data acquisition system is organised based on MOTOROLA 68k series microprocessors using the VME bus [5].

The OPAL trigger system is known as the "Central Trigger Logic" and is comprised of 4 components:

- The "Single Input Module" (**SIM**), which receives up to 64 direct standard NIM signals form the subdetectors.
- The $\theta\phi$–matrix, consists of 5 modules, one for each detector layer. Here correlation within a given layer and/or between different layers is established.
- The "PAttern Match Module" (**PAM**) has 120 inputs, of this, 64 inputs are from the SIM and 56 inputs from the $\theta\phi$–matrix. It is the logical unit responsible for combining these SIM and $\theta\phi$–matrix signal to produce the final trigger pulse. Based on this trigger decision an event is either accepted or rejected.
- The "General Trigger Unit" (**GTU**). It oversees the general synchronisation and timing of the various subdetectors. Now, each subdetector has a "Local Trigger Unit" (**LTU**) which is connected to the GTU via the trigger bus.

[5]The VME bus is a 32–bit data and 32–bit address asynchronous multi–processor bus introduced in 1982 and is now the IEEE standard.

GTU then dictates the overall trigger decision produced by the PAM to these individual LTU's which in turn take appropriate action.

Figure 3.10 shows the set up of OPAL's central trigger logic. Following each beam crossing, all of the direct and $\theta\phi$ input signals arrive at the central trigger between $1\mu s$ and 14 μs [6]. After formation of internal $\theta\phi$ signal and their combination with the direct signals, PAM combines these signals and decides $\sim 7\mu$s before the next beam crossing whether to reject this event or to further process it. If the event is to be rejected, the GTU issues a reset signal to the LTU's and the detector stands ready. Following reset, the subdetectors clear their modules in order to receive the next gate. However, if the event is to be accepted and further analysed, the GTU broadcasts an interrupt signal which inhibits any further trigger signals. This will continue until all subdetectors have concluded their data readout. On completion of data read out the "busy" signal on the trigger bus is removed allowing further triggers.

The data acquisition system [38] has a multilevel tree structure. For each event, 16 acquisition subsystems (14 subdetectors, trigger and track trigger) supply raw data that is treated by the system. This corresponds to some 150,000 analog signals from the various subdetectors which, after processing, produce on average 100 kbytes of data per multihadronic event.

The Local System Crate (LSC) is the VME system where all data of a subdetector are gathered and from where the subdetector is controlled. It typically contains one or more CPU boards, about 5 Mbyte of memory, the local trigger unit, an ethernet interface, and a VME crate interconnect. Here the acquired sub−event data is formatted for later software processing.

[6] The Jet chamber and muon detector have the longest time lapse due to their long drift times.

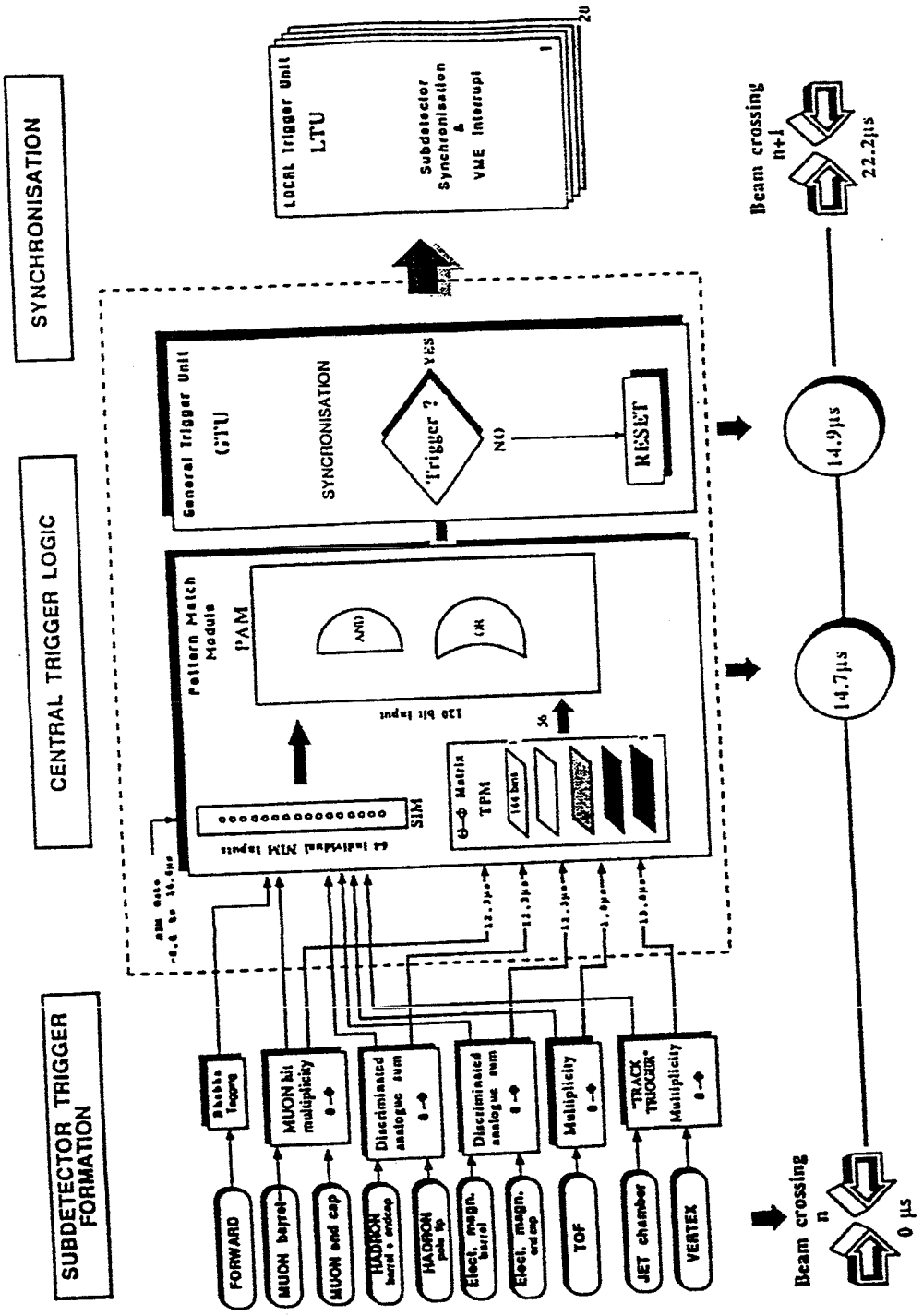

Figure 3.10: The central trigger logic for the OPAL data acquisition system.

The VME system that carries out the task of merging the sub–event data from all the various subdetectors into a single data structure is known as the "event builder". This concatenated data would then be further treated by the "filter" processors.

Filter processors are yet another VME system that perform a fast analysis of each event. At this stage, events get classified into various physics categories and background events are rejected. Subsequent to this, an event identification–bit is set in the 32–bit filter word that associates the event with a particular physics category. The filter program is written in FORTRAN and uses the calibrated calorimeter signals, the jet chamber tracks, the TOF and the muon chamber information.

The data from the filter crate is then transferred via an optical fiber link to the ground level (about 100 m above the underground experimental area) at a maximum rate of 4 Mbyte/s to the so called "top crate" VME system. The top crate is connected to a set of Apollo DN10000 computers equipped with RISC (Reduced Instruction Set Code) processors running under the UNIX operating system. These attached fast processors perform event "reconstruction" using the off–line reconstruction program.

The final step in the data acquisition consists of transferring these processed events via a high–speed parallel link to the main online computer, a VAX 8700, where they are recorded on magnetic tape cartridges. These cartridges are later transferred and stored at the main CERN site for the ensuing physics analysis. The overall data acquisition chain is schematically shown in Figure 3.11.

In order to perform any physics analysis, it is necessary to translate the digitised information from the various subdetectors into meaningful quantities such as

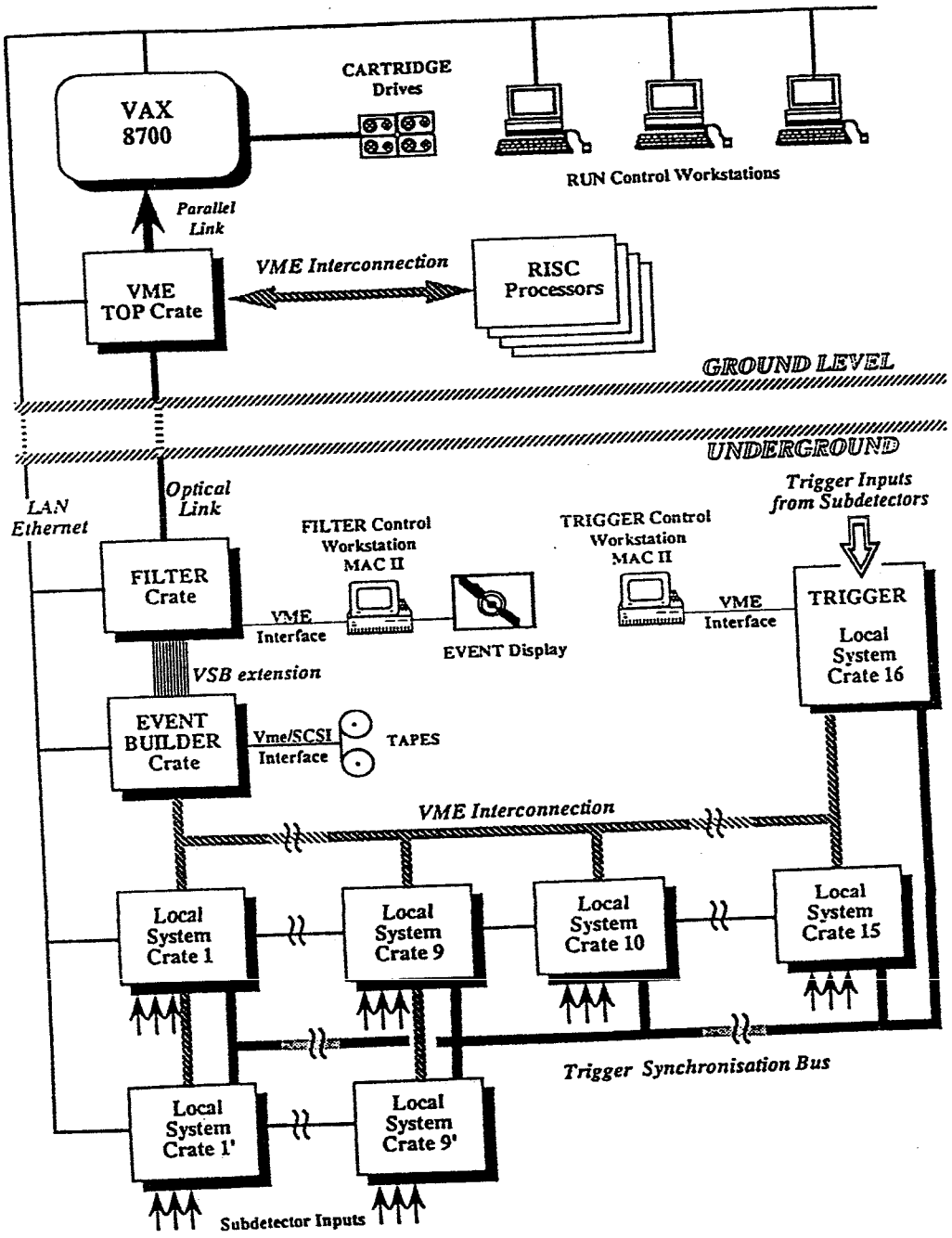

Figure 3.11: The schematic of the data acquisition system for OPAL.

momentum and energy for a given event. This task is carried by an off–line reconstruction program which determines and correlates the energy and momentum from the various subdetectors.

The OPAL reconstruction program is coded in FORTRAN and is known as ROPE (Reconstructor for OPal Events) [7]. ROPE is made up of various software processors that are responsible for interpreting the digitised information for their associated subdetectors. For example, the software processor responsible for handling the digitised information from the vertex detector is known as CV (Central Vertex), that for the jet chamber is referred to as CJ (Central Jet), whereas CZ (Central Zed) handles the information from the Zed chambers. In addition, there are software processors that interrelate the reconstructed information for several different subdetectors. For example, CT (Central Tracking) is responsible for merging the reconstructed subtracks from CV, CJ and CZ into one overall track incorporating the information from all of the 3 central tracking chambers.

The result of the reconstruction is summarised and written into a particular tree–like data structure, known as the Data Summary Tape (DST), where all the relevant information for every given subdetector is recorded in the form of a self–contained data block [8]. In addition there are data blocks that contain information about the global properties of the event including detector and trigger status, charged tracks and secondary vertices. Most physics analyses are then carried out using the DST information only.

[7] Both online and off–line software codes written in FORTRAN use the memory manager ZEBRA [39]

[8] Various calibration files are used in producing the DST information which are not stored as part of the DST.

Chapter 4

The Data Selection

The analysis reported in this chapter is based on a data sample which is comprised of 138,638 multihadronic Z^0 decays collected by the OPAL detector in 1990. The sample corresponds to an integrated luminosity of 6.5 pb^{-1} with an event weighted centre–of–mass energy of 91.314 GeV.

In order to classify, categorise and analyse (multihadronic) events, certain characteristics have to be meaningfully defined. So, before considering the actual selection technique that has been applied to the data, some of these relevant concepts pertaining to the event shape will be discussed.

4.1 Definition of Some Global Shape Parameters

Shape parameters refer to a set of "collective" variables that describe the global shape of an event and quantify its associated properties such as its degree of "jettiness".

One such variable is the *sphericity* (S), which is defined in terms of the *normalised momentum tensor*, M_{kl}:

$$M_{kl} = \frac{\sum_i^N p_{ik} p_{il}}{\sum_i^N p_i^2} \quad k,l = 1,2,3 \tag{4.1}$$

where p_i is the momentum of the i^{th} particle and k, l are space–coordinate indices.[1]

[1]The above definition includes all final particles in the event, although sometimes only charged particles are considered.

Diagonalising this symmetric matrix results in the unit eigenvectors $\mathbf{n_1}$, $\mathbf{n_2}$, $\mathbf{n_3}$ and three eigenvalues Q_1, Q_2, Q_3, ordered according to $0 \leq Q_1 \leq Q_2 \leq Q_3$, with $Q_1 + Q_2 + Q_3 = 1$. Sphericity is then defined as:

$$S = \frac{3}{2}(Q_1 + Q_2) = \frac{3}{2}\frac{min[\sum_j (p_{jT})^2]}{\sum_j (p_j)^2} \tag{4.2}$$

where p_{jT} is the component of momentum perpendicular to the axis $\mathbf{n}$ (the sphericity axis), which has minimised the sum in the numerator.

It is noted that: $0 \leq S \leq 1$, where events with $S \approx 1$ are more or less spherical, while for a pair of collimated jets $S \approx 0$.

Due to its quadratic dependence on particle momenta, S is inherently unstable against collinear decays that could be encountered in fragmentation or QCD radiation. By defining an observable having a linear dependence on particle momenta it is possible to circumvent this sensitivity. One such variable is the principal thrust (T), defined by

$$T = \frac{max[\sum_i |\mathbf{p_i} \cdot \mathbf{n}|]}{\sum_i |\mathbf{p_i}|} \tag{4.3}$$

where the unit vector $\mathbf{n} = \mathbf{n}_{Thrust}$ which maximises the numerator defines the *thrust axis*, and provides one possible candidate for the jet axis. Spherical events have $T \approx 0.5$, while narrow two jet events have $T \approx 1$.

The application of equation 4.3 in the plane perpendicular to $\mathbf{n}_{Thrust}$ determines the Thrust **major** value, T_{major}, with its associated direction, $\mathbf{n}_{Tmajor}$. It provides a measure for three jet events. The *event plane* is then defined by $\mathbf{n}_{Thrust}$, and $\mathbf{n}_{Tmajor}$.

Finally, the direction $\mathbf{n} = \mathbf{n_{Tminor}}$ (which is perpendicular to both $\mathbf{n}_{Thrust}$ and $\mathbf{n}_{Tmajor}$) in conjunction with equation 4.3 yields the Thrust *minor* value, T_{minor}.

4.2 The Multihadron Event Selection

High average visible energy and multiplicity are the two most distinguishing features of a hadronic event. Figure 4.1 shows a typical multihadronic event as observed in OPAL. There are background processes, however, that could reproduce these marked characteristics. So, one needs to identify and discriminate against such background events. The most notable sources are:

- τ–pair ($\tau^+\tau^-$) events with hadronic decays of the τ's; the predominant decays are the 1 prong ((86.13±0.33)%) and the 3 prong ((13.76±0.32)%), while the higher–prong τ decays are less probable (the 5 prong decay has a decay rate of $(1.1\pm0.27)10^{-3}$).

- Beam–gas, beam–wall events. Here, e^+or e^-interact with the residual gas in the beam pipe or the actual material of the beam pipe respectively, sending a shower of particles into the detector.

- Two–photon events where the final pseudo–hadronic final state results from the radiation of two photons (see Figure 4.2).

- cosmic–rays penetrating the detector.

The selection criteria employed to identify a multihadronic event candidate is based on Cluster and Charged Multiplicity information and is known as the CMH selection. The following requirements were imposed:

1. $N_{ctrk} \geq 5$ $\rightarrow$ at least five charged tracks.

2. $N_{clus} \geq 7$ $\rightarrow$ at least seven electromagnetic clusters.

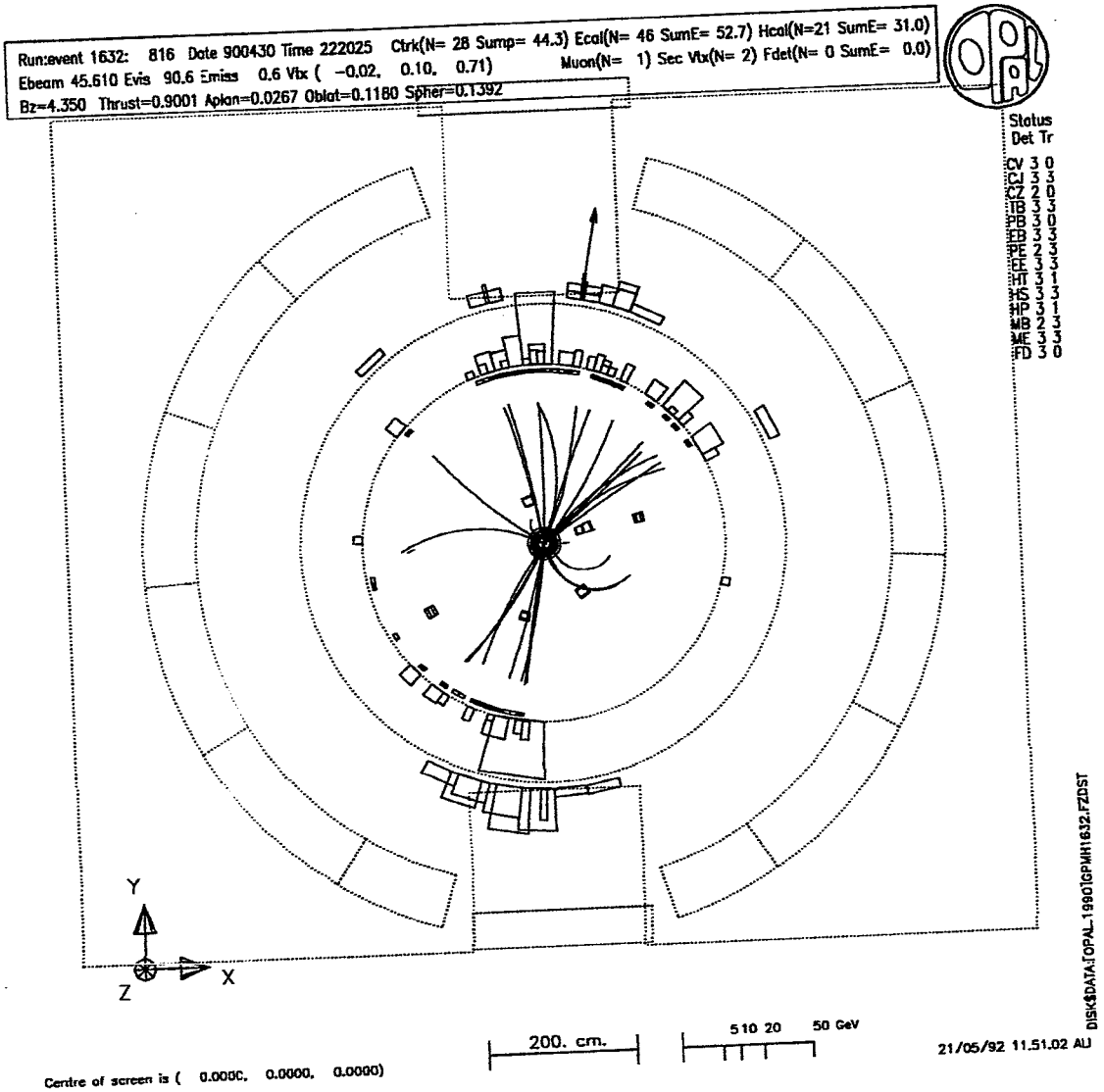

Figure 4.1: A typical multihadron event as observed in OPAL.

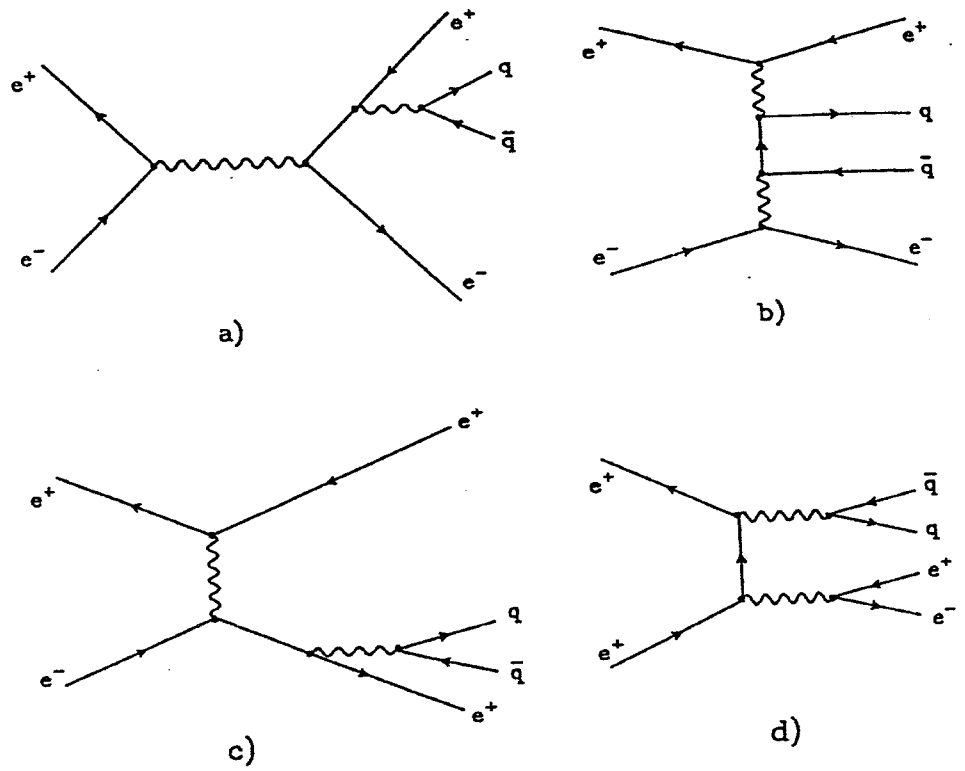

Figure 4.2: Diagrams for two–photon hadron production.

3. $R_{vis} = (\sum_i E^i_{clus}/\sqrt{s}) > 0.1 \rightarrow$ visible energy deposition of no less than 10% of the total centre–of–mass energy.

4. $R_{bal} = |\sum_i E^i_{clus} \cos\theta^i_{clus}| / \sum_i E^i_{clus} < 0.65 \rightarrow$ the energy imbalance along the beam axis, where θ^i_{clus} is the polar angle of the i^{th} cluster, and E^i_{clus} is the energy of the i^{th} cluster.

Only "good" tracks and clusters were utilised in these considerations. Tracks were required to have at least 20 measured space points ("hits")and a minimum momentum component transverse to the beam axis, p_T, of 50 MeV. The "vertex" requirement for these tracks demanded a distance of closest approach to the nom-

inal interaction point of < 2 cm perpendicular to the beam direction, $|d_0|$, and < 40 cm along the beam direction, $|z_0|$. The barrel region clusters were required to have greater than 100 MeV energy, while the endcap clusters contained not less than two adjacent lead glass blocks with a minimum deposited energy of 200 MeV.

The requirements 1. and 2. (see above) were aimed at removing charged lepton pair events. The vertex requirements for the charged tracks effectively discard tracks from beam–gas events and cosmic–rays since these tend to occur far from the collision region. The two–photon and beam–gas events were eliminated by the R_{vis} requirement. The energy imbalance condition, R_{bal}, served to discard beam–gas, beam–wall and the cosmic–rays in the end cap region.

These criteria provide a multihadronic event selection process with a very high degree of purity (the only remaining contaminations arising from two–photon and $\tau^+\tau^-$events which are estimated to be at a level of less than 0.1%). Using the JETSET and HERWIG Monte Carlo (MC) samples, the acceptance for the multihadronic selection procedure has been determined to be (98.37±0.61)% where the uncertainty includes the statistical and the systematic (pertaining to the ambiguities associated with a particular choice of fragmentation model as well as the selection method itself) errors [40].

In this fashion, a data sample consisting of 138638 multihadronic event candidates has been obtained. The collected data spans an energy range of ±3 GeV (at integral intervals of 0, ±1, ±2, ±3 GeV) around the Z^0 mass, and corresponds to an integrated luminosity of 6.5 pb^{-1}. The energy–composition content of the data sample is shown in Figure 4.3. In addition, two Monte Carlo samples, one JETSET and the other HERWIG, containing 164042 and 89926 events respectively, were treated in like manner. The number of multihadronic event candidates

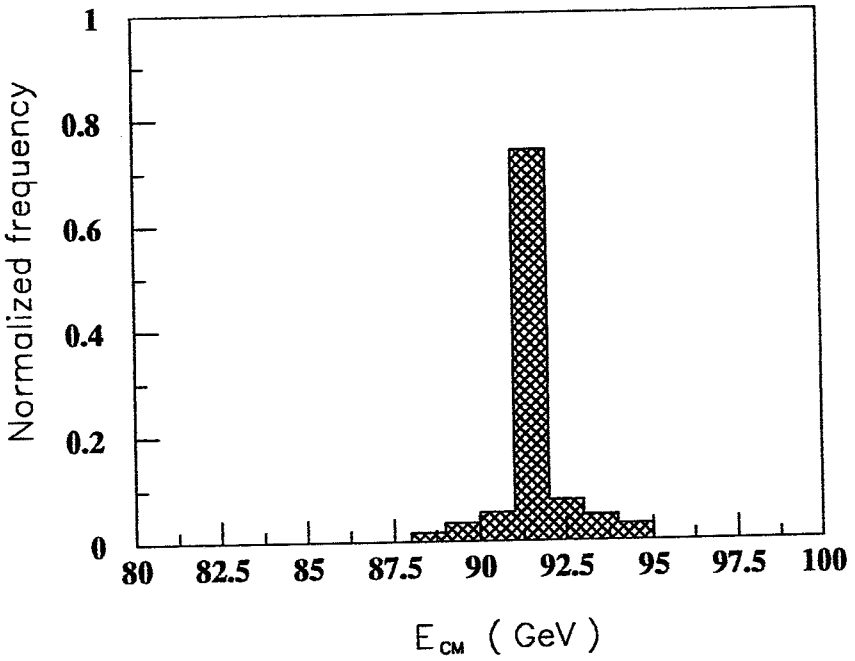

Figure 4.3: The normalised energy—composition distribution for the data sample.

for these two Monte Carlo samples after the selection procedure was 161327 and 88277 respectively, in agreement with the expected 98.4% efficiency of the selection process.

4.3 Global Similarity of the Data and the MC

The MC description of the detector and the physics investigated by the detector is inherently limited and represents only a model. So, having selected the multi-hadronic event candidates, one then needs some form of "compatability" between the data and the MC samples for any ensuing detailed physics analysis. This is necessarily required if one wishes to carry out a meaningful comparison between

the data–extracted experimental results and the theoretical results utilised in the MC simulation.

This overall compatability requirement is demanded in the form of "global similarity" where one has a reliable description of the *collected* data by the *generated* MC on a global scale. It is achieved by applying an additional set of cuts, independently, to both the data and the MC samples, thereby producing "working" samples that exhibit similar global properties. From such a restricted working data sample, one could then confidently extrapolate to the "physics level" (corresponding to the "generator level" in the MC), employing the known detector acceptance for the physics of interest. These cuts will be referred to as the Global Event Shape (GES) selection cuts.

The philosophy behind the GES selection cuts is to choose an appropriate physical region of the detector and of the event phase space that are accurately represented by the MC. Let's consider examples where the MC simulation might be considered an insufficient description of the real physics involved. For instance, tracks that have very low momenta spiral under the applied magnetic field within the central detector and might not be too reliably simulated in the MC. Steep tracks do not generally have as great a measured path length in the Central Detector as do tracks that are well within the barrel region and therefore may not be as accurately measured. Events with polar angle of the thrust vector close to the direction of the beam axis, once again, do not have an entirely reliable MC reproduction. For such extreme forward directions (where a great deal of the energy associated with the event could flow down the beam pipe), the collected experimental information by the detector is clearly limited and is hard to be accounted for in the MC.

To summarise, the effect of the application of the GES cuts is to produce

a set of "well defined" and "well contained" events that can have a reliable MC representation. The GES selection criteria (the final component in the sample selection chain) are listed below:

- Individual charged track quantities:

  1. $p_T \geq 0.15$ GeV, where p_T is the component of momentum perpendicular to the beam axis.
  2. $|\cos\theta_{ctrk}| \leq 0.94$, where θ_{ctrk} is the polar angle of the track.
  3. $|d_0| \leq 5.$ (cm), where d_0 is the distance of closest approach perpendicular to the beam direction.
  4. $|z_0| \leq 99.$ (cm), where z_0 is the distance of closest approach parallel to the beam direction.
  5. $N^h_{CJ} \geq 40$, where N^h_{CJ} is the number of Jet chamber hits associated with the track.
  6. $\chi^2_{ctrk} \leq 999.$, where the χ^2_{ctrk} is associated with the goodness of the charged track reconstruction in the (x, y) plane.

- Global event quantities:

  1. $N_{ctrk} \geq 5$, where N_{ctrk} is the number of charged tracks in the event satisfying all of the preceding single track cuts.
  2. $|\cos\theta_T| \leq 0.9$, where θ_T is the polar angle of the Thrust vector for the event.

Table 4.1 presents the efficiency of the sample selection chain. The overall selection efficiency is of the order of 94%. Figure 4.4 shows the global similarity of the data

Table 4.1: The efficiency of various selection processes on the data and the MC samples.
†→ estimated using the 98.37% selection efficiency .

Selection Process	# DATA Events	# JETSET Events	# HERWIG Events	Selection Efficiency
Generator/Physics Level	(140935) †	164042	89926	100%
CMH selection	138638	161327	88277	~98%
GES selection	131253	154070	84228	~94%

and the MC (JETSET), where the number of entries in the MC histograms have been normalised to that for the data. In Figure 4.5 one sees this compatibility for the sphericity and thrust global shape parameters.

4.4 Summary

The manner in which multihadron events are selected in OPAL has been discussed. The procedure is very efficient ((98.37±0.61)%) and has very high degree of purity (two–photon and $\tau^+\tau^-$ contamination at a level of less than 0.1%).

Following the multihadron cuts, further additional selection cuts are imposed in order to choose multihadron events for which the data and the MC exhibit global similarity.

From a total of 138638 selected multihadron data events, 131253 events survive the latter global event shape selection cuts. This reduced data set then forms the working sample which is used in the K^0_s analysis.

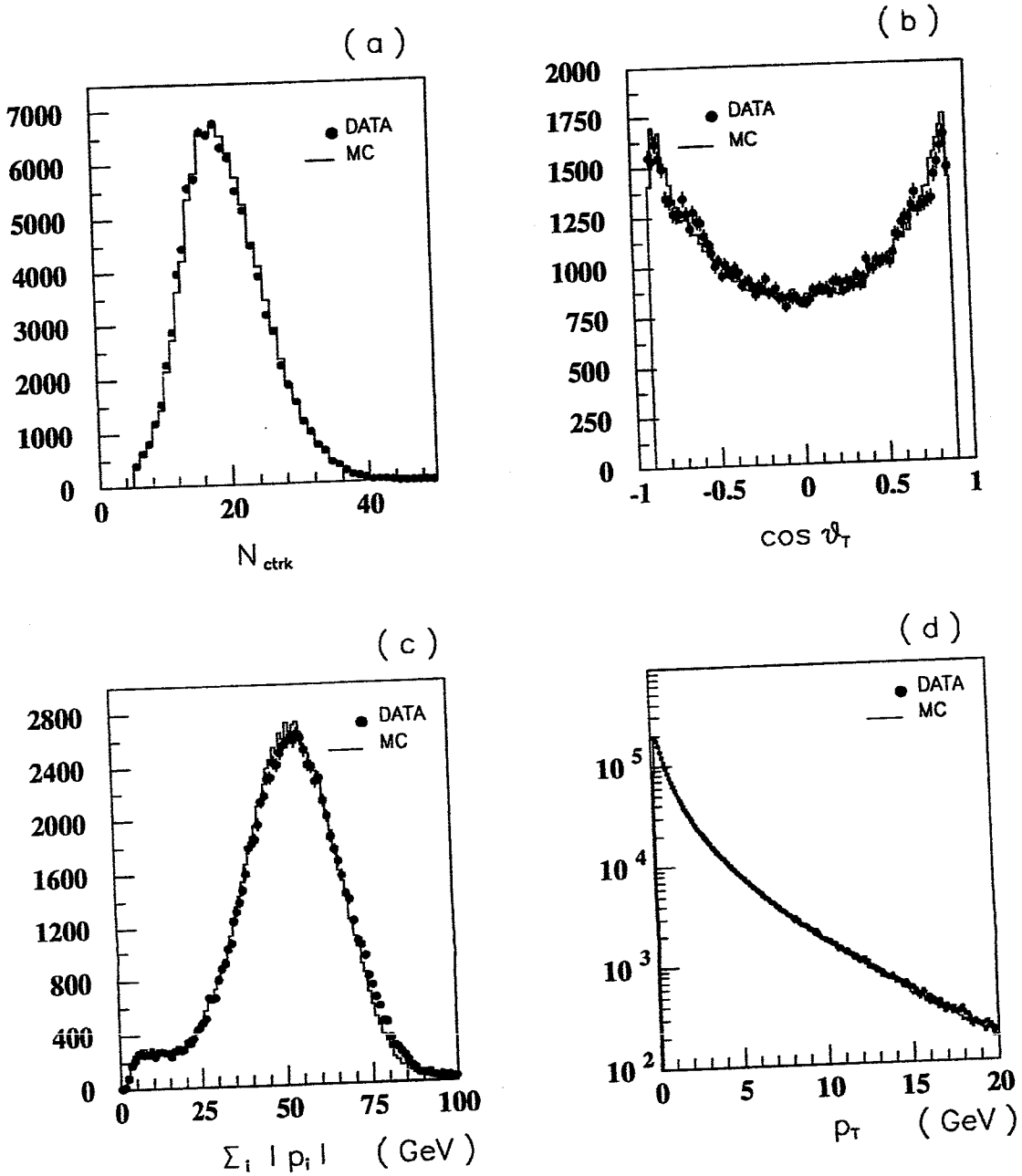

Figure 4.4: Global similarity of the data and the MC (JETSET) is presented in terms of some of the event's shape parameters. (a) Number of charged tracks for the event. (b) Cosine of the polar angle of the thrust vector. (c) Sum of charged momenta. (d) Transverse momentum for the charged tracks.

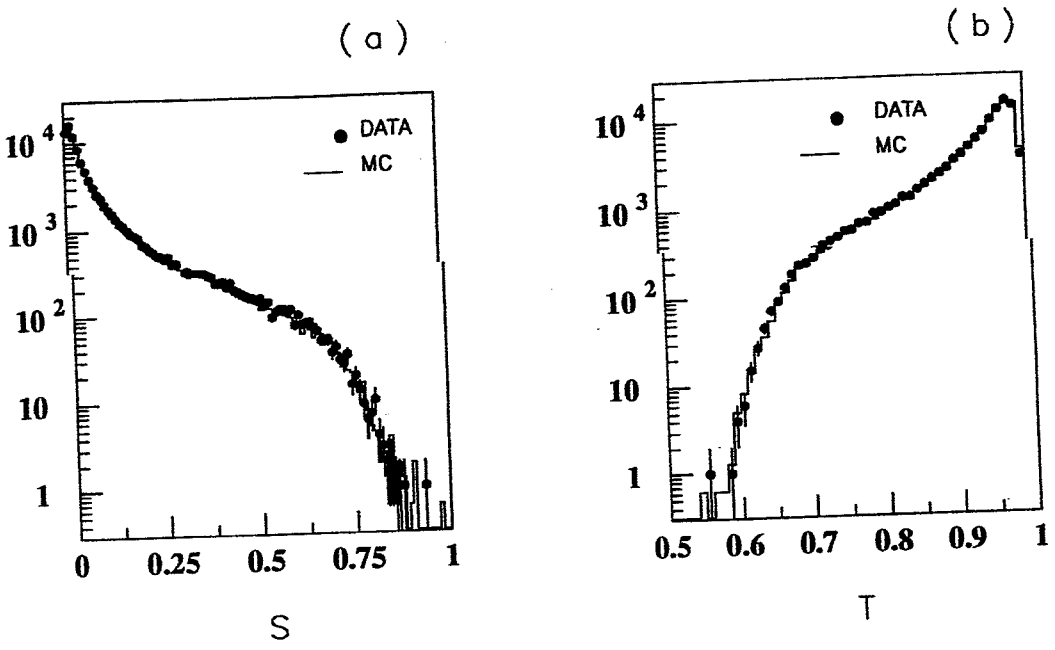

Figure 4.5: (JETSET) as observed for the cases of (a) event sphericity, S, and (b) event thrust, T.

Chapter 5

The Data Analysis

This chapter deals with the manner in which K_s^0 have been reconstructed. The acceptance function for this reconstruction procedure is determined and its associated systematics discussed. The quality of the K_s^0 sample is then checked in terms of fragmentation–independent distributions. The chapter commences with a brief description of how charged tracks are parametrised in the OPAL Central Detector.

5.1 Charged Track Parametrisation and the Associated Momentum Determination in the OPAL Central Detector

Charged particles arising from e^+e^-annihilation within the OPAL detector create helical trajectories in its Central Detector (**CD**) under the influence of an applied axial magnetic field. The description for such paths ("tracks") is done in terms of two *independent* parametrisation: a circle fit in the (x,y)-plane and a straight line fit in the (s,z)-plane (z-axis is taken along the beam axis direction which is slightly inclined to the horizontal direction.) The variable s, is the projected path length along the particle's trajectory in the (x,y)-plane measured from the point of closest approach (p.c.a.) to the origin, (x_0,y_0). Figure 5.1 shows the geometry of a typical track in these two respective planes.

In OPAL, the 5 parameters necessary to describe such a helical motion are chosen to be $(\kappa, \phi_0, d_0, tan\lambda, z_0)$, where:

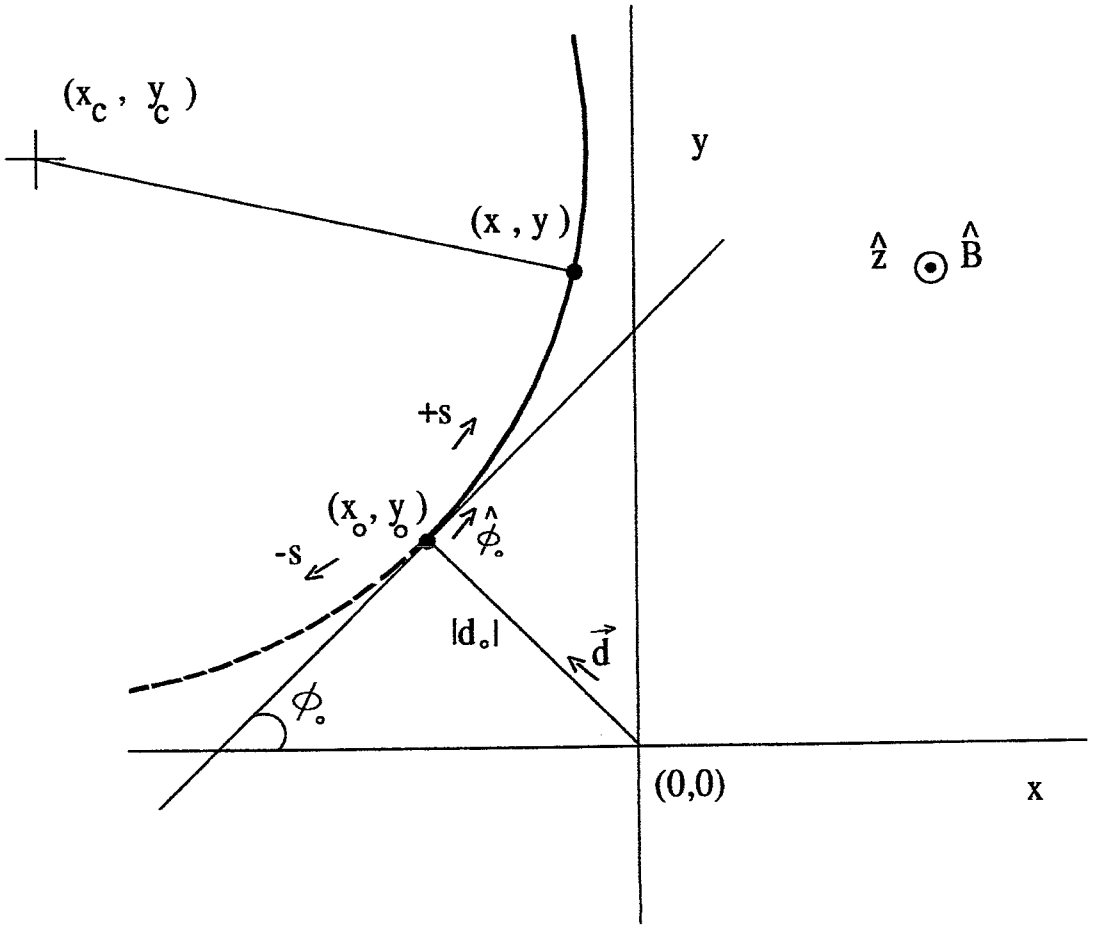

Figure 5.1: Typical track geometry in (x,y)-plane. (x_c, y_c) is the centre of the circular path, (x_0, y_0) is the p.c.a. and (x,y) is a typical point on the track. $\hat{\phi}_0$ is the unit vector along the tangent to the path at the p.c.a., $\vec{d}$ is the vector from origin to the p.c.a. and $\hat{B}$ is the (uniform) axial magnetic field along the +z.

1. $\kappa \rightarrow$ track curvature (cm^{-1}), is related to the radius of the projected circular path in the (x,y)-plane according to:

$$|\kappa| = \frac{1}{2\rho} \tag{5.1}$$

Given an axial magnetic field along the $+z$-axis, a $+ve$ κ corresponds to a $-ve$ charge particle. For such a particle, ϕ (azimuthal angle associated with the track tangent to the path, at the given point of interest), increases as it moves away from its p.c.a.

2. $\phi_0 \rightarrow$ the azimuthal angle (rad.) for the track tangent at the p.c.a. in the (x,y)-plane.

3. $d_0 \rightarrow$ the impact parameter. It is formally defined as:

$$d_0 = \hat{\phi}_0 \times \vec{d} \cdot \hat{z} \tag{5.2}$$

where $\vec{d}$ is the vector from the origin to the p.c.a., $\hat{\phi}_0$ is the unit vector in the direction of the track tangent at the p.c.a. and $\hat{z}$ is the unit vector along the +z-axis.

4. $\tan\lambda = \tan(\frac{\pi}{2} - \theta) = \cot\theta \rightarrow$ where λ is the "dip angle", while θ is the usual polar angle measured from the $+z$-axis.

5. $z_0 \rightarrow$ the $z-$coordinate of the track at the p.c.a.

The (s,z)$-$plane description of the track in terms of the last two parameters is given by:

$$z = z_0 + s \cdot \tan\lambda \tag{5.3}$$

The transverse momentum of a particle with these track parameters is then determined according to:

$$p_T = a\frac{|B|}{|\kappa|} \quad , \quad a = \frac{c}{2} \times 10^{-14} = 1.499 \times 10^{-4} \tag{5.4}$$

where the numerical value of the constant, a, is appropriate to units in which B is measured in kG, κ is measured in cm^{-1}, then p_T is determined in GeV/c; $c = 3.0 \times 10^{+10}$ cm/s is the velocity of light in vacuum.

The other components of the momentum at the p.c.a., are then determined as follows:

$$p_{x_0} = p_T \cdot \cos\phi_0 \tag{5.5}$$

$$p_{y_0} = p_T \cdot \sin\phi_0 \tag{5.6}$$

$$\left.\begin{aligned} p_{z_0} &= p_T \cdot \tan\lambda \\ &= p_T \cdot \cot\theta \end{aligned}\right\} \tag{5.7}$$

The total momentum of the charged particle is then evaluated as:

$$\left.\begin{aligned} p &= \sqrt{p_{x_0}^2 + p_{y_0}^2 + p_{z_0}^2} \\ &= p_T\sqrt{1 + \tan\lambda^2} \end{aligned}\right\} \tag{5.8}$$

5.2 Track Fitting in OPAL

The task of tracking charged particles within OPAL is carried out by 3 central tracking subdetectors. Associated with each of these, there is a corresponding software processor that interprets the measured hits and, after "pattern recognition", reconstructs tracks. The three processors associated with the Central Detector are CV, CJ and CZ. The merging of subtracks from these various processors is done by the CT processor.

A typical, fully reconstructed, track in OPAL can have as many as 183 anode hits (Vertex chamber with 18 anodes, Jet chamber with 159 anodes, and the Zed chamber with 6 anodes) allowing a very accurate determination of the track parameters; the measurement errors being a decreasing function of the number of measured points [41].

However, charged particles travelling through matter experience random deviations due to multiple coulomb scattering from the gas and the solid material within the chambers. So, there are additional uncertainties resulting from multiple scattering that cannot be reduced below a certain level. These scattering errors become significant particularly for low momentum tracks. Since such tracks are produced abundantly, it is important to have a track fitting routine that handles this properly.

OPAL uses a (backward) recursive method of fitting that takes multiple scattering into account following a technique devised by Billoir [42]. The technique performs a fit starting from the outside of the detector moving in, and at each point all of the previously treated points are considered in the fit. Multiple scattering is taken into account between consecutive points by the addition of an average scattering angle contribution to the error matrix.

An alternative but less preferable method of fit is to perform a global instantaneous circle fit with no multiple scattering taken into account. An example of such a technique as employed in the UA1 experiment was devised by Karimaki [43]. Such a technique would certainly be faster than the Billoir method but would have inferior angular and impact parameter resolutions. The interested reader is referred to one such comparison between the Billoir and the Karimaki method that has been made for the case of the OPAL detector [44].

5.3 The K^0 Analysis

5.3.1 The V^0–Finding Procedure

A neutral particle decaying into two charged daughter particles, under the application of a magnetic field, could leave a "signature" resembling a "V"; hence the generic designation of V^0. The charged decays of the K^0_s meson, $K^0_s \to \pi^+\pi^-$, and of the lambda baryon, $\Lambda^0 \to p\pi^-$, are two such examples. Figure 5.2 shows the schematics of a typical V^0 decay topology in the (x,y) plane. In Figure 5.3 an isolated $K^0_s \to \pi^+\pi^-$ candidate is seen, decaying just outside the OPAL vertex detector. The photon conversion, $\gamma \to e^+e^-$, is a special case (zero rest mass particle) for which the two tracks are parallel at the vertex point.

The technique employed in OPAL for finding such V^0 (secondary) vertices is a geometric one [45]. It consists of "looping" over all possible pairs of *distinct* and *oppositely charged* tracks to determine their associated intersection points (if any) in the (x,y) plane: (x_V, y_V) [1].

The track pairs are chosen such that the sum of their absolute impact parameters with respect to the primary vertex is greater than 0.2 cm, i.e. one requires $|d_{01}| + |d_{02}| > 0.2$ cm.[2] In this way, one achieves a substantial reduction in the combinatorial background due to the large track multiplicities emanating from the primary vertex.

Having determined all possible intersection points, the "separation distance"

[1] Charged tracks are described in terms of circles in the (x,y) plane. So, in order to find the cross–over points between any two tracks, one looks for intersection between their two respective circles. For the special case of photon conversion, one determines the point where the tangents to the two tracks are closest together.

[2] An alternative approach would be to place cuts on the individual $|d_{01}|$ and $|d_{02}|$ and not their sum. This leads to a slight change in the shape of the background under the K^0_s peak which is more skewed. The technique employed in this analysis results in a *gentler* variation in the background across the K^0_s mass peak.

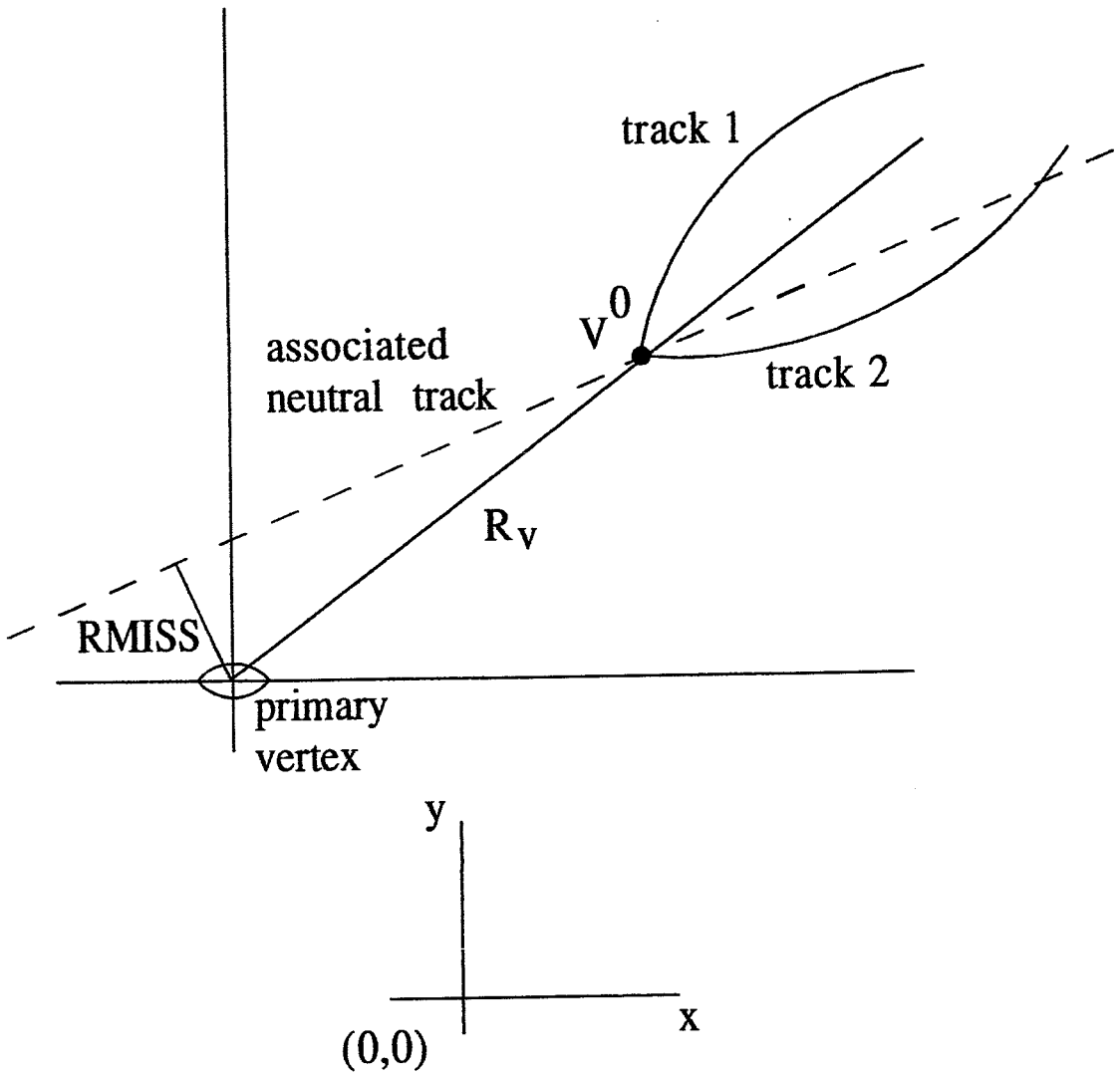

Figure 5.2: Typical V^0—decay topology in the (x,y) plane (not to scale).

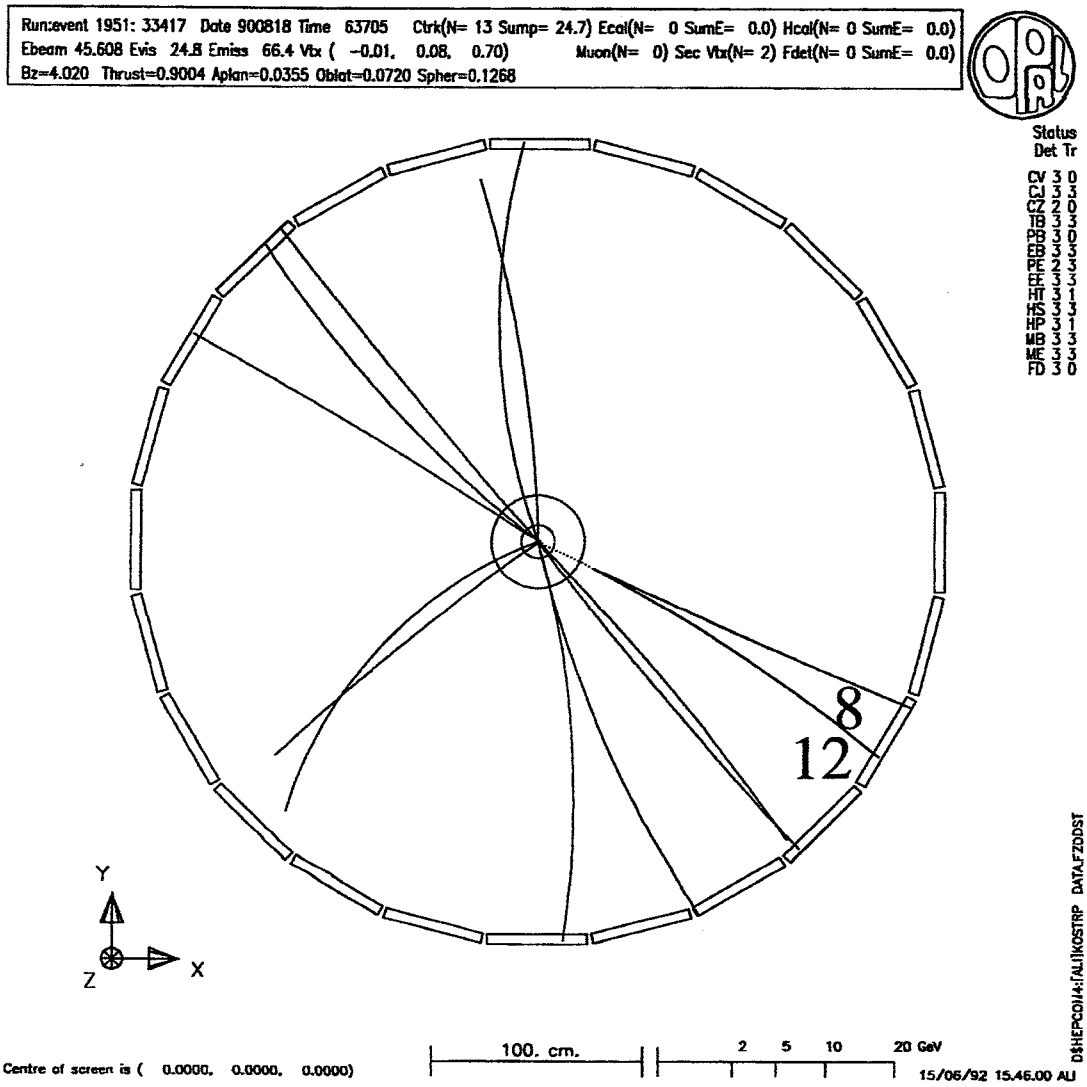

Figure 5.3: An isolated $K^0_s \rightarrow \pi^+\pi^-$ candidate as seen in OPAL Central Detector. The K^0_s candidate is seen decaying just outside the OPAL vertex detector.

(or the "miss distance") in the z−direction, Δz, at these intersection points is calculated and required to be less than 20 cm: $|\Delta z| < 20$ cm.

Furthermore, only the intersection points within the volume of the central detector are considered: $1. < R_V = \sqrt{x_V^2 + y_V^2} < 150$ cm. The neutrality of the reconstructed secondary vertex is further emphasised by allowing no more than 6 cm radial separation between this determined vertex position and the minimum radial position (of the two daughter tracks) of the first upstream hit: $R_V - R_{1min} <$ 6 cm [3].

The candidate−V^0 s remaining, are then subjected to a "pseudo χ^{2}" test defined in terms of Δz and the angle, ϕ_V, which is between the (x,y) momentum of the V^0, $\vec{P_V}$, and its (x,y) position vector with respect to the primary vertex, $\vec{R_V}$:

$$\chi^2_{pseudo} = \left(\frac{\Delta z}{5.}\right)^2 + \left(\frac{\phi_V}{0.015}\right)^2 \tag{5.9}$$

The maximum allowable value for this pseudo−χ^2 is 25: $\chi^2_{pseudo} < 25$. In the case of a track pair for which two possible intersection points exist, the one with the smaller value of χ^2_{pseudo} is chosen.

By performing a constrained (s,z) vertex fit [4] for the tracks making up the V^0 one obtains an improved dip angle determination (i.e. better p_z estimation) and, consequently, an enhanced signal. Figures 5.4 and 5.5 clearly show the improvement in the signal to noise ratio for both the data and the MC samples, respectively.

Finally, the effective mass associated with the V^0 is then determined from the measured (and fitted) momenta at the *intersection point.* For the case of

[3] Where R_{1min} is the minimum radial position of the first hit on either of the two tracks

[4] The manner in which this fit is performed is explained in the next section.

$K_s^0 \rightarrow \pi^+\pi^-$, this reconstructed mass is obtained by assigning pion mass to each of the tracks.

The above mentioned cuts would constitute what will collectively be referred to as the V^0 (or the K_s^0 in the special case of the K^0 meson) selection cuts.

5.3.2 The Constrained (s,z) Vertex Fit

An ideally reconstructed $K_s^0 \rightarrow \pi^+\pi^-$decay would have $\Delta z = 0$. However, due to the finite z–resolution associated with such a reconstruction in OPAL, one generally finds $|\Delta z| > 0$. The fit procedure adopted here is to adjust the $\tan\lambda$ for both daughter tracks such that a common z_v is obtained. [5] The net effect of such a fit is a better p_z determination for the daughter tracks and consequently for the K_s^0. Let $\tan\lambda_1$, $\tan\lambda_2$ be the tan of the dip angles of the daughter tracks before the fit. Then, prior to the vertex fit one has:

$$\left.\begin{aligned} p_{z_1} &= p_{T_1}\tan\lambda_1 \\ p_{z_2} &= p_{T_2}\tan\lambda_2 \end{aligned}\right\} \qquad (5.10)$$

Subsequent to the fit, with the modified dip angles λ_1' and λ_2', the new z–component of momenta are given by:

$$\left.\begin{aligned} p_{z_1}' &= p_{T_1}\tan\lambda_1' \\ p_{z_2}' &= p_{T_2}\tan\lambda_2' \end{aligned}\right\} \qquad (5.11)$$

It is noted that some care needs to be taken in determining the value of s (measured path length in (x,y) plane) utilised in evaluating z_v. One typically expects: $z_1 < z_v < z_2$. However, a wrong choice for the sign of s could result in a z_v far removed from the vertex region.

[5] The algorithm implemented is due to P. Billoir and relies on a χ^2_{sz}–minimisation technique [46].

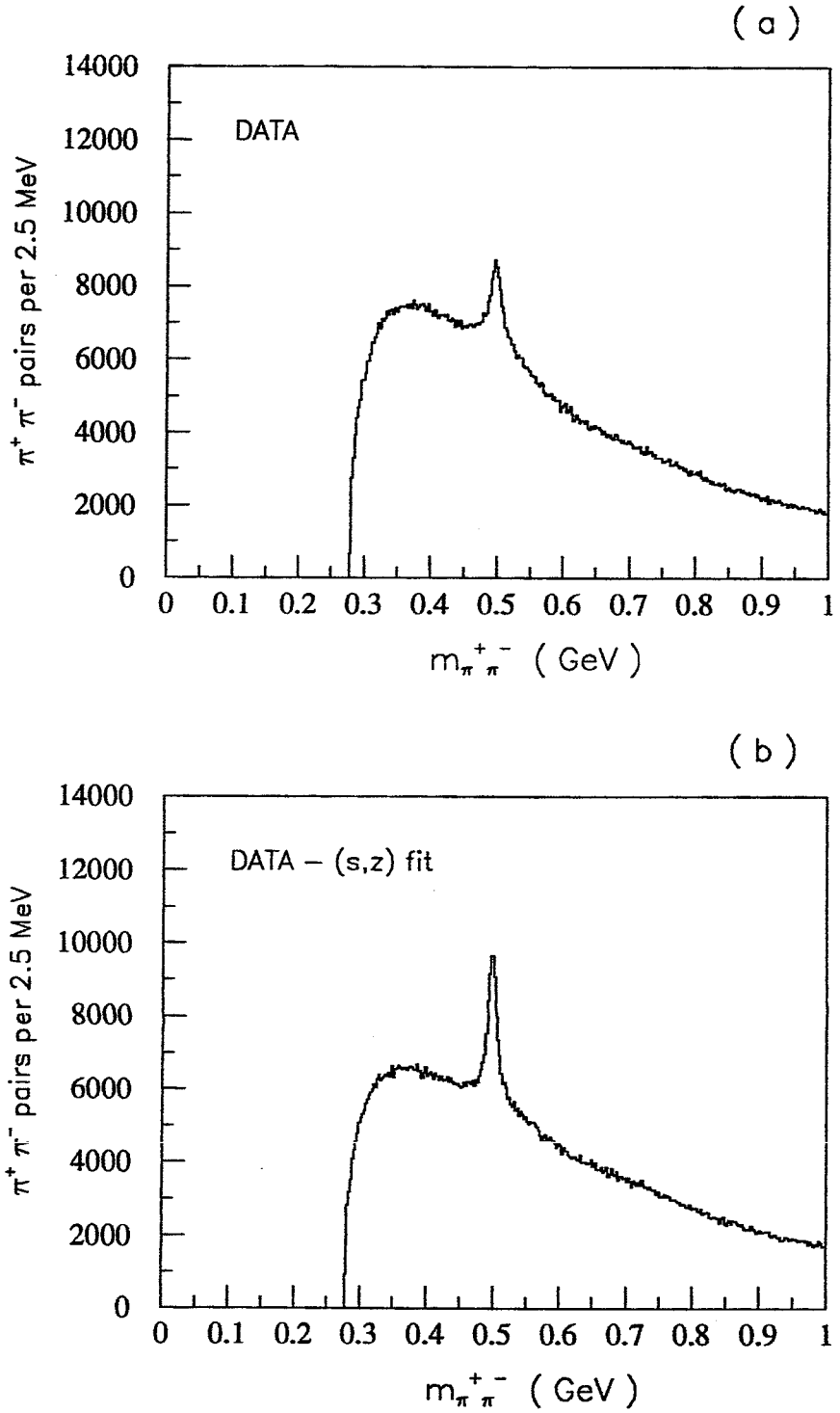

Figure 5.4: The $\pi^+\pi^-$invariant mass distribution (determined with the requirement of $|\Delta z| < 20.$ (cm) at the vertex point) for the data (a) prior to the vertex fit and (b) subsequent to the vertex fit.

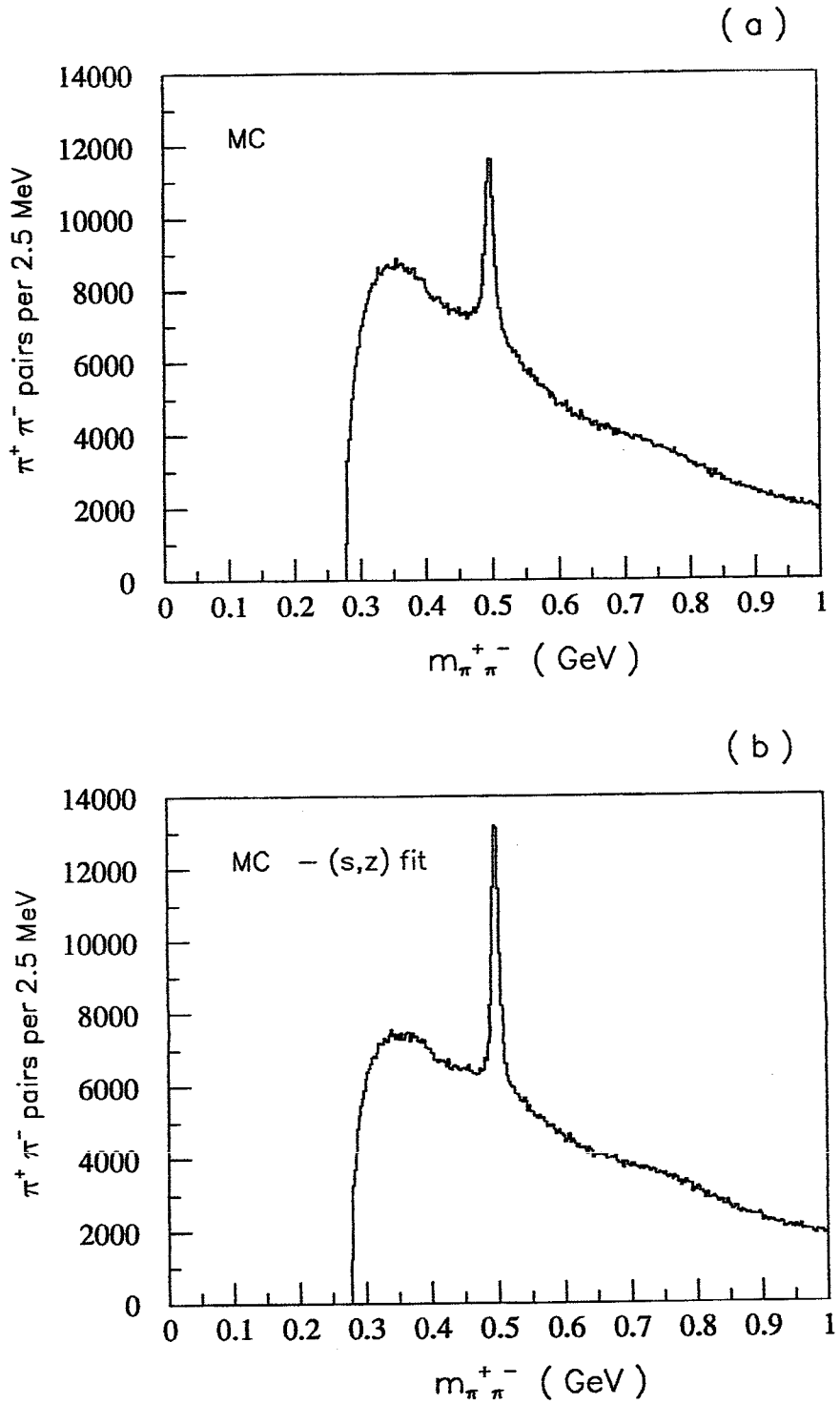

Figure 5.5: The $\pi^+\pi^-$invariant mass distribution (determined with the requirement of $|\Delta z| < 20.$ (cm) at the vertex point) for the MC (normalised to the number of data events) (a) prior to the vertex fit and (b) subsequent to the vertex fit.

5.3.3 Data/MC Observed Rate Difference for $K_s^0 \rightarrow \pi^+\pi^-$

It has been demonstrated that the data and the MC samples possess globally compatible features. However, by comparing Figures 5.4(b) and 5.5(b) one observes a statistically significant difference between the size of the signals for the mass distribution associated with the reconstructed K_s^0 –candidates, i.e. an observed rate difference between the data and the MC (the MC mass distribution has been normalised to the number of entries in the data sample). To understand this systematic, consider the Δz–distributions of the K_s^0 for the data and the MC over the entire solid angle range of the detector. Figure 5.6 (a) indicates a substantial difference between the two Δz–distributions. This is because MC does not simulate the data behaviour completely accurately and CJ has a z systematic that cannot be simulated. This z–associated difficulty is somewhat remedied by restricting oneself to those $K_s^0 \rightarrow \pi^+\pi^-$decays which are expected to have reliable z–measurements, namely, those for which both daughter tracks lie within the barrel region of the Central Detector ($|\cos\theta_{ctrk}| < 0.7$) *and* both have CZ hits. [6] Figure 5.6 (b) presents the Δz–distribution for such a restricted sub–sample. It is evident that the data and the MC distributions are in better agreement than before. Having selected such a sample, one is then faced with the task of determining a meaningful and consistent value of the "matching efficiency" between the Jet and the Zed detectors for the data and the MC. This is then required to account for the different CJ/CZ matching properties exhibited by the data and the MC.

[6] CZ possesses a much better z–resolution than CJ and hence the presence of CZ hits ensures a much better z–determination.

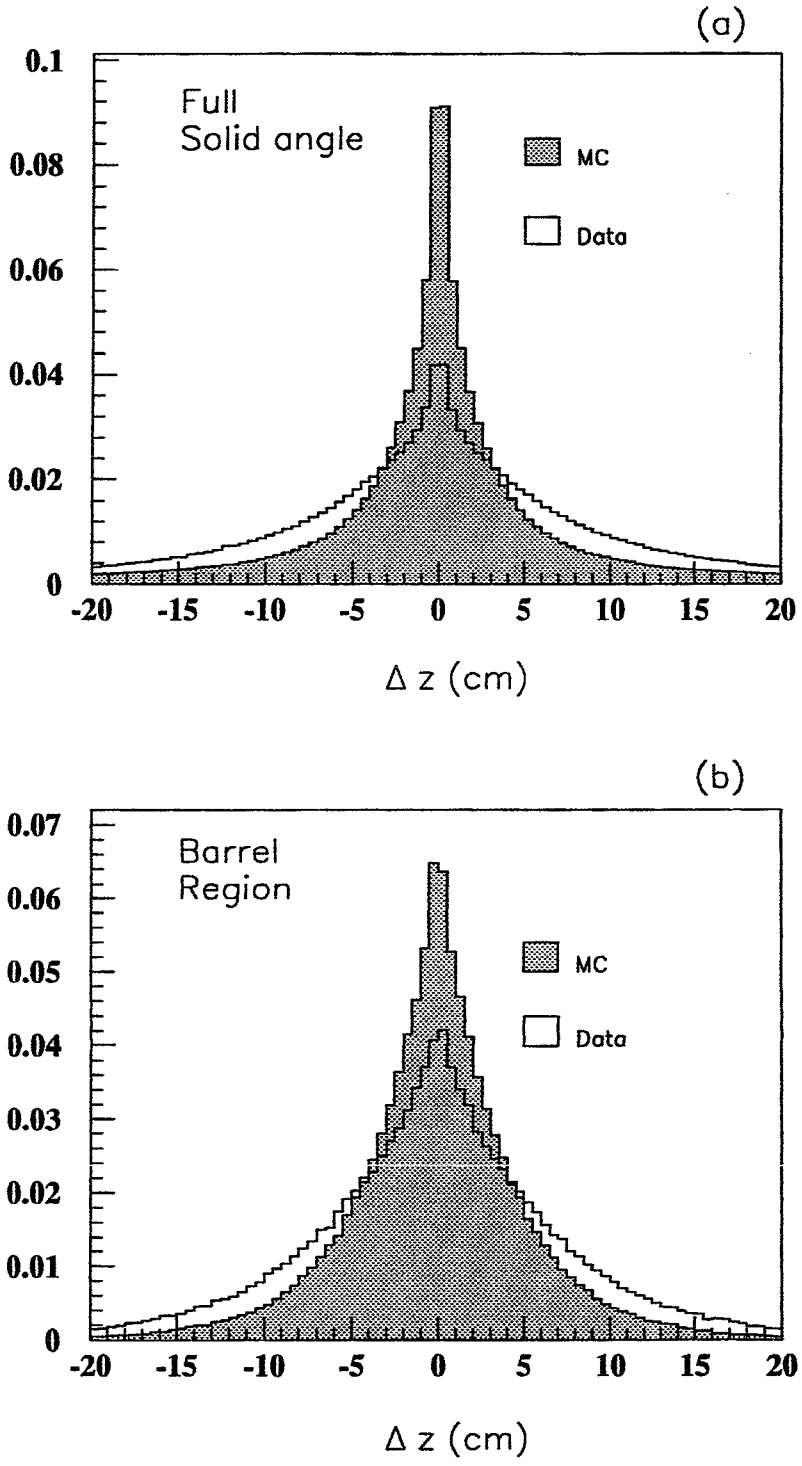

Figure 5.6: Δz distributions for (a) the entire solid angle of the detector and (b) the barrel region of the detector with CZ hits.

5.3.4 CJ/CZ Matching Efficiency Determination

It is now evident that in order to be able to carry out any meaningful rate measurements for K_s^0, it is necessary to employ a restricted K_s^0 sample. Thus, only those $K_s^0 \rightarrow \pi^+\pi^-$with both daughter tracks having CZ hits are necessarily considered. However, due to the poorer angular and momentum resolutions encountered in the data, one then experiences a reduction in the probability of matching the associated track–segments in CJ and CZ for the data as compared to the MC. This is subsequently accounted for by making a correction for the CJ/CZ matching efficiency difference.

The first step in formulating a matching efficiency for the K_s^0 is to define a *single track* CJ/CZ matching efficiency (**STME**), which is determined as a function of the *transverse momentum* of the track, p_T, the cosine of the polar angle of the track, $\cos(\theta)$, and its associated charge, q.[7] Furthermore, only those tracks which satisfy the CMH selection criteria and are contained within the barrel region of the Central Detector are considered. The single track matching efficiency is then defined as the proportion of CJ tracks within a given interval of interest that have at least 3 CZ hits:

$$\epsilon(p_T, |\cos(\theta)|, q) = \frac{N(p_T, |\cos(\theta)|, q, N_{CZ}^h \geq 3)}{N(p_T, |\cos(\theta)|, q)} \tag{5.12}$$

The CJ/CZ matching efficiency for the K_s^0, $\epsilon_{K_s^0}^{CJ/CZ}$, as a function of *total momentum of* K_s^0, $P_{K_s^0}$, is then evaluated (assuming independent single track matching efficiencies) as the product of the single track matching efficiencies of the daughter tracks making up the K_s^0:

[7] At low momenta, +ve and −ve tracks have significantly different STME.

$$\epsilon_{K^0_s}(P_{K^0_s}) = \epsilon_1(p_{T1}, |\cos(\theta_1)|, q_1) \times \epsilon_2(p_{T2}, |\cos(\theta_2)|, q_2) \qquad (5.13)$$

where $q_1 = -q_2$.

The single track matching efficiencies for the $-$ve data and MC tracks are shown in figures 5.7 and 5.8 respectively. The $+$ve data and MC tracks exhibit similar trends.

Having assigned a CJ/CZ matching efficiency as a function of $P_{K^0_s}$, to the candidate K^0_s in this manner then, for any other associated variable x (which could be event–dependent, such as sphericity), one assigns an appropriate CJ/CZ matching efficiency in a similar manner. The momentum–dependent CJ/CZ matching efficiencies for the data and the MC and the associated data correction factor are shown in Figure 5.9 and summarised in Table 5.1[8].

5.3.5 Extraction of Physics Distributions

A typical detector, by the very nature of its construction and its implemented hardware cuts, has a *finite resolution* and a *restricted acceptance*. Furthermore, subsequent analysis may impose its own set of more rigid cuts with further limitations on acceptance. The measurements provided by such a detector (a "detector quantity") results in a "measured distribution" (at the "detector level") of a given "physics quantity" of interest. Such a distribution is "smeared" and does not truly represent the actual "physics distribution."

In order to be able to account for this limited detector behaviour, one relies on MC simulation techniques. Generated MC events are passed through a simulated model of the detector (mimicking the measurement process performed by

[8]The momentum range $P_{K^0} < 0.5$ GeV/c has been made inaccessible to the analysis due to the software cuts on the track momenta.

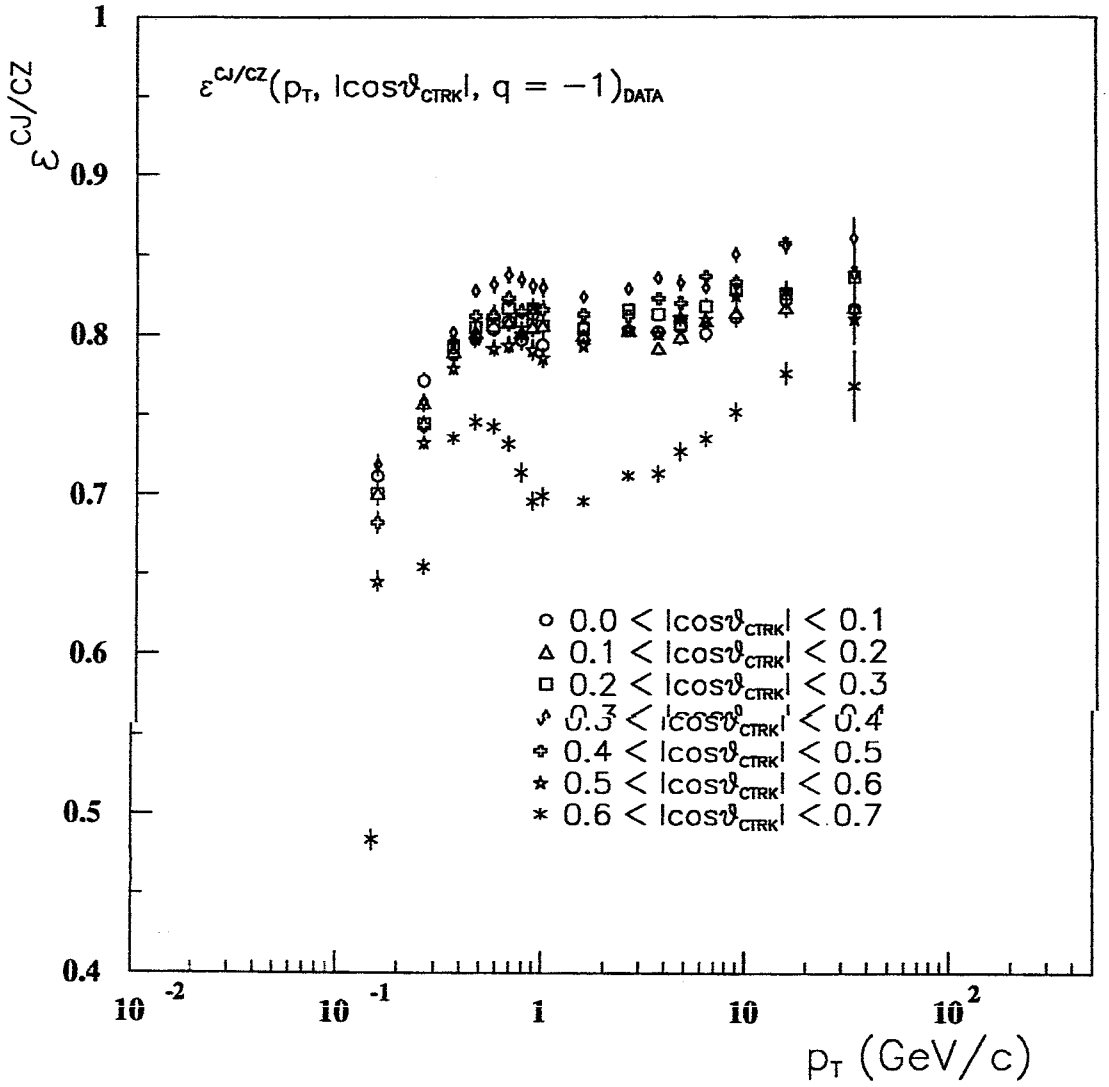

Figure 5.7: CJ/CZ single track matching efficiencies for the **negative** charge tracks as determined from the **data** sample, restricted to the barrel region of the Central Detector: $|cos(\theta_{ctrk})| < 0.7$.

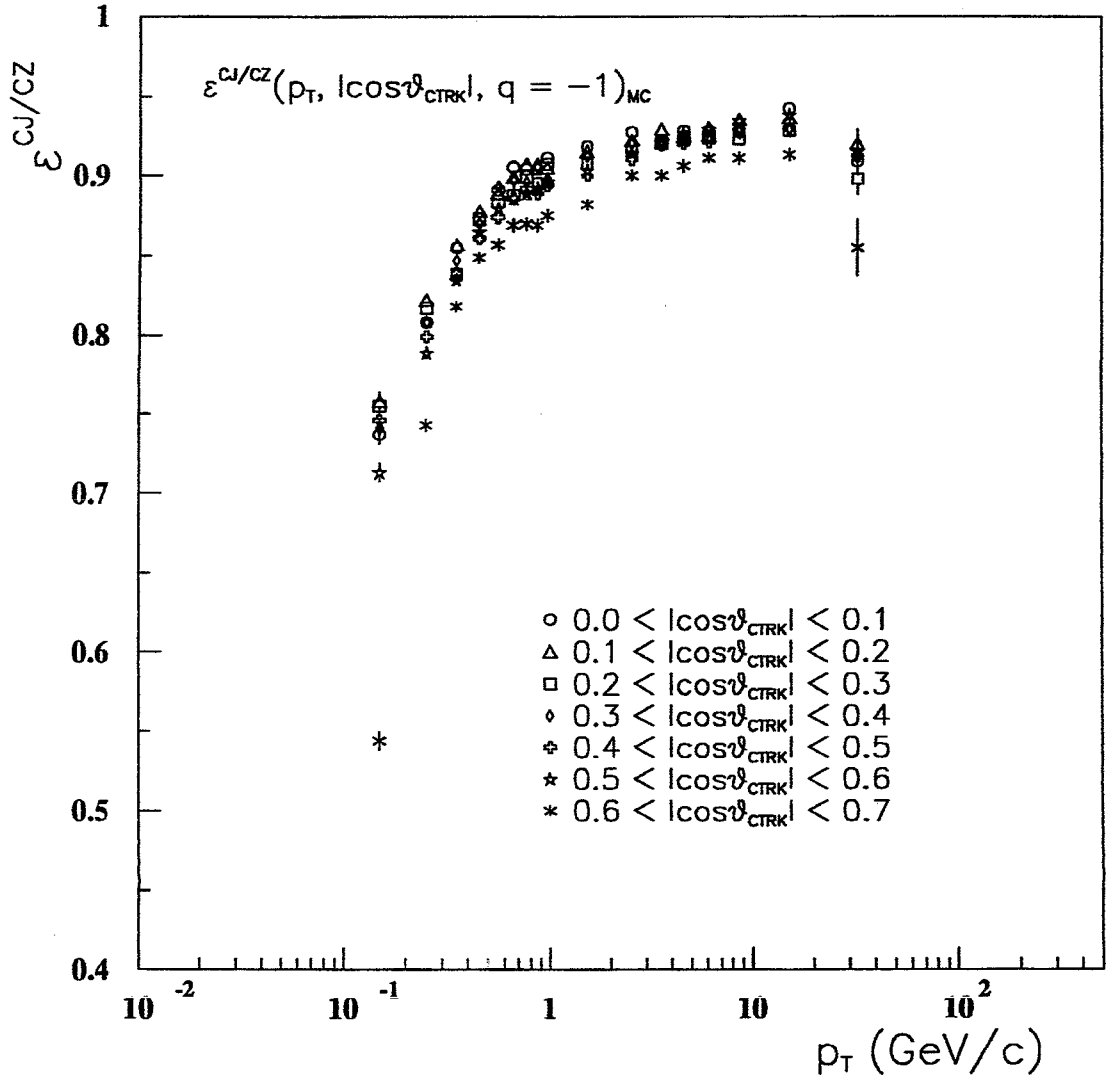

Figure 5.8: CJ/CZ single track matching efficiencies for the **negative** charge tracks as determined from the **MC** sample, restricted to the barrel region of the Central Detector: $|cos(\theta_{ctrk})| < 0.7$.

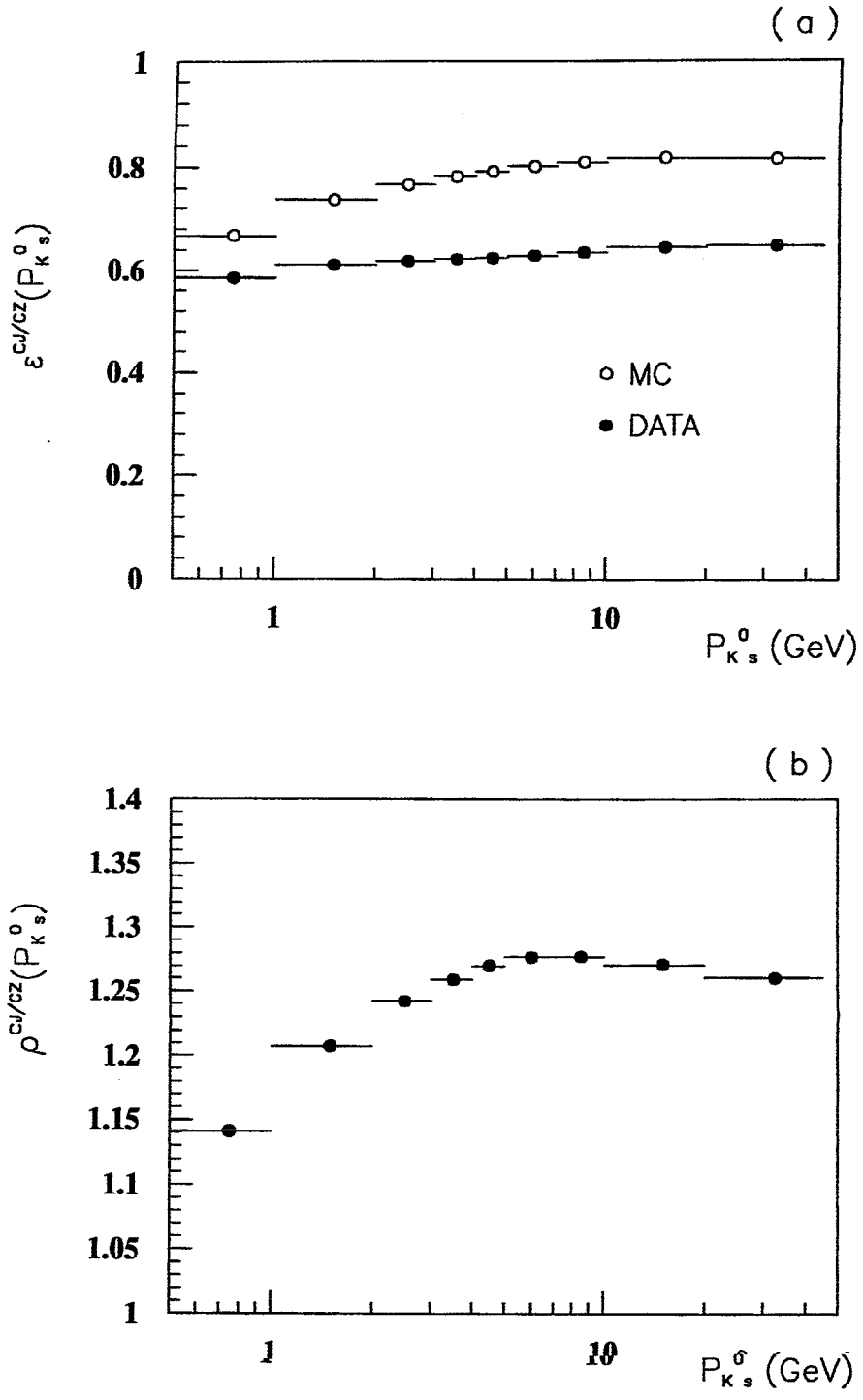

Figure 5.9: CJ/CZ matching efficiencies for the data and the MC and the associated correction factor.(a) Individual momentum–dependent matching efficiencies for the data and the MC. (b) The resulting matching efficiency correction factor.

Table 5.1: $P_{K_s^0}$—dependent K_s^0 matching efficiency correction factor ($\rho_{K_s^0}^{CJ/CZ}$) restricted to the barrel region of the Central Detector.

$P_{K_s^0} - range$ (GeV/c)	$\langle \epsilon_{K_s^0-DATA}^{CJ/CZ} \rangle$	$\langle \epsilon_{K_s^0-MC}^{CJ/CZ} \rangle$	$\langle \rho_{K_s^0}^{CJ/CZ} \rangle = \frac{\langle \epsilon_{K_s^0-MC}^{CJ/CZ} \rangle}{\langle \epsilon_{K_s^0-DATA}^{CJ/CZ} \rangle}$
(0.0, 0.5)	–	–	–
(0.5, 1.0)	0.5854 ± 0.0005	0.6681 ± 0.0006	1.1412 ± 0.0012
(1.0, 2.0)	0.6115 ± 0.0003	0.7384 ± 0.0003	1.2076 ± 0.0007
(2.0, 3.0)	0.6186 ± 0.0003	0.7685 ± 0.0003	1.2423 ± 0.0007
(3.0, 4.0)	0.6233 ± 0.0003	0.7847 ± 0.0003	1.2590 ± 0.0007
(4.0, 5.0)	0.6257 ± 0.0003	0.7945 ± 0.0003	1.2698 ± 0.0008
(5.0, 7.0)	0.6302 ± 0.0003	0.8046 ± 0.0003	1.2767 ± 0.0006
(7.0, 10.)	0.6369 ± 0.0003	0.8133 ± 0.0003	1.2769 ± 0.0006
(10., 20.)	0.6469 ± 0.0003	0.8222 ± 0.0003	1.2710 ± 0.0006
(20., 45.)	0.6514 ± 0.0008	0.8211 ± 0.0007	1.2605 ± 0.0015

the detector) accounting, as best as possible, for the detector's finite geometry and the possible interactions therein. In this manner, one gets a handle on how the detector may treat a given event.

Experimentally measured distributions are then formed by binning the measured ("detector") quantity. This quantity is related to the physics ("detector unfolded") quantity via the matrix equation:

$$\left.\begin{aligned} \underline{U} &= \underline{\underline{C}} \cdot \underline{D} \\ &= \underline{\underline{A}}^{-1} \cdot \underline{D} \end{aligned}\right\} \tag{5.14}$$

where $\underline{D}$ is the measured distribution, $\underline{U}$ is the physics distribution and $\underline{\underline{C}}(=\underline{\underline{A}}^{-1})$ is the correction (inverse acceptance) matrix relating the two. For a bin—by—bin correction, one employs a diagonal matrix relating the measured (detected) and

the physics (generated) quantities. In this manner, for bin i, one has:

$$U_i = A_i^{-1} \cdot D_i \tag{5.15}$$

with

$$A(\langle x_i \rangle) = \frac{n_{det}(\langle x_i \rangle)}{n_{gen}(\langle x_i \rangle)} \tag{5.16}$$

or

$$A_i = \frac{n_{det}^i}{n_{gen}^i} \tag{5.17}$$

where n_{det}^i and n_{gen}^i represent the number of entries in the bin i for the MC's detected and generated distributions respectively. For example in the case of $K_s^0 \rightarrow \pi^+\pi^-$, the momentum–dependent acceptance is defined as:

$$A(\langle p_{K_s^0} \rangle) = \frac{n_{det}(K_s^0 \rightarrow \pi^+\pi^-)}{n_{gen}(K_s^0)} \tag{5.18}$$

In the case of the *data* however, its different CJ/CZ matching efficiency has to be taken into account explicitly. Hence, the corrected (measured) distribution for the data is a modified form of equation 5.15 and is given by:

$$U_i^{(DATA)} = \left(\rho_{K_s^0}^{CJ/CZ} \cdot A^{-1(MC)}\right)_i \cdot D_i^{(DATA)} \tag{5.19}$$

The K_s^0 selection cuts have been optimised so as to produce an improved signal to noise ratio without unduly biasing either the data or the MC samples. In order to be able to realistically apply the acceptance function to the data it is necessary to ensure that these optimised cuts do not preferentially reject more data events than MC events or vice versa. In practice though, no MC models the detector perfectly and hence differences arise in the way these "analysis cuts" treat the data and the MC. This ultimately leads to systematic effects that need to be estimated. The discussion and estimation of such systematic uncertainties

is delayed until later. The K_s^0 optimised selection cuts utilised in this analysis are summarised below:

- $|d_{01}| + |d_{02}| > 0.6$ cm
- maximum allowable separation between the vertex and the 1st hit upstream of the K_s^0 decay vertex was set to 3 cm
- $RMISS = |d_{0V}| = |d_{0K_s^0}| < 0.2$ cm
- $\chi^2_{pseudo} = (\frac{\Delta z}{5.})^2 + (\frac{sin\phi_V}{0.015})^2 < 10.$
- $|\Delta z| < 20.$ cm
- $cos(R_V \cdot p_T) > 0.99975$
- $N^h_{CJ} > 40$
- $1. < R_V < 150.$ cm
- $\chi^2_{sz} < 100.$

The distribution of these selection cuts for the data are shown in Figures 5.11 and 5.12. For each presented distribution, all of the other optimised cuts have been applied. The optimised cuts are seen to discard a relatively small fraction of the total number of reconstructed V^0 events except the $|d_{01}| + |d_{02}|$ cut that rejects a substantial fraction of the candidate V^0, and is a particularly powerful cut for background reduction. Figure 5.10 compares the reconstructed K^0 mass plots resulting from the application of the loose cuts (as disscussed in section 5.3.1) and the optimised cuts, showing the improved signal–to–noise ratio associated with the optimised cuts. In Figure 5.10(b) the shaded regions represent the signal and the

background windows as used in the background subtraction technique (see section 5.3.6.).

Before an acceptance calculation can be performed, one needs to estimate the number of reconstructed entries under the mass peaks, n_{det}. It has been found that a double Gaussian is a more suitable functional form than a single Gaussian for such counting purposes. Figure 5.13 shows the results of a single Gaussian and a double Gaussian fit to the "tagged" MC reconstructed $K_s^0 \rightarrow \pi^+\pi^-$ mass distribution [9]. From Figure 5.13(b) it is seen that a single Gaussian is insufficient to account for the poorly reconstructed K_s^0 that form the tails; a double Gaussian function however, provides a better description of this distribution.

5.3.6 The Double Gaussian Functional Form

The most general double Gaussian function has the form:

$$f = \left(N_1 \frac{1}{\sqrt{2\pi}\sigma_1} e^{-0.5(\frac{m-\mu_1}{\sigma_1})^2} + N_2 \frac{1}{\sqrt{2\pi}\sigma_2} e^{-0.5(\frac{m-\mu_2}{\sigma_2})^2} \right) \tag{5.20}$$

For the purposes of number estimation from the differential mass peaks, certain constraints have to be imposed necessarily on the above general functional form. If the above function is to provide one with a total number of reconstructed $K_s^0 \rightarrow \pi^+\pi^-$, then one must have $N_1 + N_2 = N_{tot}$. In addition, the two Gaussians are required to have the same mean, $\mu_1 = \mu_2 = \mu$ [10].

With these two constraints, the modified double Gaussian function takes the form:

$$f = N_{tot} \left(\frac{N_1}{N_{tot}} \frac{1}{\sqrt{2\pi}\sigma_1} e^{-0.5(\frac{m-\mu}{\sigma_1})^2} + (1 - \frac{N_1}{N_{tot}}) \frac{1}{\sqrt{2\pi}\sigma_2} e^{-0.5(\frac{m-\mu}{\sigma_2})^2} \right) \tag{5.21}$$

[9] Using tagged reconstructed $K_s^0 \rightarrow \pi^+\pi^-$ candidates eliminates any possible systematics associated with background effects.

[10] This is required in order to clearly distinguish the second broader Gaussian (poorly reconstructed K_s^0 from the background over which it is fitted.

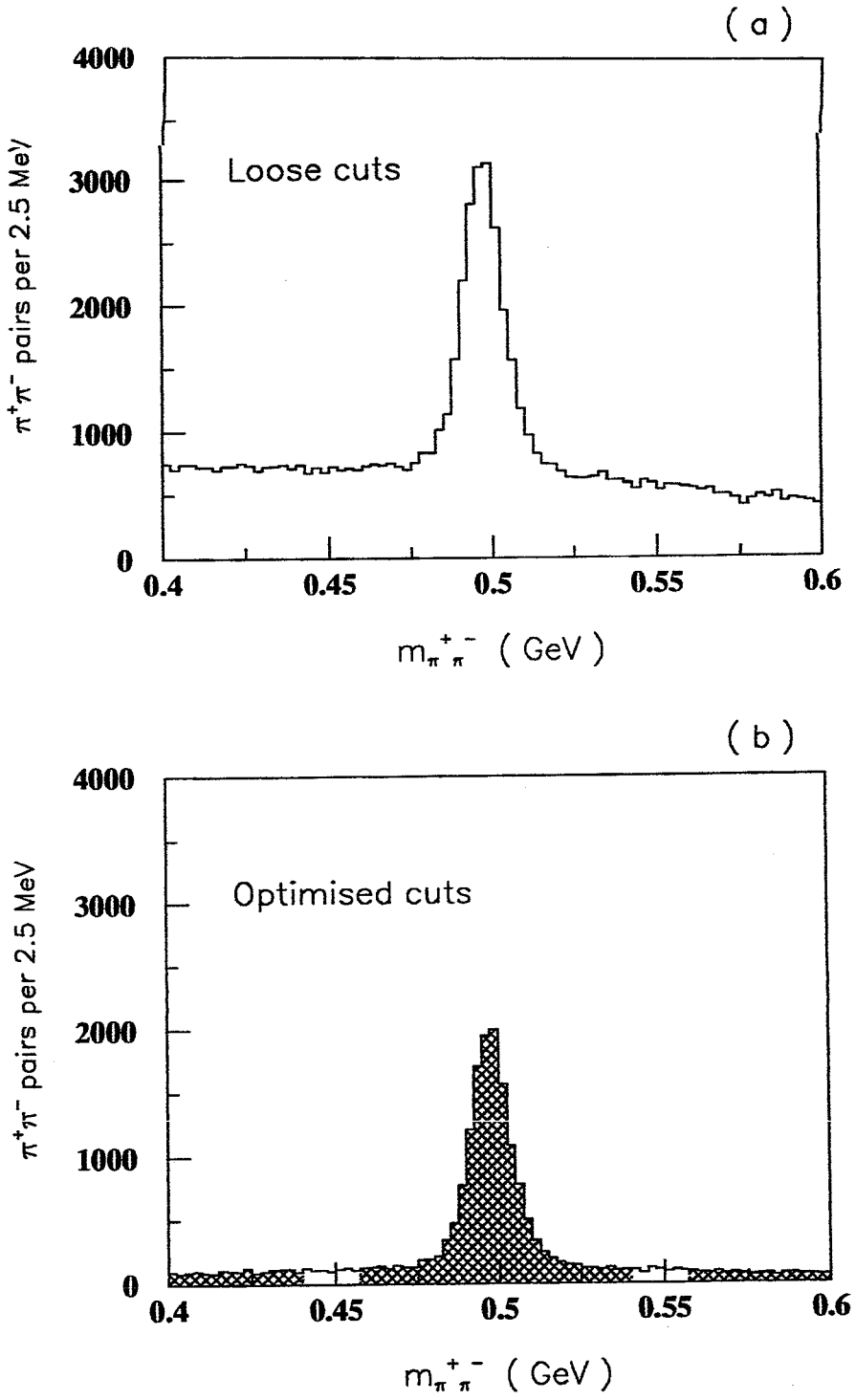

Figure 5.10: Comparison of the reconstructed mass for K^0 candidates for (a) the loose cuts (see section 5.3.1) and (b) the optimised cuts. The shaded regions in (b) represent the signal and the background windows as used in the background subtraction technique (see section 5.3.6).

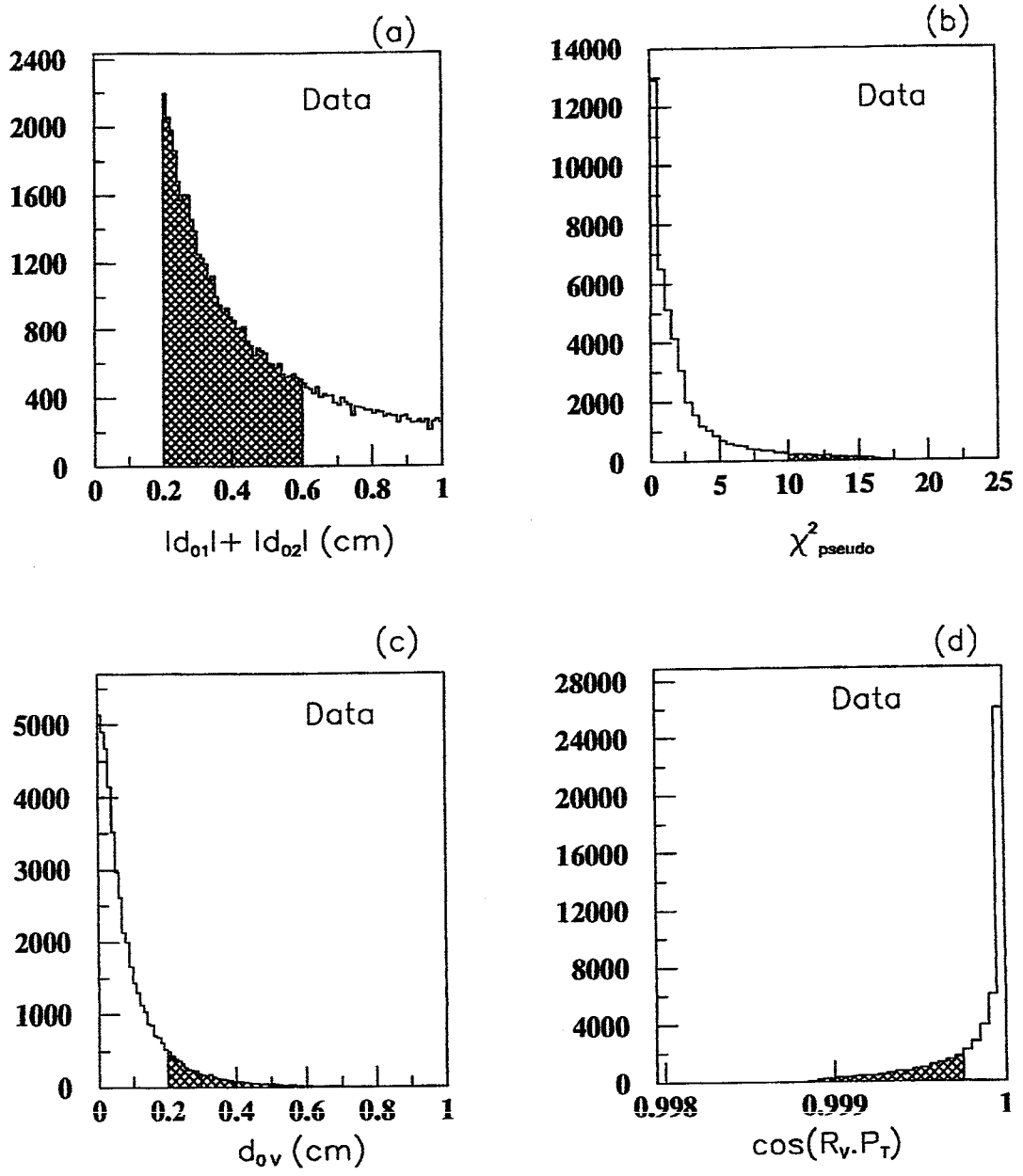

Figure 5.11: Optimised cut distributions for the data (a) $|d_{01}| + |d_{02}|$, (b) χ^2_{pseudo}, (c)d_{0V}, and (d)cos$(R_V \cdot p_T)$. For each distribution, all of the other cuts have been applied. The shaded areas represent the region of rejection for the cut.

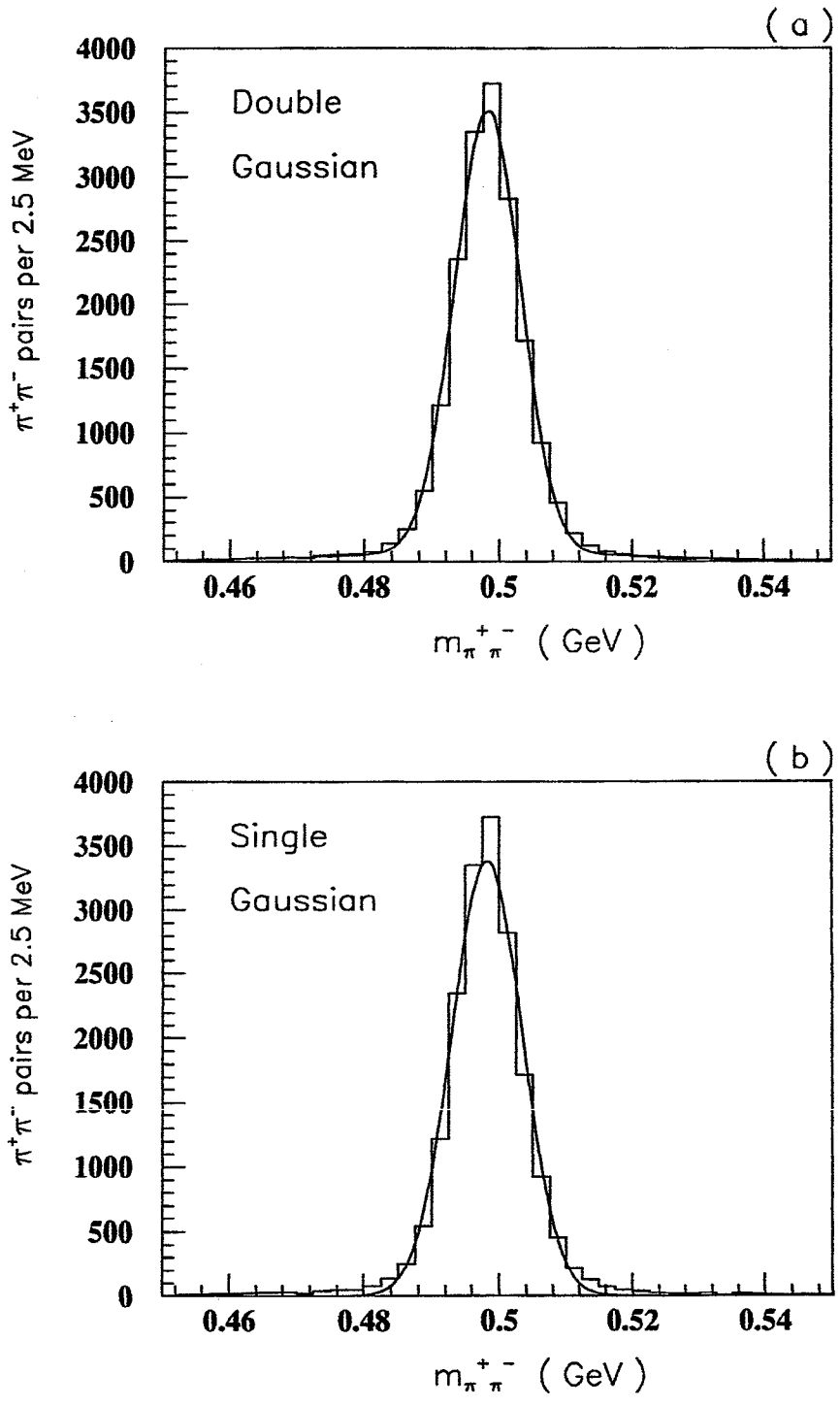

Figure 5.13: The reconstructed mass distribution for "tagged" MC candidates ($K_s^0 \to \pi^+\pi^-$), fitted to (a) a double Gaussian function and (b) a single Gaussian function.

Table 5.2: Comparison of the single Gaussian, the double Gaussian and the background subtraction techniques for the estimation of the differential signals. The entries under the "TREE" (from JETSET MC), represent the actual true number of $\#K_s^0 \to \pi^+\pi^-$ that pass the optimised cuts.

$P_{K_s^0} - range$ (GeV/c)	$\#K_s^0 \to \pi^+\pi^-$ (TREE)	$\#K_s^0 \to \pi^+\pi^-$ (Single) (Gaussian)	$\#K_s^0 \to \pi^+\pi^-$ (Double) (Gaussian)	$\#K_s^0 \to \pi^+\pi^-$ (Bkg. Sub.)
(0.5, 1.)	1504	1565 ± 39	1531 ± 44	1520 ± 41
(1., 2.)	4559	4306 ± 65	4654 ± 76	4444 ± 75
(2., 3.)	3706	3454 ± 66	3640 ± 74	3875 ± 72
(3., 4.)	2816	2494 ± 51	2696 ± 66	2875 ± 63
(4., 5.)	1961	1717 ± 44	1848 ± 56	1985 ± 53
(5., 7.)	2719	2354 ± 51	2711 ± 64	2773 ± 62
(7., 10.)	2124	1832 ± 47	2102 ± 56	2127 ± 53
(10.,20.)	1930	1481 ± 40	1725 ± 51	1776 ± 48
(20., 45.)	228	195 ± 16	218 ± 17	206 ± 17
	21608	19337 ± 146	21125 ± 176	21581 ± 169

of $K_s^0 \to \pi^+\pi^-$ as determined from the tree in Table 5.2. The two are in good agreement at 2% level.

From Table 5.2 it is evident that a single Gaussian significantly underestimates (by as much as 10%) the total number of entries under the mass peak.

5.3.7 The Acceptance Function for K_s^0

In determining an acceptance function for K_s^0 one is interested in those K_s^0 that arise as a direct result of the fragmentation process and carry information about the physics of annihilation process $e^+e^- \to Z^0 \to q\bar{q}$.

However, K_s^0 are also produced as a by–product of secondary interactions of already hadronised particles within the detector. Figure 5.14 show this production

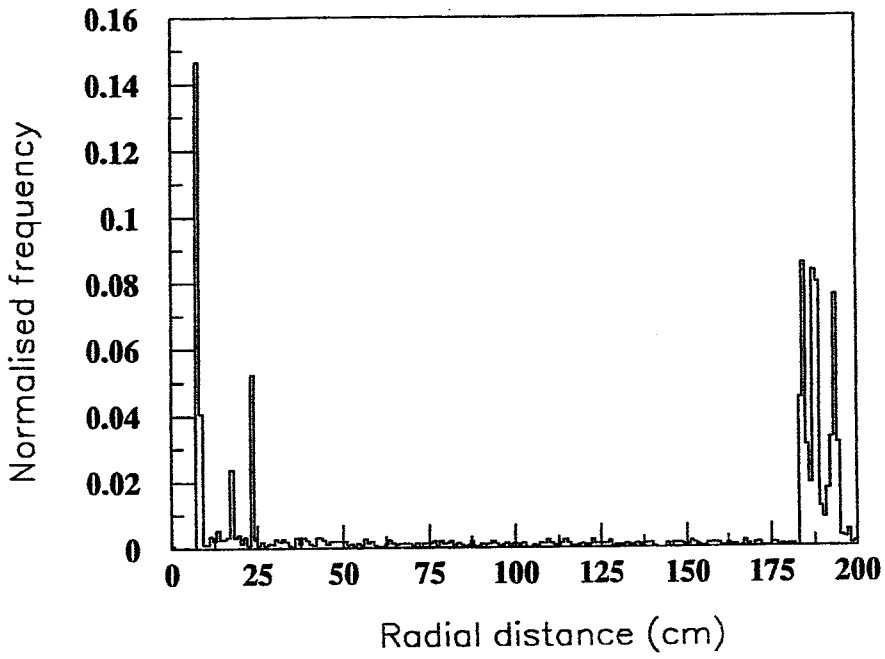

Figure 5.14: The radial distribution for the generation of K_s^0 resulting from hadronic interaction within the volume of the detector.

as a function of radius from the centre of the detector. As is seen, a large fraction of such K_s^0 are produced just outside the Central Detector. For any fragmentation study it is imperative to minimise the effect of this source of contamination. In Table 5.3 one sees clearly that the contribution from this secondary source is effectively removed by the optimised K_s^0 selection cuts.

The resultant momentum–dependent acceptance functions for the JETSET and the HERWIG MC samples based on the optimised cuts is shown in Figure 5.15 and is tabulated in Table 5.4, where the number estimation is in terms of a double Gaussian and a quadratic background fit. To improve statistical accuracy, the weighted mean of the HERWIG and JETSET acceptances (statistically compatible) has been used. The resulting K^0 data sample with its associated double Gaus-

Table 5.3: Fragmentation versus secondary hadronisation (detector produced) contributions to the actual number of $K_s^0 \to \pi^+\pi^-$ passing the optimised cuts, using the JETSET MC sample.

$P_{K_s^0}$−range (GeV/c)	Fragmentation		Secondary Hadronisation	
	$\#K_s^0$	$\#K_s^0 \to \pi^+\pi^-$	$\#K_s^0$	$\#K_s^0 \to \pi^+\pi^-$
(0., 0.5)	–	–	–	–
(0.5, 1.)	20647	1565	741	1
(1., 2.)	29705	4559	586	2
(2., 3.)	19015	3706	289	0
(3., 4.)	13714	2816	137	1
(4., 5.)	10155	1961	117	1
(5., 7.)	14129	2719	121	1
(7., 10.)	11664	2124	88	1
(10., 20.)	12130	1930	47	1
(20., 45.)	2184	228	6	0

sian fit and the quadratic background is shown in Figure 5.16. It contains an estimated number of 13630±158 reconstructed $K_s^0 \to \pi^+\pi^-$ events. The reconstructed mass associated with the peak is: $m_{K^0} = 497.4 \pm 0.1$ MeV, which agrees very well with the quoted value by the Particle Data Group [48] of 497.67 ± 0.03 MeV.

5.3.8 Fragmentation Independent Distributions

Having selected the K_s^0 data sample, it is then desirable to check its "quality" by studying some fragmentation–independent distributions. The two distributions looked at here are the $c\tau$ (where τ is the proper mean life of K_s^0), and the helicity angle of the negative daughter track.

The corrected $c\tau$ distribution is presented in Table 5.5. The mean value of $c\tau$ for K_s^0 from a fit to this distribution is $c\tau = 2.78 \pm 0.10$ cm which is in good

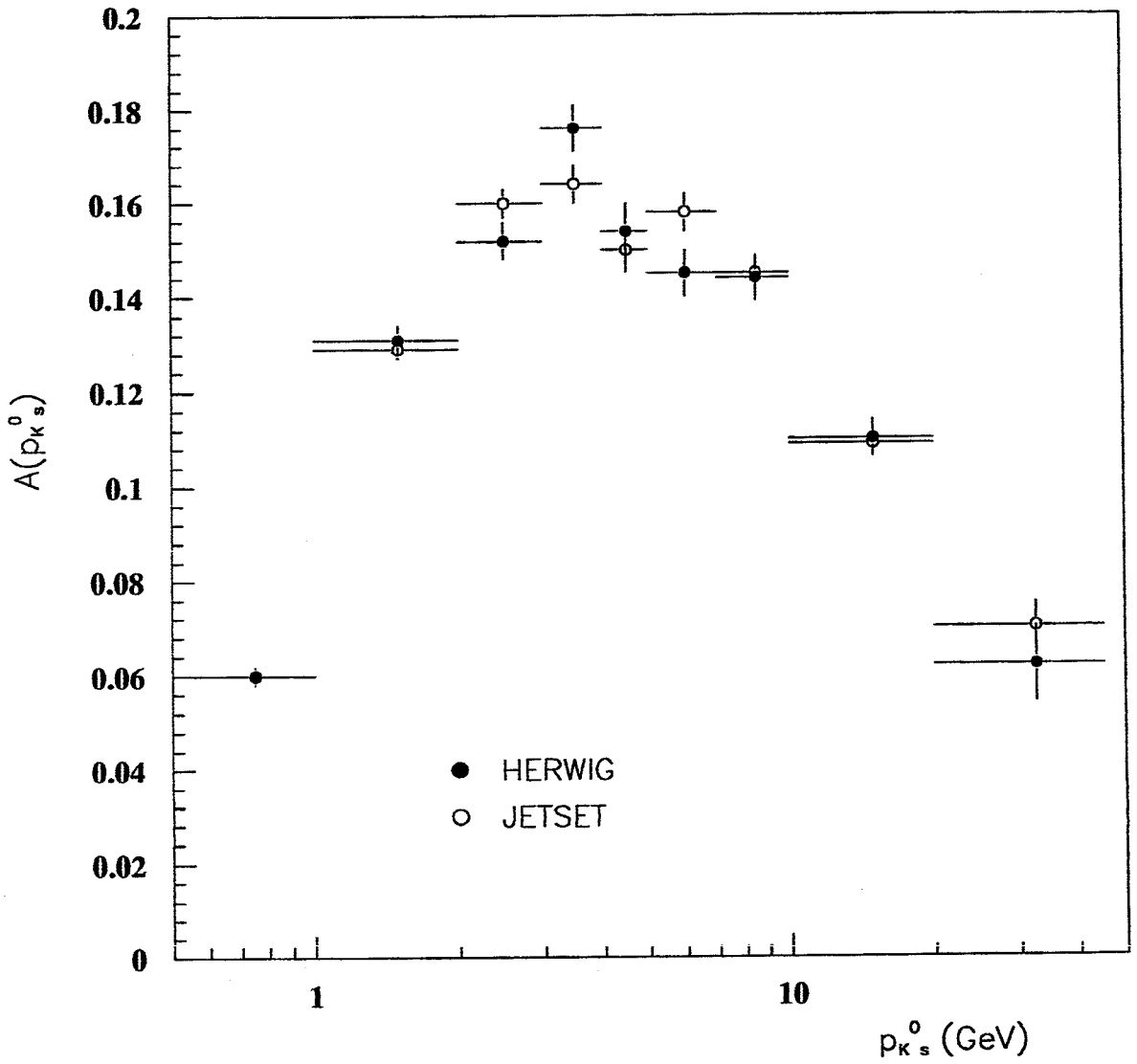

Figure 5.15: The resultant acceptance function for reconstructing $K^0_s \to \pi^+\pi^-$.

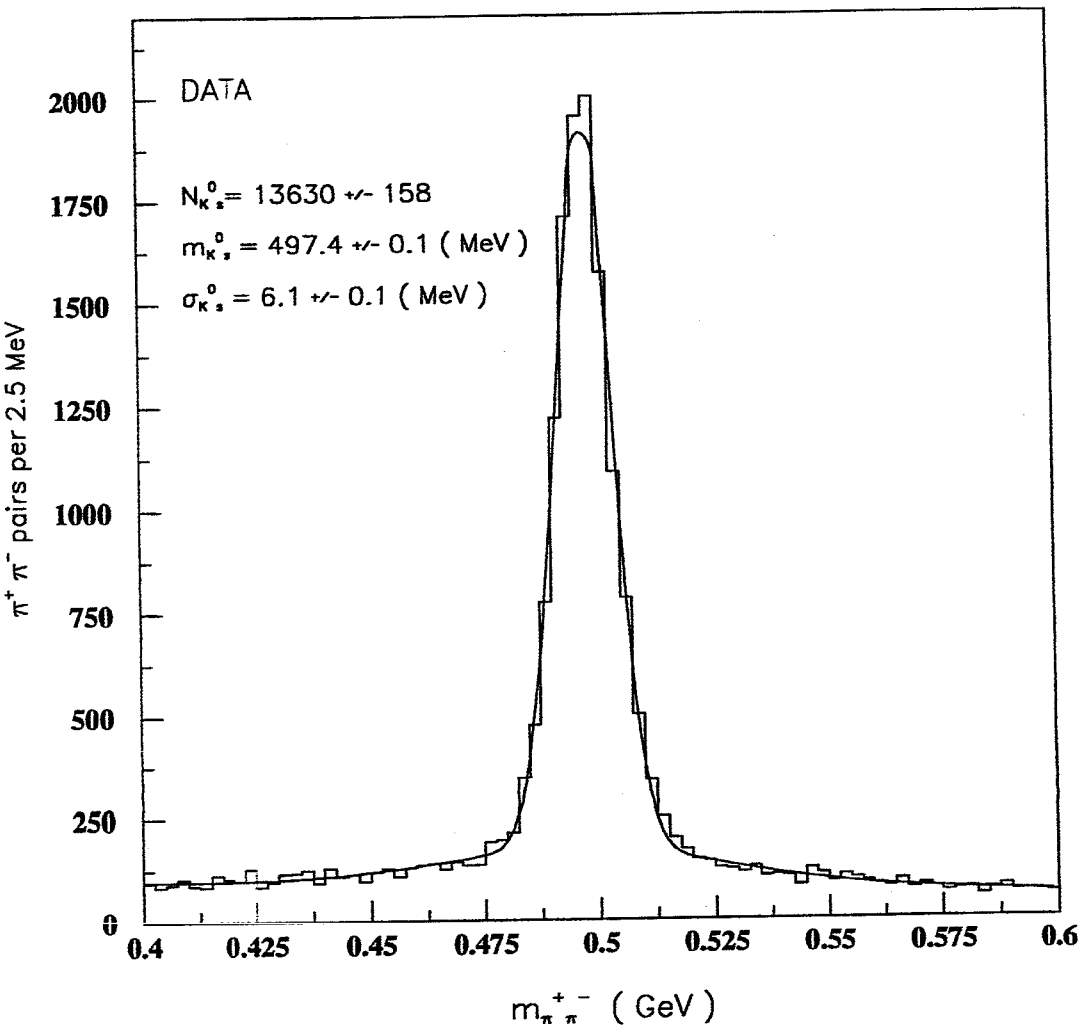

Figure 5.16: The reconstructed mass distribution for $K^0_s \rightarrow \pi^+\pi^-$ resulting from the application of the optimised cuts.

Table 5.4: The weighted mean momentum–dependent acceptance function, based on the HERWIG and the JETSET MC samples. Subscript "HW" refers to HERWIG while subscript "JT" refers to JETSET.

$P_{K^0_s} - range$ (GeV/c)	A_{HW}	A_{JT}	$\langle A \rangle$
(0., 0.5)	–	–	–
(0.5, 1.)	0.060± 0.002	0.060 ±0.002	0.060 ± 0.002
(1., 2.)	0.131 ± 0.003	0.129 ± 0.002	0.130 ± 0.002
(2., 3.)	0.152 ± 0.004	0.160 ± 0.003	0.157 ± 0.003
(3., 4.)	0.176 ± 0.005	0.164 ± 0.004	0.168 ± 0.003
(4., 5.)	0.154 ± 0.006	0.150 ± 0.005	0.152 ± 0.006
(5., 7.)	0.145 ± 0.005	0.158 ± 0.004	0.153 ± 0.003
(7., 10.)	0.144 ± 0.005	0.145 ± 0.004	0.144 ± 0.003
(10.,20.)	0.110 ± 0.004	0.109 ± 0.003	0.110 ± 0.002
(20., 45.)	0.062 ± 0.008	0.070 ± 0.005	0.068 ± 0.004

agreement with the world average as quoted by the particle data group [48] of 2.68 cm.

The decay angle for the -ve (or +ve) pion in the rest frame of the K^0 is referred to as the helicity angle of the -ve (or +ve) track. Since the K^0 has spin zero, this decay distribution is expected to be isotropic. The corrected distribution for the helicity angle of the -ve track does indeed exhibit this expected behaviour as is seen in Figure 5.17(b).

5.3.9 Systematic Effects

Systematic uncertainties could arise due to the manner in which a certain technique handles a specific measurement. It is very important to be able to identify and account for the major sources of systematics in any measurement as no amount of accumulated statistics eliminate these. The approach for estimating

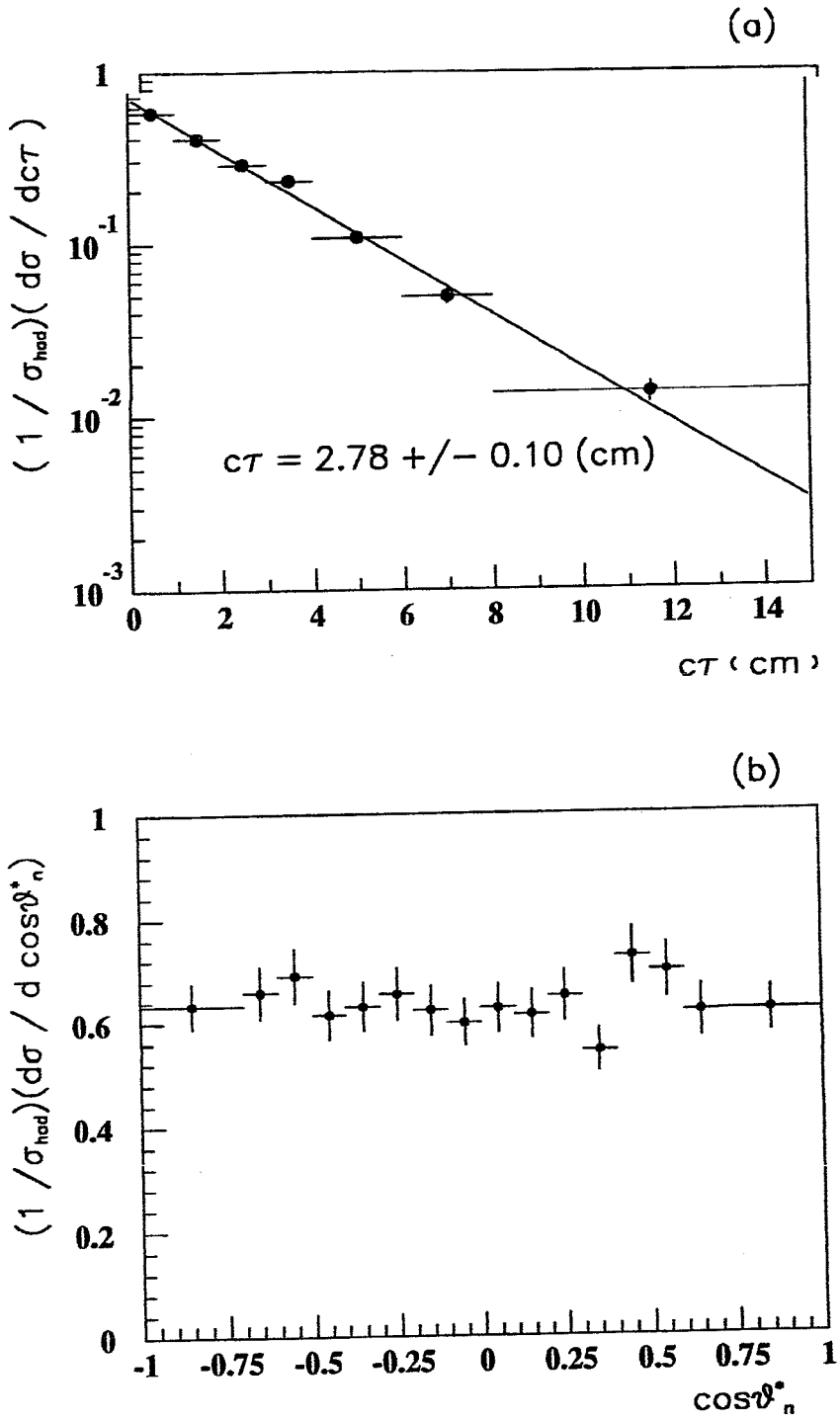

Figure 5.17: Fragmentation independent distributions for K^0. (a) life time distribution (b) helicity angle of the -ve daughter.

Table 5.5: Proper mean life distribution for K^0_s. The quoted error is statistical. There is a 7% systematic error.

$c\tau$ (cm)	$\#K^0_s \to \pi^+\pi^-$ "Raw"	$\rho^{CJ/CZ}_{K^0_s}$	$A(c\tau)$	$\frac{1}{\sigma_{had}}\frac{d\sigma}{d(c\tau)}$ (cm^{-1})
(0.,1.)	2158±60	1.256±0.001	0.069±0.001	0.5606±0.0156
(1.,2.)	4037±77	1.251±0.001	0.181±0.003	0.3966±0.0076
(2.,3.)	2944±62	1.246±0.001	0.184±0.003	0.2824±0.0056
(3.,4.)	2041±47	1.237±0.002	0.158±0.003	0.2265±0.0052
(4.,6.)	1429±44	1.230±0.002	0.116±0.003	0.1073±0.0033
(6.,8.)	351±23	1.208±0.003	0.062±0.003	0.0489±0.0033
(8.,15.)	112±15	1.192±0.003	0.020±0.002	0.0135±0.0017

these systematic errors is to vary specific cuts or parameters and then evaluate the corresponding change in the desired measured quantity. This change is then a measure of the systematics associated with the varied parameter.

In this section, the identified major sources of systematics for the K^0 inclusive production rate are discussed and evaluated from the corresponding inclusive momentum spectra. The measured rates are normalised to the corrected number of multihadronic data events which is $N_{had} = 140935$ (see Table 4.1).

The momentum region $P_{K^0} < 0.5$ GeV/c is inaccessible to the analysis due to the software selection cut on the transverse momentum of the tracks and is referred to as the "invisible momentum region". As a result, one needs to rely on the MC to account for this unobserved region. Below about 2 GeV/c, data exhibits a decreasing trend compared with the MC expectation (see Table 6.1). Because of this and the fact that a large fraction of K^0 production is in the low momentum range, one expects a large systematic uncertainty associated with the way the

Table 5.6: The distribution for the cosine of the decay angle in the rest frame of K^0_s (the **helicity angle**, θ^*) for the **negative track**, in the decay $K^0_s \to \pi^+\pi^-$. The quoted error is statistical. There is a 7% systematic error.

$\cos\theta^*_n$	$\#K^0_s \to \pi^+\pi^-$ "Raw"	$\rho^{CJ/CZ}_{K^0_s}$	$A(\cos\theta^*_n)$	$\frac{1}{\sigma_{had}}\frac{d\sigma}{d(\cos\theta^*_n)}$
(-1.00,-0.70)	1908±63	1.245±0.001	0.177±0.005	0.633±0.027
(-0.70,-0.60)	639±28	1.263±0.004	0.174±0.006	0.658±0.037
(-0.60,-0.50)	656±27	1.269±0.004	0.171±0.006	0.690±0.037
(-0.50,-0.40)	642±27	1.265±0.004	0.188±0.006	0.615±0.033
(-0.40,-0.30)	682±27	1.274±0.004	0.196±0.007	0.630±0.033
(-0.30,-0.20)	689±28	1.265±0.003	0.189±0.007	0.654±0.035
(-0.20,-0.10)	682±28	1.271±0.004	0.197±0.007	0.623±0.033
(-0.10,0.00)	683±27	1.275±0.004	0.207±0.007	0.598±0.030
(0.00,0.10)	693±27	1.275±0.004	0.200±0.007	0.626±0.032
(0.10,0.20)	663±27	1.271±0.004	0.195±0.007	0.614±0.032
(0.20,0.30)	714±28	1.263±0.004	0.197±0.006	0.649±0.033
(0.30,0.40)	611±26	1.263±0.004	0.201±0.007	0.545±0.029
(0.40,0.50)	677±28	1.257±0.004	0.166±0.006	0.726±0.040
(0.50,0.60)	670±27	1.260±0.005	0.178±0.006	0.697±0.038
(0.60,0.70)	596±27	1.253±0.005	0.171±0.006	0.619±0.036
(0.70,1.00)	1718±63	1.204±0.002	0.158±0.004	0.621±0.029

invisible momentum region is handled. The JETSET MC estimates that 7% of the total K^0 production lies in the (0.,0.5) GeV/c momentum range. The final K^0 multiplicity is determined by including the 7% unobserved production rate, which then gives a measured multiplicity of 1.95±0.03(stat.) for K^0. The systematic uncertainty is then estimated by varying the position of the momentum cut–off up to 1.0 GeV/c. The resulting systematic uncertainty is estimated to be 4.6% from the K^0 rate of 2.04±0.02 using $p > 1.0$ GeV/c.

Previously it was discussed (see section 5.3.4.) how the different CJ/CZ

matching properties for the data and the MC were accounted for in terms of a matching efficiency correction factor ($\rho_{K^0_s}$). The matching efficiency employed in this analysis is based on all K^0 candidates, with no associated m_{K^0} mass cuts. Alternatively, one could determine the matching efficiency based on those K^0 candidates that survive the optimised cuts and fall in the mass range (0.45,0.55) GeV. This is shown in Table 5.7. The associated systematic has been determined to be 2.1% from the corresponding rate of 1.99±0.03.

Another marked difference between the data and the MC behaviour is seen in the number of CJ hit distributions associated with +ve and −ve tracks for track momenta below about 1 GeV/c. Figure 5.18 shows this effect. The −ve tracks behave similarly while +ve tracks have quite different distributions. The systematic associated with this parameter was estimated by increasing the minimum number of CJ hit requirements up to 50 hits on both daughter tracks making up the K^0_s. The K^0 rate was then determined to be (see Table 5.8) 1.91±0.03, i.e. a systematic of 2.1%.

The multihadronic selection criteria used a track transverse momentum of $p_T >$ 0.15 GeV/c. The systematic effect of this cut was studied by increasing the threshold level to 0.25 GeV/c. The resulting rate was determined to be 1.96±0.03 (see Table 5.9), i.e. a 0.5% systematic effect.

The motivation for requiring CJ/CZ matching (and hence the introduction of a matching efficiency correction factor) was to obtain improved z measurement. From Figures 5.7 and 5.8, it is clear that single track matching efficiency behaviour for the data and the MC are markedly different in the ragne $0.6 \leq |\cos(\theta_{trk})| \leq 0.7$. This is understood in terms of an "edge effect" associated with CJ/CZ matching. The systematic uncertainty has been studied by tightening the cosine of the polar

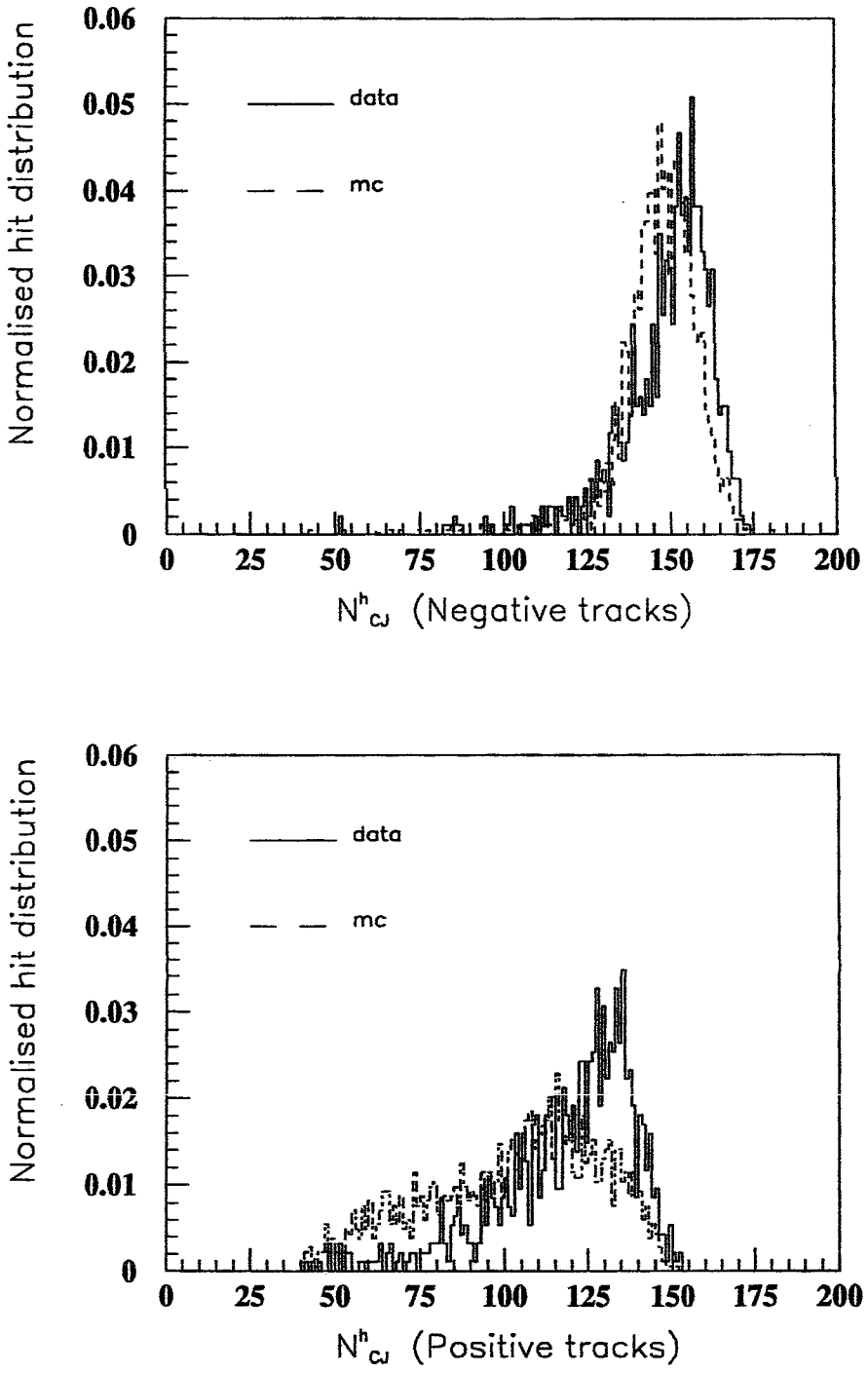

Figure 5.18: CJ hit distributions for −ve and +ve tracks below 1 GeV/c.

angle to be well within the barrel region of the Central Detector: $|\cos(\theta_{trk})| \leq 0.6$. The resulting rate is 1.96±0.03 with an associated systematic of 0.5% (See Table 5.10).

For a neutral particle like K^0, produced in the fragmentation process, one expects the impact parameter with respect to the beam spot, $RMISS = d_{0V}$, to be small as its trajectory is not influenced by the axial magnetic field in the Central Detector. The systematic associated with this cut was studied by requiring the impact parameter for K^0 to be less that 0.5 cm. The corresponding measured rate for K^0 was 1.97±0.03, i.e. a systematic effect of 1.0% (See Table 5.11).

The sum impact parameter, $|d_{01}| + |d_{02}|$, was found to be by far the most efficient cut for reducing background. An estimate for the systematic uncertainty associated with this cut was obtained by reducing this cut to 0.4 cm, i.e. $|d_{01}| + |d_{02}| > 0.4$. The resulting K^0 rate was 1.91±0.03 which corresponds to a systematic of 2.1% (See Table 5.12).

The systematic effect for χ^2_{pseudo} was determined by increasing this cut to 15. The corresponding rate was estimated to be 1.98±0.03 which represents a 1.5% systematic (See Table 5.13).

The differential mass peaks for the reconstructed $K^0_s \rightarrow \pi^+\pi^-$ candidates were fitted with a double Gaussian plus a quadratic background over the mass range (0.4,0.6) GeV. The associated systematic was estimated by increasing the range of the fit to (0.4,0.7) GeV, resulting in a rate of 1.88±0.03 which is a systematic of 3.5% (See Table 5.14).

Lastly, the systematic associated with the choice of the generator was investigated by estimating rates based on JETSET and HERWIG MC samples separately. By using the HERWIG MC sample the K^0 rate was estimated to be 1.97±0.03 (see

Table 5.15), while the use of JETSET MC sample resulted in a rate of 1.95± 0.03. This corresponds to a systematic effect of 1.0%.

Table 5.16 summarises the studied systematic uncertainties for the measured production rate of K^0.

Finally, the matter of the initial state radiation (ISR) is addressed. At the Z^0−peak, the relatively large width of the Z^0−peak means that initial state radiation does not affect the hadron production cross–section that appreciably. This was verified by running the JETSET MC with and without the initial state radiation; the result shows no statistical difference between the two cases. This is seen in Table 5.17. The quoted momentum distributions are for 10^6 JETSET multihadronic events.

5.4 Summary

From a sample of 131253 multihadronic events, employing the optimised K^0 finding cuts, a total of 13630 $K^0_s \rightarrow \pi^+\pi^-$ have been reconstructed. The acceptance for these cuts has been determined, where the chosen functional form used in estimating the acceptance function was a double Gaussian plus a quadratic background. The different CJ/CZ matching behaviour for the data and the MC has been accounted for in terms of a matching efficiency correction factor. The systematic effects associated with K^0 rate extraction have been discussed and estimated. The reliability of this K^0_s sample has been verified by studying two fragmentation–independent distributions: $c\tau$ and helicity angle.

In conclusion, the K^0_s sample is unbiased and can now be used to study the single K^0 production characteristics in multihadronic events. These will be dealt with in the next chapter.

Table 5.7: Systematics associated with CJ/CZ matching efficiency.

$P_{K^0_s} - range$ (GeV/c)	$\#K^0_s \to \pi^+\pi^-$ "Raw"	$\rho^{CJ/CZ}_{K^0_s}$	A	$\#\ (K^0, \overline{K^0})$
(0., 0.5)	–	–	–	–
(0.5, 1.)	767±29	1.136±0.002	0.060±0.002	29036±1468
(1., 2.)	2722 ±65	1.210±0.002	0.129±0.002	51064±1456
(2., 3.)	2606±68	1.248±0.002	0.160±0.003	40667±1308
(3., 4.)	1802±61	1.295±0.004	0.164±0.004	28452±1190
(4., 5.)	1352±49	1.320±0.007	0.150±0.005	23799±1178
(5., 7.)	1562±56	1.313±0.005	0.158±0.004	25953±1143
(7., 10.)	1321±47	1.313±0.003	0.145±0.004	23915±1078
(10.,20.)	1274±44	1.308±0.003	0.109±0.003	30564±1351
(20., 45.)	164±16	1.271±0.007	0.070±0.005	7571±917
Total				261021±3732

Table 5.8: Systematics associated with the number of CJ hits, $N^h_{CJ} > 50$.

$P_{K^0_s} - range$ (GeV/c)	$\#K^0_s \to \pi^+\pi^-$ "Raw"	$\rho^{CJ/CZ}_{K^0_s}$	A	$\#\ (K^0, \overline{K^0})$
(0., 0.5)	–	–	–	–
(0.5, 1.)	780±29	1.139±0.002	0.059±0.002	30127±1516
(1., 2.)	2731 ±63	1.205±0.001	0.125±0.002	52671±1479
(2., 3.)	2361±69	1.240±0.001	0.158±0.003	37056±1292
(3., 4.)	1799±61	1.258±0.001	0.165±0.004	27434±1144
(4., 5.)	1309±49	1.269±0.001	0.157±0.004	21157±958
(5., 7.)	1518±56	1.276±0.001	0.157±0.004	24677±1106
(7., 10.)	1335±47	1.276±0.001	0.139±0.004	24516±1129
(10.,20.)	1157±43	1.269±0.001	0.108±0.003	27196±1262
(20., 45.)	158±17	1.257±0.002	0.068±0.005	5841±761
Total				250675±3613

Table 5.9: Systematics associated with the track transverse momentum. $|p_T| > 0.25$ GeV/c.

$P_{K^0_s} - range$ (GeV/c)	$\#K^0_s \to \pi^+\pi^-$ "Raw"	$\rho^{CJ/CZ}_{K^0_s}$	A	$\#\ (K^0, \overline{K^0})$
(0., 0.5)	–	–	–	–
(0.5, 1.)	592±26	1.139±0.002	0.045±0.001	29979±1476
(1., 2.)	2419 ±57	1.199±0.001	0.105±0.002	55259±1674
(2., 3.)	2139±61	1.229±0.001	0.129±0.004	40753±1717
(3., 4.)	1994±59	1.244±0.001	0.172±0.004	28843±1086
(4., 5.)	1413±49	1.252±0.001	0.149±0.004	23744±1041
(5., 7.)	1561±56	1.258±0.001	0.158±0.004	24865±1092
(7., 10.)	1321±48	1.258±0.001	0.145±0.004	22922±1046
(10.,20.)	1093±44	1.252±0.001	0.110±0.004	25002±1216
(20., 45.)	164±16	1.238±0.001	0.069±0.005	5883±715
Total				257250±3804

Table 5.10: Systematics associated with the cos(polar angle of the track). $|\cos\theta_{ctrk}| < 0.6$.

$P_{K^0_s} - range$ (GeV/c)	$\#K^0_s \to \pi^+\pi^-$ "Raw"	$\rho^{CJ/CZ}_{K^0_s}$	A	$\#\ (K^0, \overline{K^0})$
(0., 0.5)	–	–	–	–
(0.5, 1.)	599±25	1.132±0.001	0.046±0.002	29468±1776
(1., 2.)	2260 ±32	1.192±0.001	0.103±0.002	52287±1257
(2., 3.)	2182±62	1.221±0.001	0.129±0.003	41302±1517
(3., 4.)	1444±56	1.239±0.001	0.132±0.004	27101±1334
(4., 5.)	1124±45	1.247±0.001	0.129±0.004	21725±1100
(5., 7.)	1300±51	1.253±0.001	0.131±0.003	24877±1130
(7., 10.)	1140±44	1.253±0.001	0.120±0.004	23811±1095
(10.,20.)	1058±40	1.248±0.001	0.089±0.003	29667±1503
(20., 45.)	129±15	1.234±0.002	0.053±0.005	6008±900
Total				256246±3946

Table 5.11: Systematics associated with the impact parameter for K^0_s. $RMISS < 0.5$ cm.

$P_{K^0_s} - range$ (GeV/c)	$\#K^0_s \to \pi^+\pi^-$ "Raw"	$\rho^{CJ/CZ}_{K^0_s}$	A	$\#(K^0, \overline{K^0})$
(0., 0.5)	–	–	–	–
(0.5, 1.)	759±29	1.139±0.002	0.060±0.002	28827±1462
(1., 2.)	2785 ±67	1.205±0.001	0.129±0.002	52047±1490
(2., 3.)	2625±58	1.240±0.001	0.160±0.003	40684±1179
(3., 4.)	1795±65	1.258±0.001	0.166±0.004	27208±1184
(4., 5.)	1223±53	1.269±0.001	0.152±0.005	20418±1111
(5., 7.)	1648±60	1.276±0.001	0.159±0.004	26453±1171
(7., 10.)	1343±52	1.276±0.001	0.145±0.004	23642±1124
(10., 20.)	1386±48	1.269±0.001	0.108±0.004	32579±1446
(20., 45.)	178±17	1.257±0.001	0.073±0.006	6130±772
Total				257988±3702

Table 5.12: Systematics associated with the sum impact parameters. $|d_{01}| + |d_{02}| > 0.4$ cm.

$P_{K^0_s} - range$ (GeV/c)	$\#K^0_s \to \pi^+\pi^-$ "Raw"	$\rho^{CJ/CZ}_{K^0_s}$	A	$\#(K^0, \overline{K^0})$
(0., 0.5)	–	–	–	–
(0.5, 1.)	789±29	1.139±0.002	0.061±0.002	29475±1452
(1., 2.)	2891 ±72	1.205±0.001	0.135±0.002	51627±1497
(2., 3.)	2695±74	1.240±0.001	0.174±0.003	38408±1376
(3., 4.)	1869±68	1.258±0.001	0.184±0.004	25559±1083
(4., 5.)	1404±56	1.269±0.001	0.167±0.005	21334±1064
(5., 7.)	1816±64	1.276±0.001	0.174±0.004	26637±1121
(7., 10.)	1385±54	1.276±0.001	0.158±0.003	22376±970
(10., 20.)	1424±51	1.269±0.001	0.128±0.004	28242±1342
(20., 45.)	220±18	1.257±0.001	0.085±0.006	6507±703
Total				250165±3611

Table 5.13: Systematics associated with the pseudo–chisquare, $\chi^2_{pseudo} < 15$.

$P_{K^0_s} - range$ (GeV/c)	$\#K^0_s \to \pi^+\pi^-$ "Raw"	$\rho^{CJ/CZ}_{K^0_s}$	A	$\#\ (K^0, \overline{K^0})$
(0., 0.5)	–	–	–	–
(0.5, 1.)	770±31	1.139±0.002	0.060±0.002	29245±1529
(1., 2.)	2812 ±66	1.205±0.001	0.130±0.002	52147±1464
(2., 3.)	2684±70	1.240±0.001	0.158±0.003	42125±1393
(3., 4.)	1854±62	1.258±0.001	0.164±0.004	28445±1178
(4., 5.)	1374±50	1.269±0.001	0.154±0.004	22641±1012
(5., 7.)	1629±57	1.276±0.001	0.159±0.004	26148±1127
(7., 10.)	1349±48	1.276±0.001	0.147±0.004	23425±1049
(10.,20.)	1288±45	1.269±0.001	0.109±0.003	29997±1334
(20., 45.)	164±16	1.257±0.002	0.070±0.005	5890±712
Total				260063±3498

Table 5.14: Systematics associated with the fit procedure.

$P_{K^0_s} - range$ (GeV/c)	$\#K^0_s \to \pi^+\pi^-$ "Raw"	$\rho^{CJ/CZ}_{K^0_s}$	A	$\#\ (K^0, \overline{K^0})$
(0., 0.5)	–	–	–	–
(0.5, 1.)	767±29	1.139±0.002	0.060±0.002	29131±1469
(1., 2.)	2611±62	1.205±0.001	0.125±0.002	50357±1442
(2., 3.)	2587±67	1.240±0.001	0.171±0.003	37516±1174
(3., 4.)	1784±59	1.258±0.001	0.174±0.004	25798±1039
(4., 5.)	1384±48	1.269±0.001	0.162±0.004	21679±923
(5., 7.)	1734±54	1.276±0.001	0.163±0.004	27150±1077
(7., 10.)	1360±46	1.276±0.001	0.149±0.004	23299±1006
(10.,20.)	1172±43	1.269±0.001	0.116±0.003	25649±1151
(20., 45.)	165±16	1.257±0.002	0.068±0.005	6100±800
Total				246679±3418

Table 5.15: Systematics associated with the generator choice, HERWIG.

$P_{K^0_s} - range$ (GeV/c)	$\#K^0_s \to \pi^+\pi^-$ "Raw"	$\rho^{CJ/CZ}_{K^0_s}$	A	$\#\ (K^0, \overline{K^0})$
(0., 0.5)	–	–	–	–
(0.5, 1.)	767±29	1.145±0.002	0.060±0.002	29359±1550
(1., 2.)	2722±65	1.211±0.001	0.131±0.003	50356±1667
(2., 3.)	2606±68	1.245±0.001	0.152±0.004	42754±1647
(3., 4.)	1802±61	1.260±0.001	0.176±0.005	25760±1176
(4., 5.)	1352±49	1.272±0.001	0.154±0.006	22282±1206
(5., 7.)	1562±56	1.277±0.001	0.145±0.005	27446±1351
(7., 10.)	1321±47	1.278±0.001	0.144±0.005	23460±1167
(10.,20.)	1274±44	1.274±0.001	0.110±0.004	29426±1493
(20., 45.)	164±16	1.266±0.002	0.062±0.008	6719±1082
Total				257562±4162

Table 5.16: Summary of systematic uncertainties associated with K^0 measured production rate.

Parameter	% systematic uncertainty
invisible Δp−region	4.6%
$\rho_{K^0_s}$	2.1%
N^h_{CJ}	2.1%
$\lvert p_T \rvert$	0.5%
$\lvert \cos(\theta_{ctrk}) \rvert$	0.5%
d_{0V}	1.0%
$\lvert d_{01} \rvert + \lvert d_{02} \rvert$	2.1%
χ^2_{pseudo}	1.5%
Fit range	3.5%
Generator choice (HERWIG)	1.0%
total (quadrature)	7.2%

Table 5.17: Effect of initial state radiation (ISR) on K^0 production momentum distribution. Result based on 10^6 generated JETSET multihadronic MC events.

p_{K^0} – range (GeV/c)	ISR **ON** $\#(K^0, \overline{K^0})$	ISR **OFF** $\#(K^0, \overline{K^0})$	Ratio (ON/OFF)
(0.,1.)	460760 ± 679	459860 ± 678	1.002 ± 0.002
(1.,2.)	443120 ± 666	441500 ± 664	1.004 ± 0.002
(2.,3.)	282140 ± 531	279940 ± 529	1.008 ± 0.003
(3.,4.)	199980 ± 447	200860 ± 448	0.996 ± 0.003
(4.,5.)	151160 ± 389	151000 ± 389	1.001 ± 0.004
(5.,7.)	209680 ± 458	210960 ± 459	0.994 ± 0.003
(7.,10.)	181200 ± 426	181120 ± 426	1.000 ± 0.003
(10.,20.)	191600 ± 438	191780 ± 438	0.999 ± 0.003
(20.,45.)	37500 ± 194	37940 ± 195	0.988 ± 0.007
	2157140 ± 1469	2154960 ± 1468	1.001 ± 0.001

Chapter 6

Results

The degree of success of a hadronisation model in describing particle production in e^+e^-annihilation is dependent not only on its ability to provide a reliable prediction for various inclusive particle production rates, but also on its capacity to generate detailed kinematic distributions that mimic the data. Hence one needs to investigate both production rates and differential distributions.

This chapter concentrates on one such study with K^0 as the primary particle of interest. Using the already obtained K^0_s data sample and the tuned MC samples, the inclusive production rate for K^0 is then determined from the momentum distribution. This is followed by a study of scaling and coherence effects for inclusive particle production. A number of distributions of interest are also studied, namely: longitudinal rapidity, transverse momenta in and out of the event plane and sphericity dependence of strangeness production.

6.1 Determination of the K^0 Inclusive Production Rate and Estimation of the Strangeness Suppression Factor

The inclusive production rate or the mean multiplicity per event for K^0, $n_{(K^0,\overline{K^0})}$, is defined as the average number of K^0 and its anti−particle, $\overline{K^0}$, that are produced per multihadronic event. Table 6.1 summarises the measured K^0 production rate as a function of its momentum. It is noted that the measured differential rate

Table 6.1: Data "Fragmentation Function". Optimized cuts $+ |cos(\theta_{clrk})| < 0.7 +$ two CZ "tracks". The rate is normalised to the corrected number of multihadronic data events which are $N_{had} = 140935$ (see Table 4.1). The A and $\rho_{K^0_s}^{CJ/CZ}$ are those as given in Tables 5.4 and 5.1.

$P_{K^0_s} - range$ (GeV/c)	# $K^0_s \to \pi^+\pi^-$ "Raw"	# $(K^0, \overline{K^0})_{DATA}$ Corrected	# $(K^0, \overline{K^0})_{MC}$ (JETSET)	$\frac{DATA}{MC}$
(0., 0.5)	–	–	–	–
(0.5, 1.)	767 ±29	29177±1471	43724±79	0.67±0.03
(1., 2.)	2722 ±65	50571±1437	62239±94	0.81±0.02
(2., 3.)	2606 ±68	41241±1334	39463±75	1.05±0.03
(3., 4.)	1802 ±61	27009±1034	28315±63	0.95±0.04
(4., 5.)	1352 ±49	22589±1012	21287±55	1.06±0.05
(5., 7.)	1562 ±56	26068±1065	29739±65	0.88±0.04
(7., 10.)	1321 ±47	23266±958	25533±60	0.96±0.04
(10.,20.)	1274 ±44	29441±1149	27035±62	1.09±0.04
(20., 45.)	164±16	6080±693	5602±28	1.09±0.12
	13570±153	255442±3457	282937±200	0.90±0.01

below about 2 GeV/c exhibits a decreasing trend compared with the JETSET expectation. The "invisible" region for the reconstructed K^0_s in the data is placed at 0.5 GeV/c. Including the 7% contribution from this inaccessible region of the momentum spectrum results in the final measured rate that is:

$$\langle n_{(K^0,\overline{K^0})} \rangle = 1.95 \pm 0.03(stat.) \pm 0.14(sys.) \qquad (6.1)$$

This value is somewhat lower than the JETSET and HERWIG predicted rates of 2.15 and 2.06 at 91.314 GeV respectively. Table 6.2 lists the K^0 measured mean multiplicities at different centre–of–mass energies from previous experiments. The present measured rate is to be compared with the DELPHI [49] LEP result of 2.12± 0.05±0.04 and the MARK II [50] at SLC value of 1.54±0.21±0.18. In Figure 6.1(a)

the measured K^0 production rates as a function of centre–of–mass energy are compared with the expectations of JETSET and HERWIG. The measured values agree generally quite well with the MC expectations, with the possible exception of MARK II at 91 GeV which is approximately 2σ below the the MC predicted values.

Based only on this K^0 rate measurement, one can now proceed to determine the strangeness suppression factor, γ_s (γ_s is defined as the ratio of the production of strange quark to up or down quark). Figure 6.1(b) shows the linear behaviour of γ_s with respect to the JETSET predicted K^0 production rate. The graphically determined value for the suppression factor based on the present rate is then:

$$\gamma_s = 0.25 \pm 0.03 \tag{6.2}$$

The error reflects both the statistical and systematic errors of the K^0 production rate. Table 6.3 gives a summary of the strangeness suppression factor (from K^0 production rate measurements) in e^+e^-annihilation experiments at various centre–of–mass energies. Strange particle production has also been studied in lepton–nucleon scattering where the νp and $\overline{\nu} p$ data from BEBC [59] indicates $\gamma_s \simeq 0.2$, while the EMC collaboration [60] result based on μp scattering finds $\gamma_s = 0.30 \pm 0.01(stat) \pm 0.07(sys)$. Malhotra and Orava [61] have complied data for hadron–hadron interactions from which they have deduced a weighted mean for the strangeness suppression factor of $\gamma_s = 0.30 \pm 0.02$. The available data from these various sources then indicates a value of γ_s in the range $0.2 - 0.3$ with no evidence for dependence on the centre–of–mass energy or reaction type.

This observed strangeness–suppression could be interpreted quite naturally in terms of the "flux–tube model" for particle production [27], where the confinement force field is treated as a one–dimensional string. The quark production process,

Table 6.2: K^0–multiplicity as a function of the centre-of-mass energy.

Experiment	$\sqrt{s}$ (GeV)	Reference	K^0 Mean Multiplicity
PLUTO	9.3–9.44	[51]	0.73±0.16
PLUTO	9.45–9.466	[51]	0.97±0.22
PLUTO	12	[51]	1.5±0.4
PLUTO	27.6–31.6	[51]	1.46±0.30
CLEO	9.46	[52]	1.05±0.13
JADE	12	[53]	1.14±0.38
JADE	14	[53]	1.05±0.21
JADE	22	[53]	1.27±0.29
JADE	30	[53]	1.49±0.22±0.15
JADE	34.5	[53]	1.45±0.23
TASSO	14.8	[54]	1.17±0.09±0.07
TASSO	22	[54]	1.28±0.11±0.08
TASSO	34.5	[54]	1.49±0.04±0.05
TASSO	35	[54]	1.47±0.03±0.05
TASSO	42.6	[54]	1.52±0.05±0.05
HRS	29	[55]	1.58±0.03±0.08
MARK II	29	[56]	1.27±0.03±0.15
MARK II	29	[50]	1.26±0.04±0.14
MARK II	91	[50]	1.54±0.21±0.18
TPC	29	[57]	1.22±0.03±0.15
CELLO	35	[58]	1.42±0.09±0.18
DELPHI	91	[49]	2.12±0.05±0.04
OPAL	91	This thesis	1.95±0.03±0.14

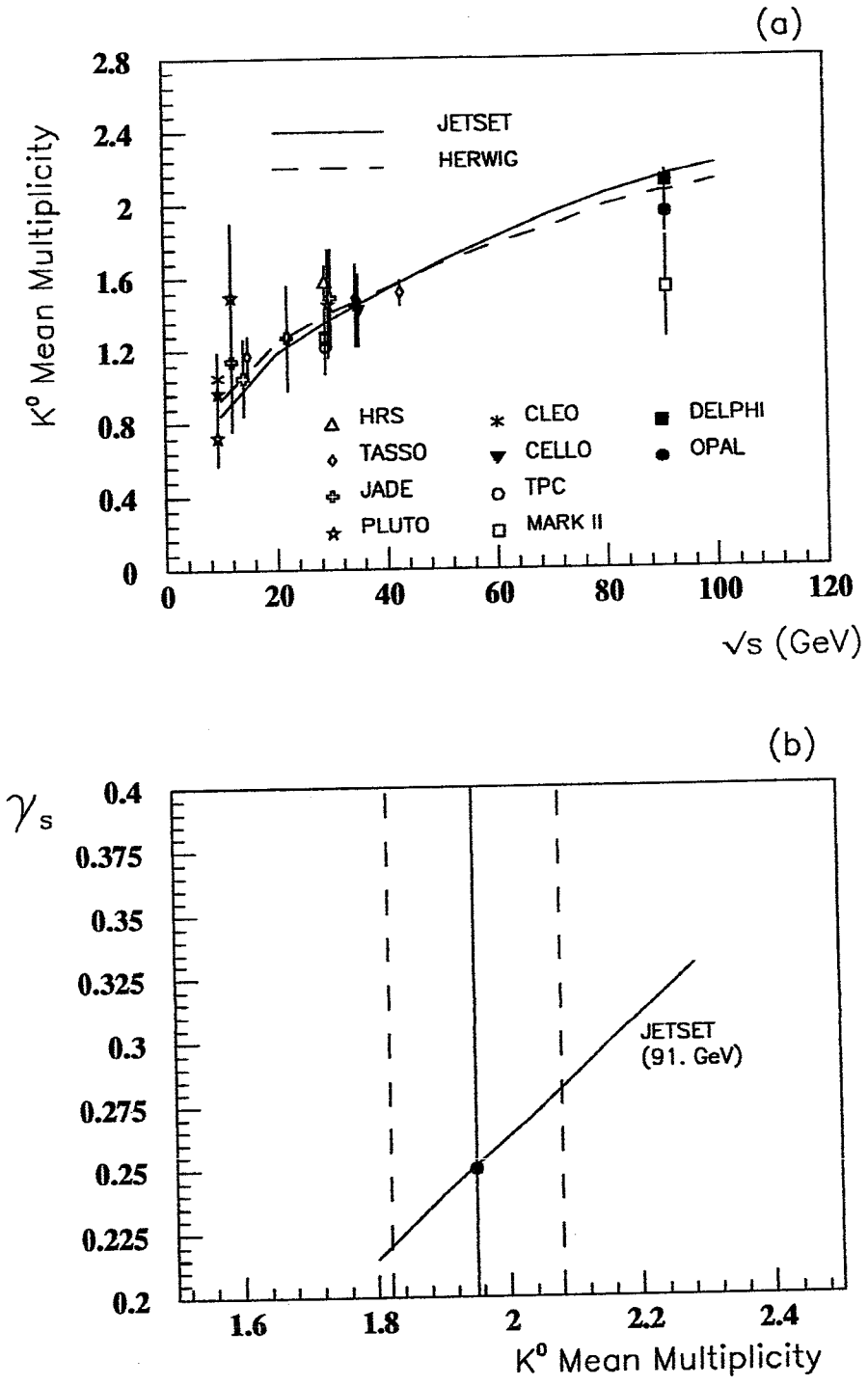

Figure 6.1: (a) Comparison of the measured mean multiplicity for K^0 with JETSET and HERWIG as a function of the centre–of–mass energy and (b) determination of the strangeness suppression factor at 91 GeV.

Table 6.3: Measured values of the strangeness suppression factor, γ_s, in e^+e^-annihilation experiments.

Experiment	$\sqrt{s}$ (GeV)	Reference	γ_s
JADE	12–35	[53]	0.27±0.03±0.05
TASSO	14–43	[54]	0.35±0.02±0.05
DELPHI	91	[49]	0.30±0.02
OPAL	91	This thesis	0.25±0.03
Average			0.29±0.02

in terms of string breaking, is essentially a tunnelling process and the strangeness suppression represents the SU(3) flavour breaking due to the larger mass of the strange quark. The "string constant" (energy per unit length of the string) is then a measure of time and momentum transfer involved in the confinement process.

6.2 K^0 Differential Production Cross–section as a Function of Scaled Energy Variable

The range of the momentum distribution for the production of particles is dependent on the energy of interaction, and so it is not suitable for comparison purposes at different centre–of–mass energies. This is remedied by using a related *scaled variable* that accounts for this differing production range. The variable chosen here is the *scaled energy variable*, x_E, defined as $x_E = 2E/\sqrt{s}$, where E is the energy of the particle and $\sqrt{s} = E_{CM}$ is the centre–of–mass energy. In this way, x_E lies in the range (0., 1.) irrespective of the initial interaction energy.

The K^0 scaling $(\frac{1}{\beta}\frac{1}{\sigma_{had}}\frac{d\sigma}{dx_E})$ and normalised $(\frac{1}{\sigma_{K^0}}\frac{d\sigma}{dx_E})$ cross–sections as a func-

tion of x_E are tabulated in Table 6.4. For the normalised cross–section, the distribution is normalised to unit area by using the appropriate measured rate.

Figure 6.2 presents the measured scaling cross-section along with the JETSET and the HERWIG MC predictions. One observes a very good agreement between the measured cross–section and the two MC expectations.

Comparisons with results from other experiments are presented in terms of both the scaling cross–section (as shown in Figure 6.3) and the normalised cross–section (as shown in Figure 6.4). Both distributions indicate scaling violation, with the LEP distributions (highest centre–of–mass energy) having the softest fragmentation. This can be understood as follows. As the centre–of–mass energy increases the number of emitted gluons increases which in turn results in larger multiplicity and a corresponding reduction in the fractional energy of individual produced particles. The other contributing factor is the effect of the different coupling of the γ and the Z^0 to quarks. Below the Z^0 peak, the coupling is purely QED and the strength of the coupling is determined by the square of the charge on the appropriate quark. At the Z^0 peak however, the coupling to various quarks is determined by the size of the electro–weak couplings (see section 1.5) and results in a more democratic distribution. Table 6.5 shows the production rate for the various quark flavours below, and at, the Z^0 peak. At the peak, the proportion of K^0 arising from heavier quark decays increases, thereby enhancing the softer component of the distribution.

6.3 K^0 Production Within Jets

The emphasis so far has been on single particle production distributions without any explicit reference to the jet nature of multihadronic events. The attention is

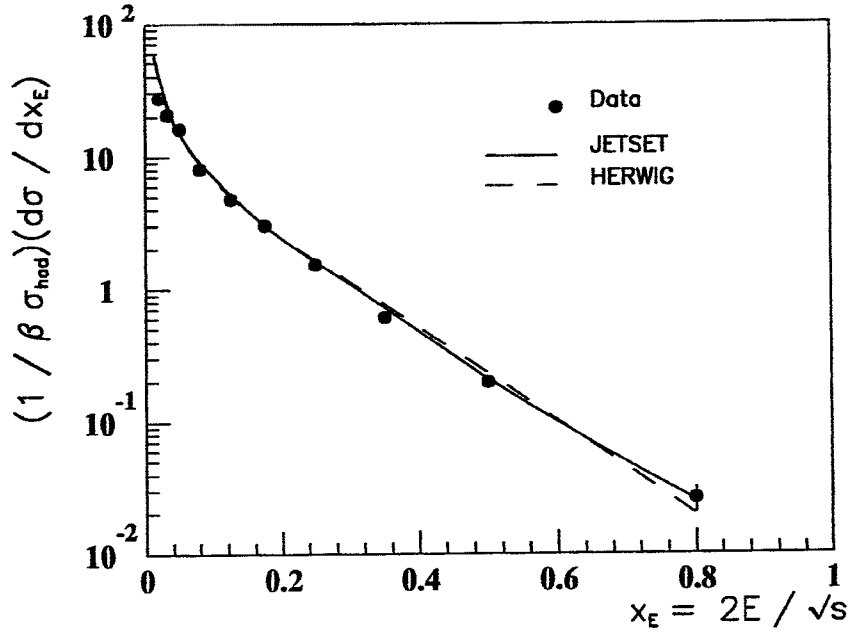

Figure 6.2: The scaling cross–section for inclusive K^0 production.

now turned to distributions that take the global shape and parameters of the event into account. Two kinematical variables that are often used to describe particle behaviour within jets are the longitudinal rapidity with respect to the thrust axis ($y_{\parallel}$) and the transverse momentum squared with respect to the thrust axis (P_T^2).

The investigation of transverse momentum properties for particles within jets, which is associated with hard gluon radiation, will be carried out in terms of two transverse momentum distributions: the transverse momentum (a) in the event plane (P_{Tin}) and (b) out of the event plane (P_{Tout}).

Finally, the dependence of strangeness production on event sphericity is also studied.

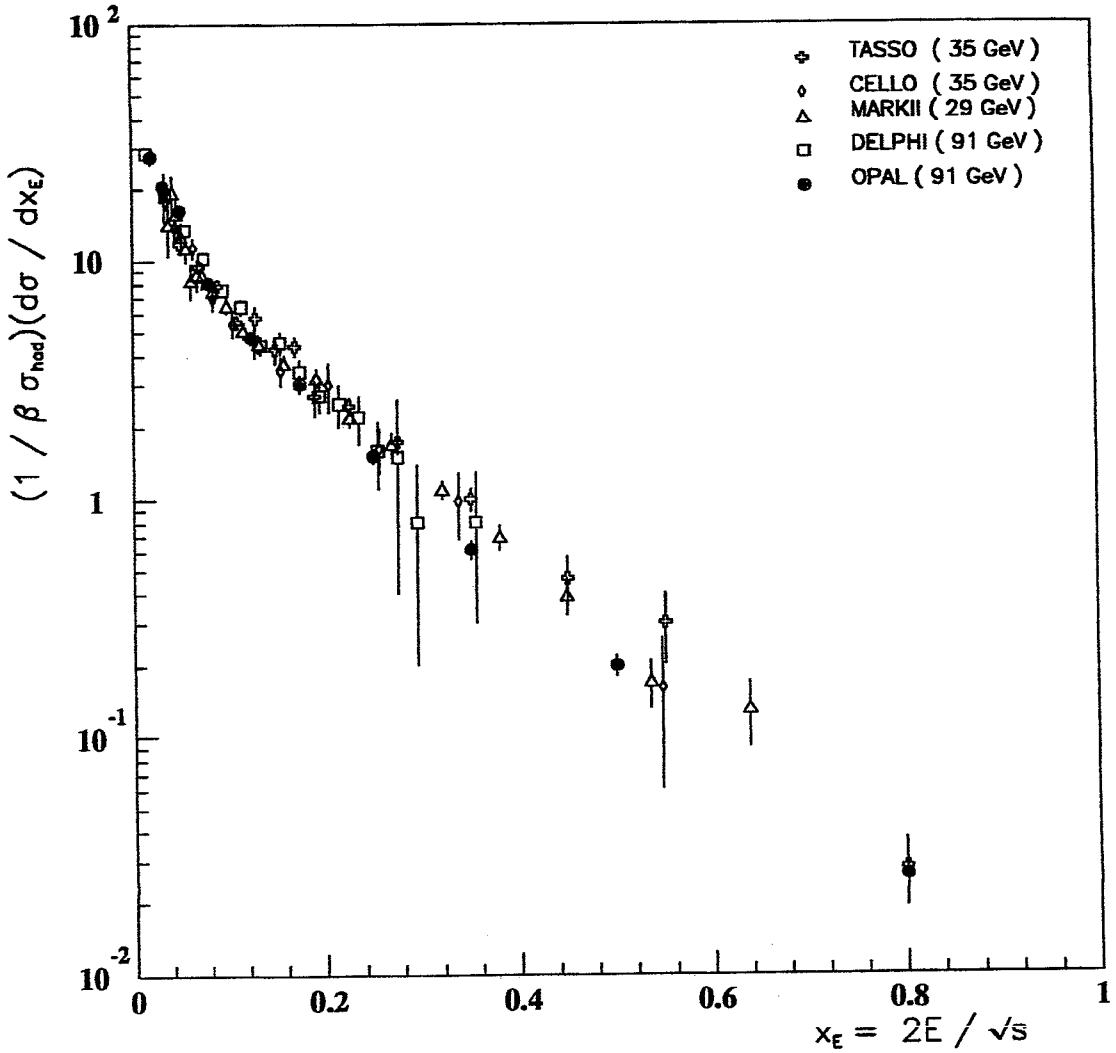

Figure 6.3: Comparison of measured scaling cross–sections for K^0 production at various energies.

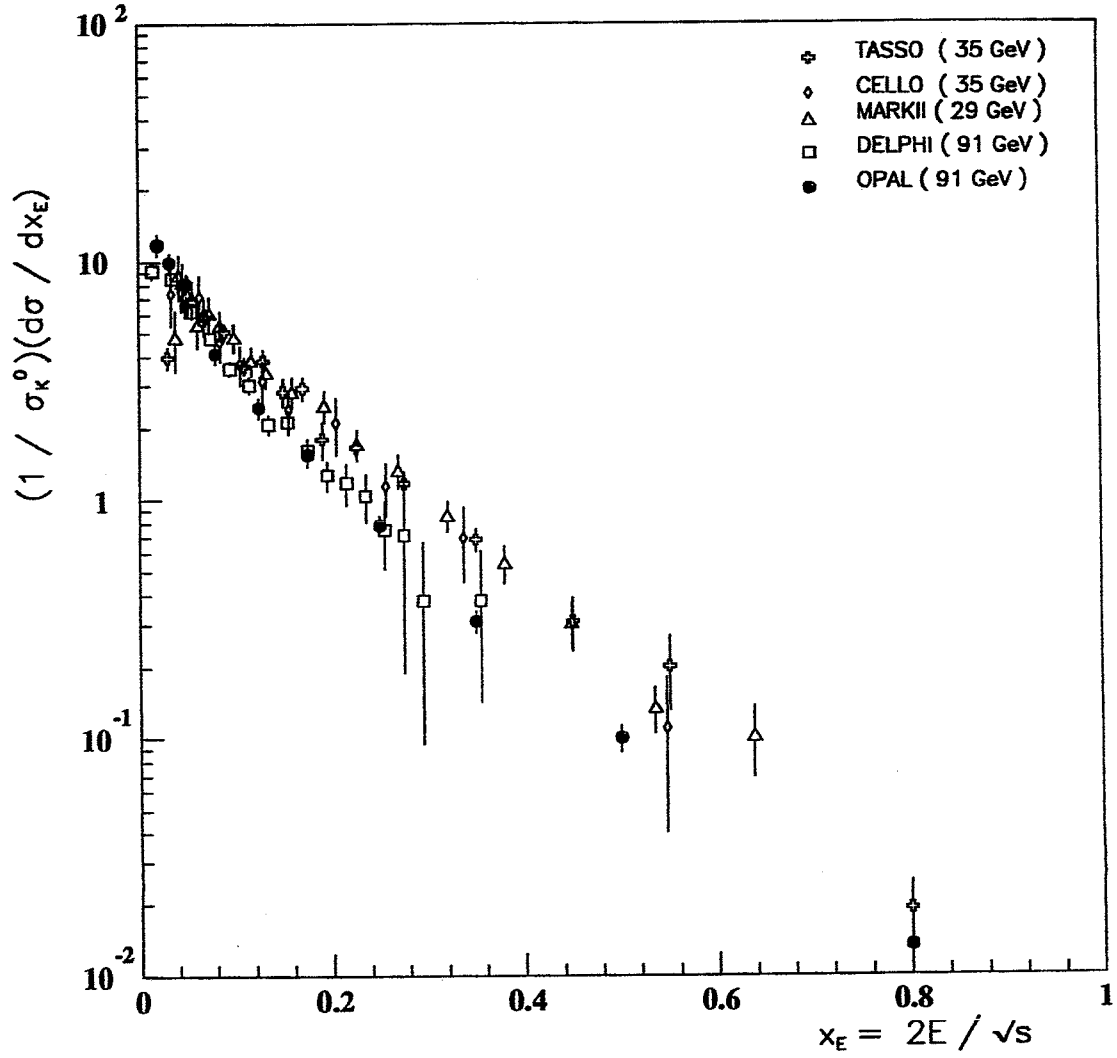

Figure 6.4: Comparison of measured normalised cross-sections for K^0 production at various energies.

Table 6.4: Scale invariant and normalised cross—section for the production of neutral Kaon, ($K^0, \overline{K^0}$). β is evaluated at the centre of each respective bin. The quoted error is statistical. There is a 7% systematic error.

$\langle x_E \rangle$	$\#K^0_s \to \pi^+\pi^-$ "Raw"	$\rho^{CJ/CZ}_{K^0_s}$	$A(x_E)$	$\frac{1}{\beta\,\sigma_{had}}\frac{d\sigma}{dx_E}$	$\frac{1}{\sigma_{K^0}}\frac{d\sigma}{dx_E}$
< 0.015	–	–	–	–	–
(0.015,0.025)	767±29	1.141±0.001	0.060±0.002	27.47± 1.39	11.80± 0.85
(0.025,0.04)	2208 ±55	1.200±0.001	0.125±0.002	20.56± 0.61	9.92± 0.33
(0.04,0.06)	2742 ±68	1.235±0.001	0.152±0.002	16.19± 0.45	8.10 ±0.24
(0.06,0.10)	3002 ±81	1.261±0.001	0.168±0.003	8.07± 0.26	4.10± 0.13
(0.10,0.15)	2019 ±63	1.275±0.001	0.154±0.003	4.76± 0.18	2.43± 0.09
(0.15,0.20)	1222 ±79	1.280±0.001	0.147±0.003	3.03± 0.21	1.55± 0.11
(0.20,0.30)	1069±41	1.275±0.001	0.127±0.003	1.52± 0.07	0.778± 0.04
(0.30,0.40)	358 ±26	1.270±0.001	0.105±0.002	0.61± 0.05	0.313± 0.03
(0.40,0.60)	193±17	1.265±0.001	0.087±0.002	0.119± 0.018	0.102± 0.009
(0.60,1.00)	35±7	1.255±0.001	0.060±0.004	0.0260± 0.005	0.0133± 0.003

6.3.1 Rapidity Distribution

The direction of the general flow of energy in an event is given by the thrust vector. It is of interest to study the capability of hadronisation models in reproducing flow distributions for particles relative to this general flow direction. The variable used to investigate this is the *rapidity*, defined as:

$$y_{\parallel} = \frac{1}{2}\ln\left(\frac{E + p_{\parallel}}{E - p_{\parallel}}\right) \tag{6.3}$$

where E is the particle energy and $p_{\parallel}$ is the particle momentum component parallel to the thrust axis.

The rapidity distribution is made up of a main plateau region (at small rapidity values) followed by a rapidly falling edge (at high rapidity) known as the "fragmentation region". The initial quarks are generated with a high rapidity

Table 6.5: Comparison of the production rate for various primary quark flavours below and and at the Z^0–peak.

Primary quark flavour	γ ($E_{cm} = 30$ GeV)	Z^0 ($E_{cm} = 91$ GeV)
$(u\bar{u}, c\bar{c})$	36%	17%
$(d\bar{d}, s\bar{s}, b\bar{b})$	9%	22%

$y_{\parallel} \approx \ln(\sqrt{s}/m_q)$ (where $\sqrt{s}$ is the centre–of–mass energy and m_q is the quark mass) and, because the confinement process involves only limited momentum transfer corresponding to a small change in rapidity, the fragmentation region is occupied by particles that contain the primary quarks. The plateau region, on the other hand, is mainly populated by particles made up of newly formed quarks.

The corrected rapidity distribution is presented in Table 6.6 and Figure 6.5. One observes good agreement between the data and both the JETSET and the HERWIG MC for high rapidity values. Over the plateau region, however, the HERWIG MC exhibits a somewhat different behaviour than the data. The data maintains a flat distribution while HERWIG has a fall off at small rapidity. This implies that the HERWIG MC predicts a diminished number of K^0 with small momentum component parallel to the jet axis as compared to the data.

6.3.2 Transverse Momentum Distributions In and Out of the Event Plane

Ideal two jet events result from back–to–back produced primary quarks. Such jets possess no transverse momentum and all of the energy flow is along the original

Table 6.6: The longitudinal rapidity ($y_{\parallel}$) distribution for neutral Kaon, ($K^0, \overline{K^0}$). The rapidity, $y_{\parallel}$, is defined with respect to the (principal) thrust axis for the event. The quoted error is statistical. There is a 7% systematic error.

$\langle y_{\parallel} \rangle$	$\#K^0_s \rightarrow \pi^+\pi^-$ "Raw"	$\rho^{CJ/CZ}_{K^0_s}$	$A(y_{\parallel})$	$\frac{1}{\sigma_{had}}\frac{d\sigma}{d\, y_{\parallel}}$
(0.,0.25)	391±25	1.202±0.004	0.042±0.002	0.631±0.053
(0.25,0.50)	510±28	1.241±0.002	0.061±0.002	0.585±0.040
(0.50,0.75)	674±31	1.240±0.002	0.075±0.003	0.635±0.037
(0.75,1.00)	880±36	1.230±0.001	0.104±0.003	0.591±0.029
(1.00,1.25)	1012±40	1.221±0.001	0.114±0.003	0.614±0.030
(1.25,1.50)	1092±42	1.219±0.001	0.129±0.003	0.586±0.027
(1.50,1.75)	1272±47	1.222±0.001	0.142±0.004	0.619±0.029
(1.75,2.00)	1190±50	1.236±0.001	0.144±0.004	0.581±0.029
(2.00,2.50)	1367±49	1.248±0.001	0.148±0.004	0.653±0.030
(2.25,2.50)	1135±52	1.262±0.001	0.152±0.005	0.535±0.030
(2.50,2.75)	1064±47	1.274±0.001	0.153±0.004	0.503±0.027
(2.75,3.00)	921±41	1.283±0.001	0.144±0.005	0.465±0.026
(3.00,3.50)	1028±45	1.293±0.001	0.137±0.004	0.274±0.014
(3.50,4.00)	315±47	1.298±0.002	0.128±0.008	0.0904±0.0147
(4.00,5.00)	70±10	1.292±0.005	0.058±0.008	0.0220±0.0044

direction of the primary quarks. Jets, however, do develop transverse momentum due to hard gluon radiation and the tunnelling process from vacuum involved in particle production.

The event plane can be defined in terms of the *thrust axis* and the *major thrust axis*; the two axes being perpendicular. The average momentum measured along the major thrust axis is known as the transverse momentum in the event plane, ($\langle P_{Tin} \rangle$). It is critically affected by hard gluon radiation and is a measure of 3 jet structure. A third thrust axis, known as the *minor thrust axis*, is defined to be perpendicular to the event plane and the average transverse momentum

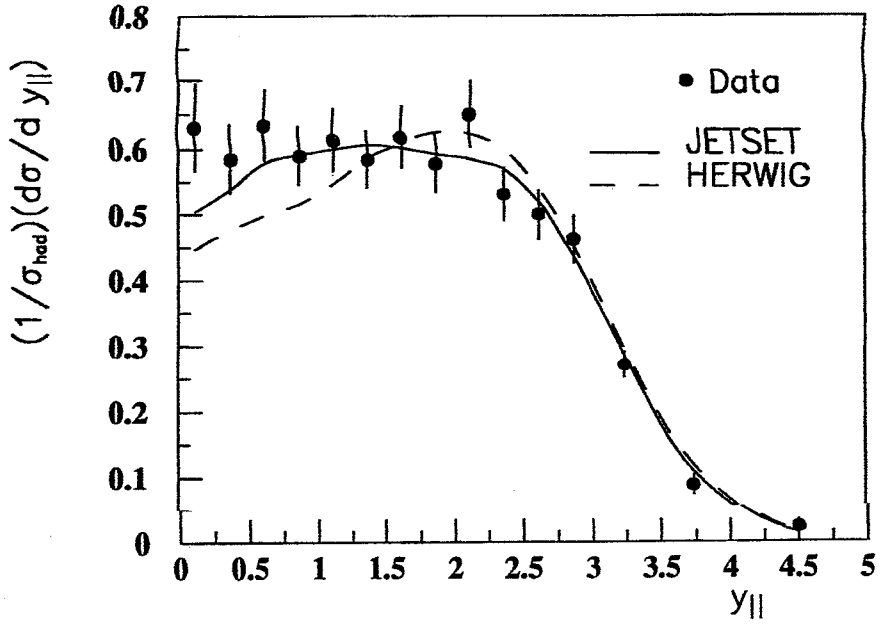

Figure 6.5: The longitudinal rapidity ($y_{||}$) distribution for inclusive production of neutral Kaon, $(K^0, \overline{K^0})$.

measured along this axis is known as the transverse momentum out of the event plane, ($\langle P_{Tout} \rangle$). This, in contrast to the other distributions, reflects the nature of jet transverse momentum as acquired during the quark hadronisation process. In the absence of any hard gluon radiation, the two distributions are expected to be identical. However, with hard gluon radiation present, one expects a broadening of the $\langle P_{Tin} \rangle$ distribution.

Figures 6.6(a) and 6.6(b) show the measured transverse momenta in and out of the event plane respectively, together with the JETSET and the HERWIG predictions. One clearly observes the broadening of the $\langle P_{Tin} \rangle$ distribution (with

Table 6.7: The transverse momentum distribution in the event plane (P_{Tin}) for neutral Kaon, ($K^0, \overline{K^0}$). The quoted error is statistical. In addition there is a 7% systematic error.
† → the entry is to be multiplied by 10^{-2}

$\langle p_{Tin} \rangle$ (GeV/c)	$\#K^0_s \to \pi^+\pi^-$ "Raw"	$\rho^{CJ/CZ}_{K^0_s}$	$A(P_{Tin})$	$\frac{1}{\sigma_{had}}\frac{d\sigma}{dP_{Tin}}$ $(GeV/c)^{-1}$
(0.00,0.20)	2447±63	1.236±0.002	0.100±0.002	2.156±0.068
(0.20,0.30)	1197±42	1.239±0.003	0.108±0.003	1.941±0.084
(0.30,0.50)	2094±55	1.238±0.002	0.117±0.002	1.575±0.052
(0.50,0.75)	1948±53	1.243±0.003	0.137±0.003	1.000±0.034
(0.75,1.00)	1444±44	1.240±0.002	0.144±0.004	0.704±0.028
(1.00,1.50)	1619±46	1.243±0.002	0.146±0.004	0.391±0.015
(1.50,2.00)	845±33	1.249±0.003	0.151±0.005	0.199±0.010
(2.00,3.00)	759±31	1.256±0.003	0.151±0.006	0.0896±0.0049
(3.00,5.00)	460±24	1.253±0.004	0.135±0.007	0.0303±0.0023
(5.00,10.00)	107±11	1.247±0.008	0.103±0.010	0.368±0.052 †

a Width at Half Max. of ~0.6 GeV/c) compared with that for $\langle P_{Tout} \rangle$ (a Width at Half Max. of ~0.4 GeV/c). The agreement between the data and the MC is quite good except at lower transverse momenta where the data indicates a smaller production rate than the expectation of both the JETSET and the HERWIG.

6.3.3 Sphericity Dependence of Strangeness Production

The sphericity of an event is dependent on the nature of the primary quarks (heavier beauty and charm quarks result in more spherical events) and the hard gluon emission (an increase in sphericity also corresponds to an increase in hard gluon radiation). Hence one could gain further insight into strangeness production by studying its dependence on event sphericity. Such a study will allow a comparison

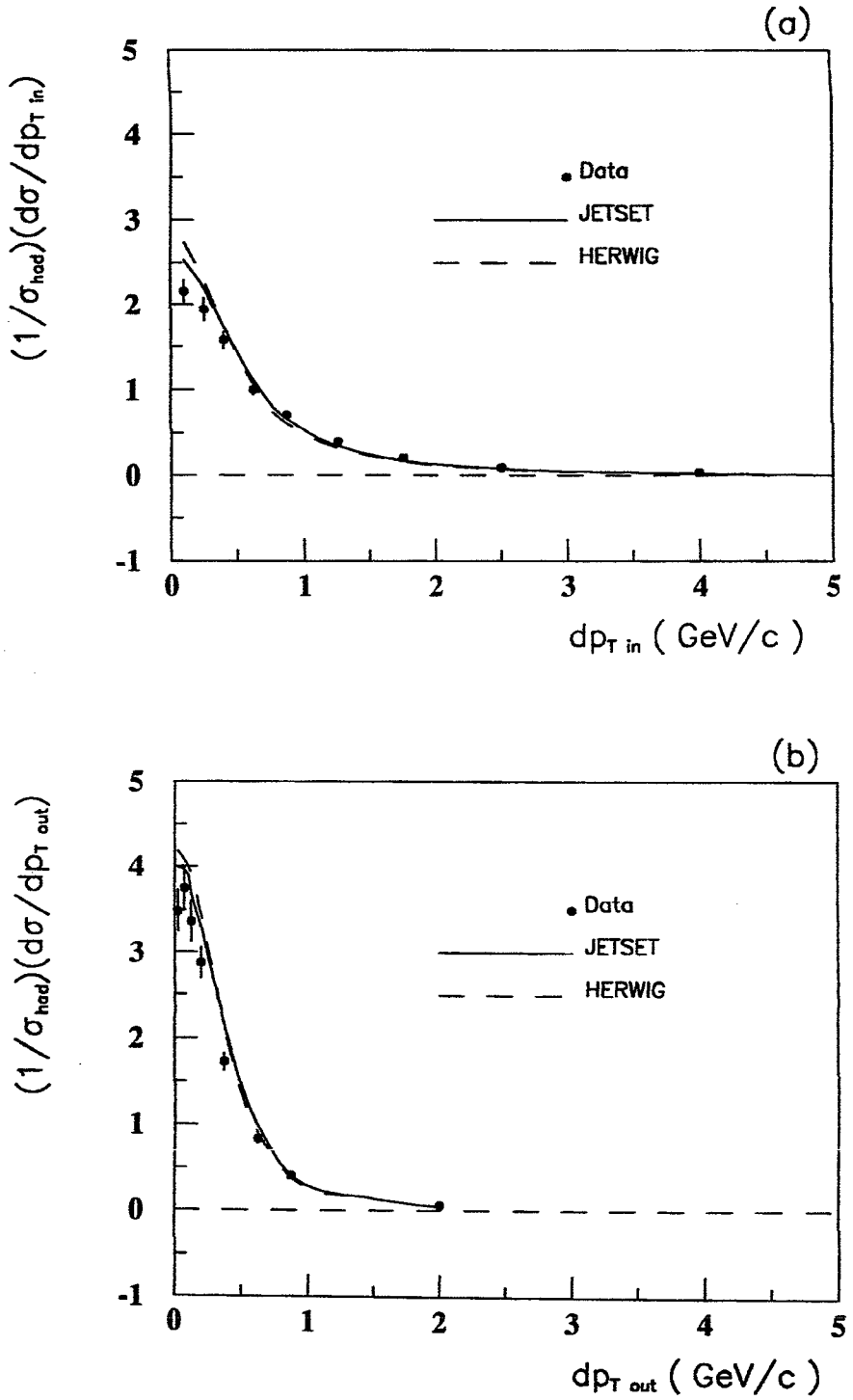

Figure 6.6: Production cross-section for K^0 (a) in the event plane (b) out of the event plane.

Table 6.8: The transverse momentum distribution **out** of the event plane (P_{Tout}) for neutral Kaon, ($K^0, \overline{K^0}$). The quoted error is statistical. In addition there is a 7% systematic error.
† → the entry is to be multiplied by 10^{-1}

$\langle p_{Tout} \rangle$ (GeV/c)	$\#K^0_s \to \pi^+\pi^-$ "Raw"	$\rho^{CJ/CZ}_{K^0_s}$	$A(P_{Tout})$	$\frac{1}{\sigma_{had}}\frac{d\sigma}{dP_{Tout}}$ $(GeV/c)^{-1}$
(0.00,0.05)	1191±43	1.236±0.003	0.120±0.003	3.487±0.155
(0.05,0.10)	1238±43	1.242±0.003	0.116±0.003	3.751±0.164
(0.10,0.15)	1170±42	1.236±0.003	0.122±0.003	3.365±0.150
(0.15,0.25)	2041±55	1.242±0.002	0.125±0.003	2.876±0.097
(0.25,0.50)	3779±73	1.242±0.001	0.127±0.002	2.098±0.051
(0.50,0.75)	1875±50	1.243±0.002	0.129±0.003	1.015±0.035
(0.75,1.00)	870±33	1.243±0.003	0.124±0.004	0.494±0.025
(1.00,3.00)	764±32	1.248±0.003	0.089±0.004	0.762±0.045 †

between such production in quark and gluon jets.

Figure 6.7(a) shows the rate of K^0 production per multihadronic event as a function of event sphericity. This clearly manifests an increasing trend for strangeness production with sphericity. An earlier MARK II measurement [50] at 91 GeV had indicated a possible depletion region in the data for low sphericity events as compared with the MC expectation [1]. In this analysis, however, no such discrepancy is observed between the data and the MC. In fact the sphericity dependence of strangeness production is described very well by the MC.

Data at lower centre–of–mass energy [54] has shown that the mean charged track multiplicity as well as the number of K^0 per multihadronic event increases with sphericity. However, there was no indication that the two multiplicities increase at different rates. Figure 6.7(b) shows the ratio of the K^0 production rate

[1]This would imply a preferential production of strangeness in gluonic jets as compared to quark jets.

to the mean charged track multiplicity as a function of sphericity for the OPAL data. It indicates that K^0 production and charged track multiplicity increase at the same rate as a function of sphericity, and therefore no preferential production of strangeness is indicated in gluonic jets.

6.4 QCD Prediction of Inclusive Particle Production Spectra

Recent analytical developments in perturbative QCD have made it possible to give definitive predictions about the inclusive particle production spectrum in terms of the Modified Leading Log Approximation (**MLLA**) [62] employing Local Parton Hadron Duality (**LPHD**) [63]. MLLA is an approximation that correctly keeps leading and next to leading logarithms in calculations. LPHD postulates that the conversion of partons into hadrons occurs on a low virtuality scale, independent of the scale of the primary process, and leads to close similarity between hadron and parton distributions. Such local duality is believed to be connected with the Amati and Veneziano "preconfinement" [64] properties of the QCD parton cascade. This perturbative approach then attempts to describe the global features of hadronic events such as inclusive energy spectra, multiplicity distributions, etc., independently of any particular fragmentation model. In doing so, it expands the regime of applicability of perturbative QCD.

According to this formulation, the inclusive particle spectra as a function of the logarithm of the inverse of the fractional momentum $\xi_p = \ln(1/x_p) = \ln(\sqrt{s}/2p)$ is a "humped-back" distribution, with the position of its maximum (ξ_p^*) dependent on the mass of the particle, decreasing as the mass of the particle increases. This distribution is expected to be approximately Gaussian in the vicinity of the

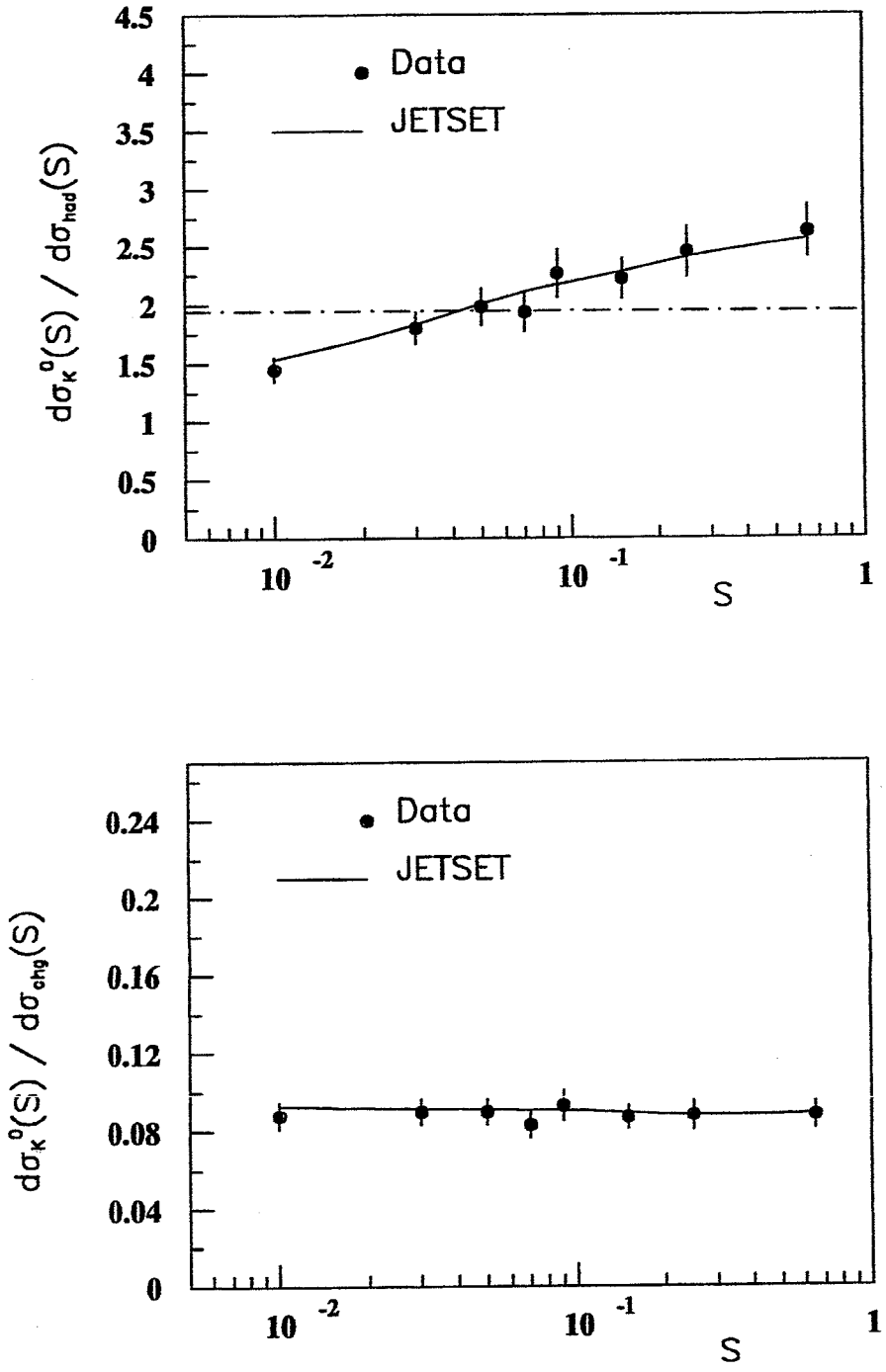

Figure 6.7: Sphericity dependence of strangeness production (a) K^0 production cross–section per multihadronic event (b) K^0 production cross–section normalised to average number of charged tracks.

Table 6.9: Differential cross–section for the production of neutral Kaon, $(K^0, \overline{K^0})$, as a function of $\xi_p = \ln(1/x_p)$. The quoted error is statistical. In addition there is a 7% systematic error.

$\langle\xi_p\rangle$	$\#K^0_s \to \pi^+\pi^-$ "Raw"	$\rho^{CJ/CZ}_{K^0_s}$	$A(\xi_p)$	$\frac{1}{\sigma_{had}}\frac{d\sigma}{d\xi_p}$
(0.0,1.0)	314±21	1.265±0.002	0.075±0.004	0.0751±0.0064
(1.0,1.4)	682±31	1.270±0.001	0.115±0.002	0.267±0.013
(1.4,1.6)	548±30	1.274±0.001	0.135±0.003	0.367±0.022
(1.6,1.8)	811 ±35	1.275±0.001	0.145±0.003	0.506±0.024
(1.8,2.0)	895±37	1.276±0.001	0.150±0.003	0.540±0.025
(2.0,2.2)	1011±44	1.275±0.001	0.153±0.003	0.600±0.029
(2.2,2.4)	1144 ±47	1.269±0.001	0.155±0.003	0.664±0.030
(2.4,2.6)	1198±50	1.261±0.001	0.168±0.003	0.640±0.029
(2.6,2.8)	1160±50	1.255±0.001	0.165±0.003	0.626±0.029
(2.8,3.0)	1182±39	1.240±0.001	0.158±0.002	0.660±0.023
(3.0,3.2)	1191±45	1.230±0.001	0.148±0.002	0.705±0.028
(3.2,3.4)	1066±48	1.215±0.001	0.138±0.002	0.668±0.032
(3.4,3.6)	740±21	1.200±0.001	0.123±0.002	0.514±0.017
(3.6,3.8)	651±36	1.180±0.001	0.105±0.002	0.469±0.027
(3.8,4.5)	767±29	1.141±0.001	0.060±0.002	0.299±0.015
>4.5	–	–	–	–

peak [65].

To gain insight into, and to test the validity of, this new QCD approach for predicting hadron production spectra, such inclusive distributions for a variety of particle species have been measured.

Table 6.9 presents the differential cross–section for the inclusive production for the K^0 as a function of ξ_p. Figure 6.8 compares the distributions for K^0_s, Λ, and all charged tracks as measured by OPAL. The fitted curve is a Gaussian to the K^0_s distribution (in the range $|\xi^* - \xi| < 1.$) and corresponds to a peak position

of $\xi^*_{K^0} = 2.70 \pm 0.08$. As expected the distribution for the charged tracks is at a higher value of $\xi^*_{charged} = 3.60 \pm 0.04$ [66]. No significant difference is observed between the distribution for the K^0 and Λ.

DELPHI [49] has obtained similar values for the peak positions: $\xi^*_{charged} = 3.67 \pm 0.10$, $\xi^*_{K^0} = 2.62 \pm 0.11$, $\xi^*_{\Lambda} = 2.82 \pm 0.25$. The DELPHI value for $\xi^*_{K^0}$ is in good agreement with the value determined in this work.

L3 [67] has measured this distribution for π^0 and finds the peak position to be at $\xi^*_{\pi^0} = 4.11 \pm 0.18$.

These measured distributions for various particle species are in fair agreement with the expectations of MLLA + LPHD. However, it is noted that the similarity of the distribution for the K^0 and Λ indicates a possible deviation from this description of inclusive particle production in the case of baryons.

6.5 Strange Vector Mesons: $K^{*+/-}(892)$ and $K^{*0}(892)$

In this section, the attention is turned to the inclusive production of strange vector mesons. Such mesons are produced both directly as a result of fragmentation and indirectly from the decay of higher mass particles. Based purely on statistical reasoning, the ratio of direct production of vector to pseudoscalar mesons, as given by spin degeneracy, is expected to be 3:1. Experiments at lower centre–of–mass energies have shown that light pseudoscalars are actually favoured over heavier vector mesons [68]. This observation is implemented phenomenologically in the JETSET MC via another tunable parameter which expresses the probability of production of a vector meson, V/(P+V). For the case of strange vector mesons this parameter is more specifically labelled as $(V/(P+V))_s$ and is designated as PARJ(12) in JETSET. It is set to a default value of 0.6 based on measurements

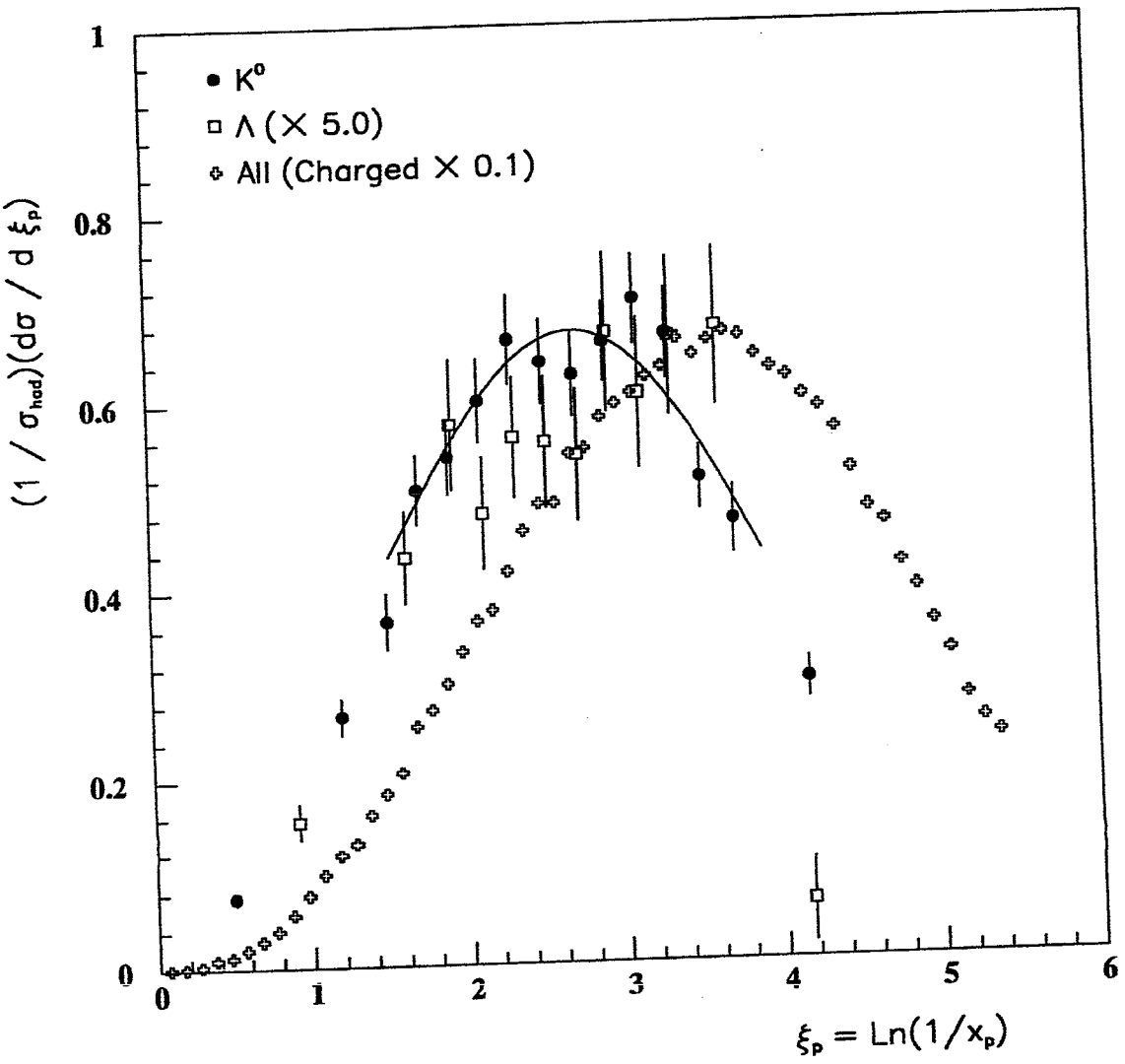

Figure 6.8: ξ_p distribution for K^0_s, Λ, and all charged tracks from OPAL. The curve is a Gaussian fit to the K^0_s distribution.

at lower centre–of–mass energies [68]. It is therefore of interest to determine this parameter at the Z^0 peak and gain further insight into the fragmentation process.

The detailed matter of rate extraction for the strange vector meson is not dealt with in depth in this thesis. However, the observation of the charged strange vector meson is presented and the recent OPAL rate measurements for $K^{*+/-}(892)$ [69] and $K^{*0}(892)$ [70] , based on the 1990 OPAL data, are provided. These rates, along with that already measured for K^0, are then used to infer a value for $(V/(P+V))_s$ at the Z^0 peak.

The charged K^* vector meson is reconstructed through its strong decay: $K^{*+/-} \rightarrow K^0\pi^{+/-}$. For the purposes of K^* detection, the previously reconstructed K^0_s is selected around the $\pi^+\pi^-$ mass peak within the range $0.475 < m_{\pi^+\pi^-} < 0.520$ GeV. The additional $\pi^{+/-}$ is selected from those tracks with $|d_0| < 0.5$ cm, $|z_0| < 5.0$ cm, and which have 3 CZ hits. The observed $K^{*+/-}(892)$ peak is seen in Figure 6.9. Its reconstructed mass and width are: $m = 0.8907 \pm 0.0037$ (GeV), and $\Gamma = 0.0519 \pm 0.0107$ (GeV), which are in good agreement with the world average as quoted by the Particle Data Group [48] of $m = 0.8918 \pm 0.0002$ (GeV), and $\Gamma = 0.0498 \pm 0.0008$ (GeV) for the charged mode. The chosen fitting function had the form

$$f(m) = N\frac{(\Gamma/2)^2}{[(m-\mu)^2 + (\Gamma/2)^2]} + BKG \qquad (6.4)$$

where the background took the form:

$$BKG = \alpha_1(m - m_0)^{\alpha_2}\ e^{-(\alpha_2 m + \alpha_3 m^2)} \qquad (6.5)$$

Using this technique for $K^{*+/-}(892)$ reconstruction [69], OPAL has determined an inclusive production rate of $0.889 \pm 0.012(\text{stat.}) \pm 0.150(\text{sys.})$ per hadronic

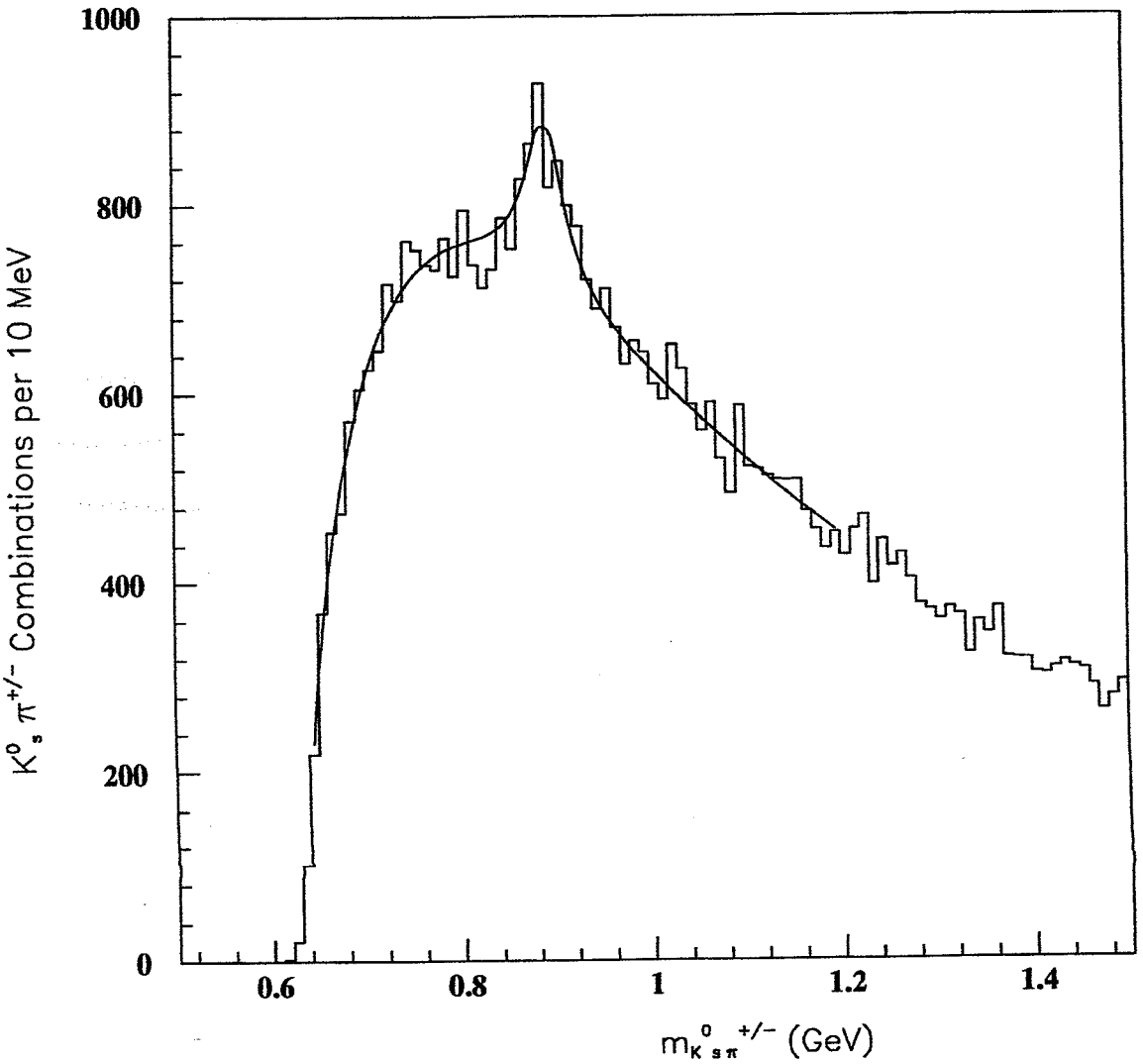

Figure 6.9: Reconstructed charged K*(892) mass distribution from $K^0_s \pi^{+/-}$ combinations.

event. This rate compares favourably with that of the HERWIG prediction of 0.81 while JETSET with its default parameters predicts a rate of 1.100.

Employing the already measured suppression factor of $\gamma_s = 0.25 \pm 0.03$, it was determined that the above measured $K^{*+/-}(892)$ rate corresponds to $(V/(P+V))_s = 0.52 \pm 0.10$ in JETSET. It was subsequently checked that with the tuned parameters, $\gamma_s = 0.25$ and $V/(P+V)_s = 0.52$, the expected JETSET K^0 multiplicity was in agreement with the previously measured K^0 rate of $1.95 \pm 0.03(stat.) \pm 0.14(sys.)$.

$K^{*0}(892)$ has also been reconstructed in OPAL [70] via the decay chain $K^{*0}(892) \rightarrow K^{+/-}\pi^{+/-}$, where the dE/dx information from the Jet chamber has been used in particle identification. The inclusive production rate for $K^{*0}(892)$ is measured to be $0.79 \pm 0.07(stat.) \pm 0.04(sys.)$ per hadronic event. This is in good agreement with HERWIG expected rate of 0.777 while JETSET, with its default parameters, gives an expected rate of 1.06. Once again, using the measured $\gamma_s = 0.25 \pm 0.03$, the determined value for $(V/(P+V))_s = 0.50 \pm 0.05$. With this choice of parameters one has agreement between the measured $K^{*0}(892)$ rate and its JETSET expected rate. [2]

The determined value of the parameter $(V/(P+V))_s$ from both $K^{*0}(892)$ and $K^{*+/-}(892)$ are in good agreement and indicate that strange pseudoscalar and vector meson direct production rates are comparable in fragmentation process.

6.6 Future Prospects

This study concentrated on production characteristics of single K^0 in a multihadronic environment. Much time was invested in understanding the K^0 signal extraction, its proper handling and the associated systematics.

[2] A global fit [70] to OPAL, L3 and DELPHI rate measurements for all charged, π^0, K^0, $\omega(783)$, $K^{*+/-}(892)$, $K^{*0}(892)$, $\phi(1020)$, Λ and Ξ gives $0.22 < \gamma_s < 0.25$ and $0.4 < (V/(P+V))_s < 0.5$.

With this knowledge and a larger data sample in hand, one could investigate in more detail the nature of hadronisation, with K^0 as a probe, by looking at multi-K^0 events production characteristics versus those for single K^0 events, K^0–K^0 correlations and K^0 properties in 2 and 3 jet events. With a larger data set a study of production characteristics of strange tensor mesons, such as $K_2^*(1430)$, is also feasible. Charm production could be investigated using K^0 via decay channels such as $D^0 \to \overline{K^0}\pi^+\pi^-$ and $D^+ \to \overline{K^0}\pi^+, \overline{K^0}\pi^+\pi^+\pi^-$. Finally, a study of the rare decay $D^0 \to \overline{K^0}K^0$ is also of interest.

Chapter 7

Conclusions

The behaviour of K^0 production at the Z^0 resonance has been studied and several distributions characterising this production in hadronisation have been investigated. The data set used for this purpose comprised of 138,638 multihadronic Z^0 decays, was collected by the OPAL detector in 1990. The findings have been compared with the expectations of two Monte Carlo models: JETSET 7.2 (string fragmentation) and HERWIG 5.0 (cluster fragmentation) which had been tuned so as to describe the overall global event shapes.

The inclusive production rate for K^0 at 91 GeV has been measured to be 1.95±0.03 (stat.)±0.14 (sys.) per multihadronic event. This measurement agrees with the JETSET and HERWIG expected rates although JETSET predicts a slightly higher rate. The measurement is in accord with the recently published DELPHI rate of 2.12±0.05 (stat.)±0.04 (sys.). MARK II has reported a rate of 1.54±0.21 (stat.)±0.18 (sys.) which is substantially below (about 1.5 σ) the present measured rate. Together with results from other e^+e^- experiments at lower centre–of–mass energies it is concluded that JETSET and HERWIG both provide a fairly good description of the variation of K^0 multiplicity over the energy range 10–91 GeV.

The OPAL measured mulitiplicity for K^0 corresponds, within the JETSET model, to a strangeness suppression factor of $\gamma_s = 0.25 \pm 0.03$. The available data from νp, μp, hadron–hadron and e^+e^- experiments at different centre–of–mass

energies, suggests that the strangeness suppression factor lies in the range of 0.2–0.3 with no evidence for its dependence on the reaction type or the centre–of–mass energy.

The inclusive single particle scaling cross–section ($\frac{1}{\beta}\frac{1}{\sigma_{had}}\frac{d\sigma}{dx_E}$) has also been measured. JETSET and HERWIG both provide a very good description for this distribution. A comparison of this cross–section with those at lower centre–of–mass energies indicates scaling violation. The cross–sections at the higher centre–of–mass energy are softer signifying the increased contribution of strangeness from gluon radiation and from heavier primary quarks.

K^0 production within jets has been studied in terms of rapidity ($y_{\parallel}$) and transverse momentum in (P_{Tin}) and out (P_{Tout}) of the event plane. Both the JETSET and HERWIG MC accurately describe the measured rapidity distribution in the high rapidity region. However, in the plateau region near zero rapidity, the HERWIG MC prediction deviates from the measured data points by predicting a reduced production of K^0 with small momentum component parallel to the jet axis. The transverse momentum in and out of the event plane are also well described by the two MC except that, at lower values of transverse momenta, JETSET and HERWIG slightly overestimate K^0 production. As expected, P_{Tin} exhibits a broader distribution than P_{Tout} due to the hard gluon radiation.

The K^0 production dependence on event sphericity has also been investigated. The results indicate an increase in production with sphericity, a trend which is very well predicted by the MC. An earlier MARK II result at 91 GeV had hinted at a possible depletion of K^0 at lower sphericity which would imply a preferential production of K^0 in gluonic jets at 91 GeV. There are no such indications in the present analysis. In fact, the ratio of K^0 production to the charge track multiplic-

ity as a function of sphericity exhibits a uniform distribution. If strangeness were preferentially produced in gluonic jets (more spherical events) then the distribution would not have been flat. This sphericity–dependent behaviour agrees with observations at lower centre–of–mass energies.

The inclusive K^0 production as a function of the logarithm of the inverse of the fractional momentum, $\xi_p = \ln(1/x_p)$, has also been determined. In accordance with MLLA+LPHD, the expected humped–back distribution is observed, signifying the coherent emission and the subsequent destructive interference of soft gluons. A comparison with other particle species reveals the expected decreasing trend in the position of the peak for such a distribution with increasing particle mass, although there are indications (from Λ measurements both by OPAL and DELPHI) that for baryons there might be deviation from this behaviour.

Using the OPAL measured rates for strange vector mesons, $K^{*+/-}$ and K^{*0}, the relative probability for the generation of strange vector mesons has been determined to be $(V/(P+V))_s = 0.50 \pm 0.04$. This implies that strange pseudoscalar and vector mesons are produced in equal proportion in the fragmentation process.

This thesis has presented the results of a study on some aspects of hadronisation process as probed by K^0 meson. In summary, K^0 production is well represented by the hadronisation models considered, although some slight parameter tuning is indicated in the case of JETSET.

Bibliography

[1] H. Yukawa, Proc. Physico-Mathematical Soc. of Japan, **17**(1935)48.

[2] C. M. Lattes et al., Nature **160**(1947)453.

[3] E. Fermi, Z. Physik **88**(1934)161.

[4] G. D. Rochester and C. C. Butler, Nature **160**(1947)855.

[5] A. Pais, Phys. Rev. **86**(1952)663.

[6] M. Gell-Mann, Phys. Rev. **92**(1953)883; Nuovo Cimento 4, suppl.2(1956)848.

[7] T. Nakano and K. Nishijima, Prog. Theor. Phys. **10**(1953)581.

[8] M. Gell-Mann and Y. Ne'eman, *The Eightfold Way,* Benjamin, New York(1964).

[9] M. Gell-Mann, Phys. Lett. **8**(1964) 214.
G. Zweig, CERN preprint 8409/TH.412 (unpublished).

[10] S. L. Glashow, J. Illiopoulos and L. Maiani, Phys. Rev. **D2**(1970)1285.

[11] J. J. Aubert et al., Phys. Rev. Lett. **33**(1974)1404.
J.-E. Augustin et al., Phys. Rev. Lett. **33**(1974)1406.

[12] M. Kobayashi and T. Maskawa, Prog. Theor. Phys. **49**(1973)652.

[13] D. Griffiths, *Introduction to Elementary Particles,* John Wiley, New York(1987);
I. S. Hughes, *Elementary Particles,* Cambridge University Press, Cambridge(1991);
F. Halzen and A. Martin, *Quarks and Leptons: An Introductory Course in Modern Particle Physics,* John Wiley, New York(1984);
D. H. Perkins, *Introduction to High Energy Physics,* Addison-Wesley(1987).

[14] H. Fritzsch, M. Gell-Mann and H. Leutwyler, Phys. Lett. **47B**(1973)365;
H. D. Politzer, Phys. Rev. Lett. **30**(1973)1346;
D. Gross and F. Wilczek, Phys. Rev. Lett. **30**(1973)1343;
S. Weinberg, Phys. Rev. Lett. **31** (1973)494.

[15] S. L. Glashow, Nucl. Phys. **22**(1961)589;
S. Weinberg, Phys. Rev. Lett. **19**(1967)1264;
A. Salam and J. C. Ward, Phys. Lett. **13**(1964)168.

[16] C. Quigg, *Gauge Theories of the Strong, Weak and Electromagnetic Interactions*, Benjamin Cummings(1983).

[17] R. K. Ellis, D. A. Ross and E. A. Terrano, Nucl. Phys. **B178**(1981)421;
F. Gutbrod, G. Kramer and G. Schierholz, Z. Phys. **C21**(1984)235.

[18] G. Altarelli and G. Parisi, Nucl. Phys. **B126**(1977)298.

[19] G. C. Fox and S. Wolfram, Nucl. Phys. **B168**(1980)285;
R. D. Field and S. Wolfram, Nucl. Phys. **B213**(1983)65;
T. D. Gottschalk, Nucl. Phys. **B214**(1983)201.

[20] A. Bassetto et al., Phys. Rep. **100**(1983)201;
G. Marchesini and B. R. Webber, Nucl. Phys. **B238**(1984)1;
A. H. Mueller, Phys. Lett. **104B**(1981)161;

[21] B. Bambah, et al., *QCD Generators for LEP*, CERN-TH.5466/89;
D. H. Saxon, *Jet Fragmentation*, RAL-85-077;
D. H. Saxon, *Quark and Gluon Fragmentaion in High Energy* e^+e^- *Annihilation*, RAL-86-057.

[22] R. D. Field and R. P. Feynman, Nucl. Phys. **B136**(1978)1.

[23] B. Andersson et al., Nucl. Phys. **B135**(1978)273.

[24] T. Sjöstrand and M. Bengtsson, Comp. Phys. Commun. **43**(1987)367;
M. Bengtsson and T. Sjöstrand, Nucl. Phys. **B289**(1987)810;
B. Andersson et al., Phys. Rep. **97**(1983)31.

[25] JADE Collaboration, W. Bartel et al., Z. Phys. **C21**(1983)37;
TPC Collaboration, A. Aihara et al., Z. Phys. **C28**(1985)31;
TASSO Collaboration, M. Althoff et al., Z. Phys. **C29**(1985)29.

[26] X. Artru and G. Mennessier, Nucl. Phys. **B70**(1974)93;
X. Artru, Phys. Rep. **97**(1983)147.

[27] E. Brezin and C. Itzykson, Phys. Rev. **D2**(1970)1191;
A. Casher et al., Phys. Rev. **D20**(1979)179;
H. Neuberger, Phys. Rev. **D20**(1979)2936;
A. Casher et al., Phys. Rev. **D21**(1980)1966.

[28] OPAL Collaboration, M. Z. Akrawy et al., Z. Phys. **C47**(1990)505.

[29] Yuval Ne'eman and Yoram Kirsh, *The Particle Hunters*, Cambridge University Press, Cambridge(1987).

[30] LEP Design Reports. CERN/ISR-LEP/79-33., CERN/PS/DL/83-31., CERN-LEP/84-01.

[31] C. Pellegrini, Ann. Rev. Nucl. Sci., **22**(1972)1.

[32] OPAL Collaboration, K. Ahmet et al., *The OPAL Detector at LEP*, Nucl. Instr. Meth. **A305**(1991)275.

[33] J.R. Carter, et al., Nucl. Inst. Meth. **A286**(1990)99.

[34] H. M. Fischer et al., Nucl. Inst. Meth. **A283**(1989)492.

[35] H. Mes, et al., Nucl. Inst. Meth. **A265**(1988)445.

[36] OPAL Collaboration, *Report on Data Acquisition and Analysis*, CERN/LEPC 84-2, LEPC/PR1 OPAL.

[37] OPAL Collaboration, *The Trigger System of the OPAL Experiment at LEP*, submitted to Nucl. Instr. Meth.

[38] OPAL Collaboration, *The OPAL Data Acquisition System*, submitted to Nucl. Inst. Meth.

[39] ZEBRA Data Structure Management System; CERN Computer Centre Library. DD/EE/85-6.

[40] T. Mori, *Multihadronic Cross Section in 1990*, OPAL–TN025.

[41] R. Gluckstern, Nucl. Inst. Meth. **24**(1963)381.

[42] P. Billoir, Nucl. Inst. Meth. **A225**(1984)352.

[43] V. Karimaki, CERN UA1/TN/82-24.

[44] D. Savard et al., Nucl. Inst. Meth. **A268**(1988)278.

[45] D.G. Cassel and M. Ogg, *DUET - A track finding program for Cylindrical Geometries*, a CLEO code adopted for OPAL use.

[46] Pierre Billoir, *Fast and Flexible Vertex Fit*, Preprint LPC 85-01, College de France(1985).

[47] F. James and M. Roos, *MINUIT, a system for function minimisation and analysis of the parameter errors and correlations,* Comp. Phys. Comm. **10**(1975)343.

[48] Particle Data Group,*Review of Paticle Properties,* Phys. Lett. **B239**(1990).

[49] DELPHI Collaboration, P. Abreu et al., *Production of Stange Particles in the Hadronic Decays of the Z^0*, CERN-PPE/91-207, submitted to Phys. Lett. B.

[50] C. S. Fordham, Ph.D. Thesis, SLAC-Report-374, October 1990.

[51] PLUTO Collaboration, Ch. Berger et al., Phys. Lett. **104B**(1981)79.

[52] CLEO Collaboration, S. Behrends et al., Phys. Rev. **D31**(1985)2161.

[53] JADE Collaboration, W. Bartel et al., Z. Phys. **C20**(1983)187.

[54] TASSO Collaboration, W. Braunschweig et al., Z. Phys. **C47**(1990)167.

[55] HRS Collaboration, M. Derrick et al., Phys. Rev. **D35**(1987)2639.

[56] Mark II Collaboration, H. Schellman et al., Phys. Rev. **D31**(1985)3013.

[57] TPC Collaboration, H. Aihara et al., Phys. Rev. Lett. **53**(1984)2378.

[58] CELLO Collaboration, H.-J. Behrend et al., Z. Phys. **C46**(1990)397.

[59] BEBC, G. T. Jones et al., Z. Phys. **C27**(1985)43.

[60] EMC Collaboration, M. Arneodo et al., Z. Phys. **C34**(1987)283.

[61] P.K. Malhotra and R. Ovara, Z. Phys. **C17**(1983)85.

[62] A. H. Mueller, Nucl. Phys. **213**(1983)85 and erratum quoted in Nucl. Phys. **B241**(1984)141.

[63] Ya. I. Azimov et al. , Z. Phys. **C27**(1985)65; Z. Phys. **C31**(1986)213.

[64] D. Amati and G. Veneziano, Phys. Lett. **83B**(1979)87.

[65] Yu. L. Dokshitzer et al., *Perturbative Quantum Chromodynamics*, ed. A. H. Mueller, World Scientific, Singapore (1989)241.
Yu. L. Dokshitzer et al., Rev. Mod. Phys. **60**(1988)373.

[66] OPAL Collaboration, M. Z. Akrawy et al., Phys. Lett. **B247**(1990)617.

[67] L3 Collaboration, B. Adeva et al., Phys. Lett. **259B**(1991)199.

[68] JADE Collaboration, W. Bartel et al., Phys. Lett. **145B**(1984)441.
HRS Collaboration, M. Derrick et al., Phys. Lett. **158B**(1985)519.
TPC Collaboration, H. Aihara et al., Phys. Rev. Lett. **53**(1984)2378.
CELLO Collaboration, H.-J. Behrend et al., Z. Phys. **C46**(1990)397.

[69] G. Maringer, *Production of charged* K^* *mesons in* Z^0, OPAL Technical Note, TN063.

[70] OPAL Collaboration, *Inclusive neutral vector meson production in hadronic* Z^0 *decays*, CERN-PPE/92.